Appendix A

Implications of the Depth of Seismicity for the Rupture Extent of Future Earthquakes in the San Francisco Bay Area

Colin F. Williams, USGS, Menlo Park

Introduction

This appendix addresses some issues related to the depth extent of seismicity in the San Francisco Bay Area and the potential implications for the rupture extent of future major earthquakes. The connection between the depth extent of seismicity and the size of major earthquakes lies in the seismic moment, M_0, for an earthquake, which is defined as $M_0 = \mu DA$, where μ is the shear modulus, D is the average coseismic displacement across the fault, and A is the area of the ruptured fault surface. The resulting moment magnitude, **M**, is then calculated from the relation $\mathbf{M} = 2/3 * \log M_0 - 10.7$ (Hanks and Kanamori, 1979). The rupture area A is the product of the rupture length, L, and the downdip rupture width, W. Consequently, it is important to place constraints on the value of W in order to accurately estimate the seismic moment release from future major earthquakes.

Because almost all of the historical major earthquakes in the San Francisco Bay region predate the deployment of Northern California Seismic Network (NCSN), there are few direct observations on the depth extent of coseismic rupture. However, the available evidence from the major continental earthquakes in California and elsewhere suggests that the maximum depth extent of "background" seismicity is essentially equal to the maximum coseismic rupture extent of a major earthquake on the same fault segment, provided there is enough seismicity to illuminate the entire seismogenic portion of the fault segment (e.g., Strehlau and Williams, 1998). The first section of this appendix summarizes observations on the depth extent of seismicity in the San Francisco Bay region based on well-recorded seismicity. The third section discusses some of the uncertainties inherent in using various sorts of seismic events (i.e., background microseismicity, aftershocks, mainshocks) to quantify the likely depth extent of rupture.

An additional constraint on the width of the seismogenic zone is found in the thermal state of the crust, as temperature controls both the mode of crustal deformation (brittle versus plastic) and the frictional behavior (seismic versus aseismic) of faults within the brittle field. The second section of this appendix addresses the significance of the seismicity observations in light of what is known about the thermal field in the region, with estimates of temperatures at seismogenic depth derived from near-surface heat flow measurement. The appendix refers to fault segments established by OF96-705 (the Working Group on Northern California Earthquake Potential) and those established by Working Group 02 for the current study.

Observations Based on Seismicity

Bay Area faults show substantial variations in the frequency and distribution of "background" seismicity (Figure 1). The portion of the San Andreas fault passing through the Peninsula and the

North Bay is relatively aseismic and presumably has been locked since the 1906 earthquake. Historical seismicity for the Santa Cruz Mountains segment is dominated by aftershocks of the Loma Prieta earthquake but was somewhat more active than other segments even before 1989. Similarly, the San Gregorio Fault is relatively aseismic along its northern section but active over a fairly broad zone adjoining the Santa Cruz Mountains and entering Monterey Bay. The Hayward, Calaveras, and Rodgers Creek faults are characterized by abundant microseismicity, although there are aseismic segments along each fault. Northeast of these faults the seismicity becomes more diffuse and the individual fault segments more difficult to trace.

The seismicity data presented in the figures and analyzed in this report consist of NCSN events of $M \geq 1.5$ with an rms <0.15 seconds and at least 6 stations recording each event in the years from 1980 to the end of 1998. The analysis summarized in this appendix includes the Maacama fault, which is the northwestward extension of the Rodgers Creek fault, and the NCSN catalogue from the period before 1980 is too uneven in its geographic coverage of the region encompassing the Maacama fault to be used for the study. In order to verify the statistical consistency of the results the same analysis has been repeated with the lower magnitude cut-off varied in the range from 1.2 to 1.8 and adjustments to the $M \geq 1.5$ dataset related to the rms of the event solution, the number of stations recording the event, and the covered time period. The quantitative results did not vary significantly with any of these changes. For a few segments reducing the sample population by increasing the lower magnitude threshold to 1.8 introduced greater uncertainties even though the mean values remained essentially the same.

The basic results are consistent with those found in earlier studies (e.g., Hill et al., 1990; Walter et al., 1998), although the lower cut-off magnitude relative to Walter et al. (1998) and the longer time interval relative to Hill et al. (1990) fill in gaps in some of the fault segments. The average depth extent of seismicity on Bay Area faults is approximately 14 km. On the Loma Prieta (Santa Cruz Mountains) segment of the San Andrea fault, the deep (>14 km) seismicity that characterized both the 1989 mainshock and its aftershocks is absent from the catalogue during the time from 1980 to 1989. Seismicity from the period of 1969 through 1980 does reveal deeper seismicity along the Loma Prieta segment. It is possible that other segments discussed below are similarly undersampled with respect to the maximum depth extent of seismicity.

In all cases the “95% Cut-off” column in the table refers to the 95% cut-off depth (i.e., 95% of the hypocenters are equal to or shallower than that depth). As discussed below, the available evidence suggests that a 95% cut-off provides a reasonable estimate of the likely depth extent of coseismic rupture in a major earthquake, provided there is enough seismicity to reduce statistical uncertainties. In general a 90% cut-off tends to underestimate the depth extent of rupture, and a 98% or 99% cut-off tends to overestimate the depth extent of rupture and to suffer from greater scatter due to anomalously deep events unrelated to the overall depth extent of coseismic moment release in major earthquakes.

The results are best summarized with a segment-by-segment comparison of the 95% cut-off depths with the segment widths reported in OF96-705 and selected for WG02. The segment boundaries used for determining the 95% cut-off are those updated for the WG02 study. Fault segments are abbreviated as follows: SAO, San Andreas fault offshore; SAN, San Andreas fault north; SAP, San Andreas fault peninsula; SAS, San Andreas fault south; SGN, San Gregorio

fault north; SGS, San Gregorio fault south; HN, Hayward fault north; HS, Hayward fault south; RC, Rodgers Creek fault; MF, Maacama fault; CN, Calaveras fault north; CC, Calaveras fault central; CS, Calaveras fault south; CON, Concord fault; GVN, Green Valley fault north; GVS, Green Valley fault south; GN, Greenville fault north: GS, Greenville fault south.

Segment	**OF96-705**	**95% Cutoff**	**WG02**
SAN[1]	13 km	Too few eqs	11±2
SAO[1]	13 km	Too few eqs	11±2
SAP[1]	14	14	13±2
SAS[2]	18	18	15±2
SGN[3]	15	Too few eqs	13±2
SGS[4]	12	16	12±2
RC[5]	10	10	12±2
HN	12	13	12±2
HS	12	13	12±2
MF Central	12	8	N/A
MF South	12	<8	N/A
CN	13	15	13±2
CC	10	10	11±2
CS	10	10	11±2
CON	12	16	16±2
GVN	12	16	14±2
GVS	12	14	14±2
GN	11	21[6]	15±3
GS	11	15	15±3

Notes:

1. The change in width from OF96-705 to WG02 for these two segments is due to a slightly more conservative estimate of the maximum depth of seismicity from earthquakes larger than magnitude 1.5.
2. The OF96-705 and the 95% cut-off values reflect the abundant deep seismicity associated with the Loma Prieta earthquake. These events form a local maximum in depth for the entire segment, so the WG02 value of 15 reflects an average width for the segment. In addition, standard catalogue depths are probably affected by lateral velocity contrasts (see Section on Uncertainties).
3. Research by Stephanie Ross (Ross et al., 1998) suggests that the OF96-705 width is too large. This is supported by heat flow measurements along the San Mateo County and Santa Cruz County coast, which would be consistent with widths less than 14 km.
4. Seismicity along the southern SGF is relatively sparse, leaving some question as to the statistical significance of the 95% cut-off. In addition, location of events along the SGF in this vicinity is probably affected by the same effects biasing hypocenters for the Loma Prieta earthquake (see Section on Uncertainties).
5. The WG02 width for the RCF has been deepened by 2 km in order to allow for the possibility that the relatively sparse seismicity on the RCF undersamples the true segment width. However, the limited heat flow constraints suggest the 10 km figure may be correct (see below).
6. There is a substantial deepening of seismicity along the northern portion of the Greenville Fault trend (see Figures 2-4). The WG02 value reflects an average.

These variations among fault segments are easily seen in the accompanying plots (Figures 1 through 6) which show selected SW-NE cross-sections of seismicity through the San Francisco Bay Area. In the tabulated results there are five segments/areas for which the 95% cut-off depth differs significantly from the 1996 report. These are the central and southern Maacama fault (which includes the Healdsburg fault), the Concord and Green Valley faults, and the northern portion of the Greenville fault trend. Seismicity is shallower by about 4 km on the Maacama than the rupture depth postulated by the 1996 report and deeper by 3 to 10 km on the East Bay segments. Although the resulting change in moment is large (25 to 100%), the effect on moment magnitude (using the Wells and Coppersmith [1994] magnitude-area formulas) is generally less than 0.3. The primary effect on regional forecasts would be to reduce the hazard in the North Bay and increase the hazard in the East Bay beyond the Calaveras fault. The shallower depths along the Hayward-Rodgers Creek-Maacama fault trend is best seen in Figure 7, which shows a steady shallowing in seismicity from the nothern Hayward up to The Geysers steam field. (Note – The northwestern edge of Box A starts at 160 km on this section.)

Observations Based on Heat Flow

Temperature is an important factor in determining whether a fault zone slips seismically or aseismically. Sibson (1982) was the first to highlight the general inverse correlation between heat flow in the maximum depth of seismicity along the San Andreas fault. Recent efforts to quantify this relationship indicate that the base of seismicity corresponds with a temperature of 350 to 400 ^{o}C in the California Coast Ranges (Williams, 1995) but may vary over a wider temperature range in southern California (Williams, 1996; Strehlau and Williams, 1998). This section extends these earlier studies to a detailed segment-by-segment comparison of subsurface temperatures estimated from shallow heat-flow measurements with the observed base of seismicity.

Figure 8 shows the locations of heat flow measurements in the San Francisco Bay Area along with contours that are both consistent with the data and thought to be representative of the conductive thermal regime at mid-crustal depths. The figure also includes events from Figure 1 with depths greater than 15 km. These data highlight the general correlation of deeper events with lower heat flow. Although data are sparse in the North Bay along the Rodgers Creek fault, the broad heat flow anomaly associated with The Geysers geothermal field and the Clear Lake volcanics coincides with the shallow seismic-aseismic transition on the central and southern Maacama fault segments. The deep seismicity in the Suisun Bay/Mt. Diablo region (COF, GVF, GF) is related to low heat flow mostly on the basis of contouring rather than on local measurments. New heat flow data have been collected from this area, and the preliminary results are consistent with the existing contours. Figure 9 summarizes the quantitative results for selected areas with estimated temperatures at the depths recorded in the first table. Overall the results are consistent with a seismic-aseismic transition in the temperature range of 350 to 400 ^{o}C. This agrees with results from elsewhere in the Coast Ranges and in portions of southern California (Strehlau and Williams, 1998). The bottom line is that the heat flow data would predict a shallow seismic-aseismic transition along the Rodgers Creek/Maacama fault trend as it nears The Geysers, a deep seismic-aseismic transition in the Santa Cruz Mts and a deep seismic-aseismic transition to the east of the Calaveras fault and continuing on into the Great Valley. The

observed pattern of seismicity is consistent with these predictions, both qualitatively and quantitatively.

Uncertainties

Uncertainties enter into this analysis on a number of levels. First, what is the absolute accuracy of the hypocentral depths reported in the catalogue? The question of absolute accuracy is difficult, if not impossible, to resolve, but it seems clear that even with the best quality locations ±1 km is the minimum uncertainty. In the Loma Prieta area, where lateral velocity discontinuities and the location of the fault at the western edge of the network combine to reduce the absolute accuracy, Dietz and Ellsworth (1993) report six different hypocentral depth estimates for the 1989 earthquake. These vary from 15.6 to 17.85 km for a range of 2.25 km, although many of the techniques applied for locating the mainshock are not applicable to locating the background microseismicity (and vice versa), and relative differences might mask some absolute error inherent in all techniques. However, the various models that relocated aftershocks also yield a similar range of differences in result, suggesting that the high quality catalogue depth determinations for the San Francisco Bay Area are within ±2 km of the true depth.

With the exception of the Loma Prieta area (which is already accounted for in the widths chosen for the SAF), it is most likely that any significant error in the hypocentral depths would be consistent throughout the region (i.e., either too depth or too shallow). For this reason the uncertainties in width for the WG02 report are applied to all segments simultaneously. A recent analysis of earthquake depths in the San Francisco Bay region by Hole et al. (2000) suggests that the shallower hypocenters for the Loma Prieta earthquake are more consistent with the true nucleation depth and confirms the overall accuracy of the hypocentral depths reported by the NCSN elsewhere in the region.

Second, given reasonable accuracy in the hypocentral depths of individual events, how many events are necessary to illuminate the entire depth extent of the seismogenic layer? This is not the question of how microseismicity relates to mainshock rupture extent (see below) but simply how many earthquakes it takes to obtain a statistically robust estimate. With the use of 95% as the cut-off value there typically have to be at least 100 earthquakes (and often many more) in a fault segment to get a stable value. In this case “stable” means an estimate that varies by less than two hundred meters when the population is increased or decreased by 10% (either by changing the length of fault segment studied or by adjusting the time frame of the catalogue search). The “too few eqs” entries in Table1 identify segments for which this stability criterion could not be met over the segment length defined by WG02. As a practical matter this dependence on a minimum number of earthquakes places a lower limit on the length of a fault segment for which the maximum depth can be determined. For the post-1980 seismicity this length is on the order of 20 km for the average active segment of Bay Area faults. In some areas it is possible to reduce this to 10 km, but there are others where there is not enough seismicity to determine a result at the 20 km scale. As a rule of thumb, looking at segments much longer than 20 km tends to average out some apparently real spatial variations in the depth of seismicity, while looking at segments much shorter than 20 km yields spatial variations reflecting inadequate sampling of the seismic record rather than real changes.

Third, how do these results vary by type of event (e.g., background seismicity, aftershocks, mainshocks)? This appendix incorporates all of the "small" events, including aftershocks. There is a reasonable chance that aftershocks, as events located for the most part "outside" of the ruptured fault patch, will extend to depths much greater than the seismogenic crust as defined by the mainshock hypocenter or the depth extent of the seismic source as defined by coseismic rupture. For the two recent significant earthquakes in the Bay Area (Morgan Hill and Loma Prieta), the 95% cut-off is less than 2 km deeper than the mainshock hypocenter (Schaff et al., 2002). This observation is confirmed by most other recent events in California, including Northridge, San Fernando, Whittier Narrows, Coalinga, and Joshua Tree (Williams, 1996; Strehlau and Williams, 1998). One prominent exception to this is the Landers earthquake, which had a very shallow hypocenter (the deepest of all the various relocations places it around 7 km), but this appears to be the exception rather than the rule (Williams, 1996). Most waveform inversions for coseismic slip do not provide independent estimates of the depth extent of rupture because the vertical extent of the model space is typically preset to the depth of the mainshock or the deepest aftershocks. Finding an adequate fit to the waveform data could constitute a test or simply the discovery of a local minimum.

Fourth, what uncertainty should be attached to the numbers tabulated above? The consensus view is that ±2 km is a generally a reasonable value as it covers all of the uncertainties in absolute depth for the earthquakes themselves and allows for some offset between a future mainshock rupture and the background seismicity. The uncertainty for the Greenville fault has been set to ±3 km in order to reflect the unusual variability in the depth of seismicity along the segment.

References

Dietz, L., and Ellsworth, W., 1993, Aftershocks of the 1989 Loma Prieta, California earthquake and their tectonic implications: U.S. Geological Survey Professional Paper I - Earthquake Occurrence, Chapter on Aftershocks and Postseismic Effects, P.A. Reasenberg, ed.

Hill, D.P., Eaton, J.P., and Jones, L.M., 1990, Seismicity, 1980-86, in The San Andreas Fault System, California, U.S. Geological Survey Professional Paper 1515.

Hole, J.A., Brocher, T.M., Klemperer, S.L., Parsons, T., Benz, H.M., and Furlong, K.P., 2000, Three-dimensional seismic velocity structure of the San Francisco Bay area, Journal of Geophysical Research, 105, p.13,859-13,874.

Ross, S.L., Ryan, H.F., and Stephenson, A.J., 1998, San Gregorio Fault zone studies offshore Half Moon Bay and Monterey Bay, CA, EOS, Transactions of the American Geophysical Union, v. 79, p. F613.

Schaff, D.P., Bokelmann, G.H.R., Beroza, G.C., Waldhauser, F. and Ellsworth, W.L., in press, High resolution image of Calaveras Fault seismicity, Journal of Geophysical Research.

Sibson, R.H., 1982, Fault zone models, heat flow, and the depth distribution of earthquakes in the continental crust of the United States, Seismological Society of America Bulletin, v. 72, p. 151-163.

Strehlau, J. and Williams, C., 1998, Temperature and the seismic-aseismic transition on the San Andreas and other active faults in California, Deutsche Geophysikalische Gesellschaft, v. II, p. 106-111.

Walter, S.R., Oppenheimer, D.H., and Mandel, R.I., 1998, Seismicity maps of the San Francisco and San Jose 1° ´ 2° quadrangles, California for the period 1967-1993, U.S. Geological Survey Geologic Investigations Series Map I-2580.

Wells, D. L., and Coppersmith, K. J., 1994, New empirical relationships among magnitude, rupture length, rupture width, rupture area, and surface displacement: Seismological Society of America Bulletin, v. 84, no. 4, p. 974-1002.

Williams, C.F., 1995, Temperature and the seismic/aseismic transition: A new look, EOS Transactions of the American Geophysical Union, v. 76, p. 410.

Williams, C.F., 1996, Temperature and the seismic/aseismic transition: observations from the 1992 Landers earthquake, Geophysical Research Letters, v. 23, n. 16, p.2029-2032.

Working Group on Northern California Earthquake Potential, 1996, Database of potential sources for earthquakes larger than magnitude 6 in northern California, United States Geological Survey Open-File Report, 96-705, 29p.

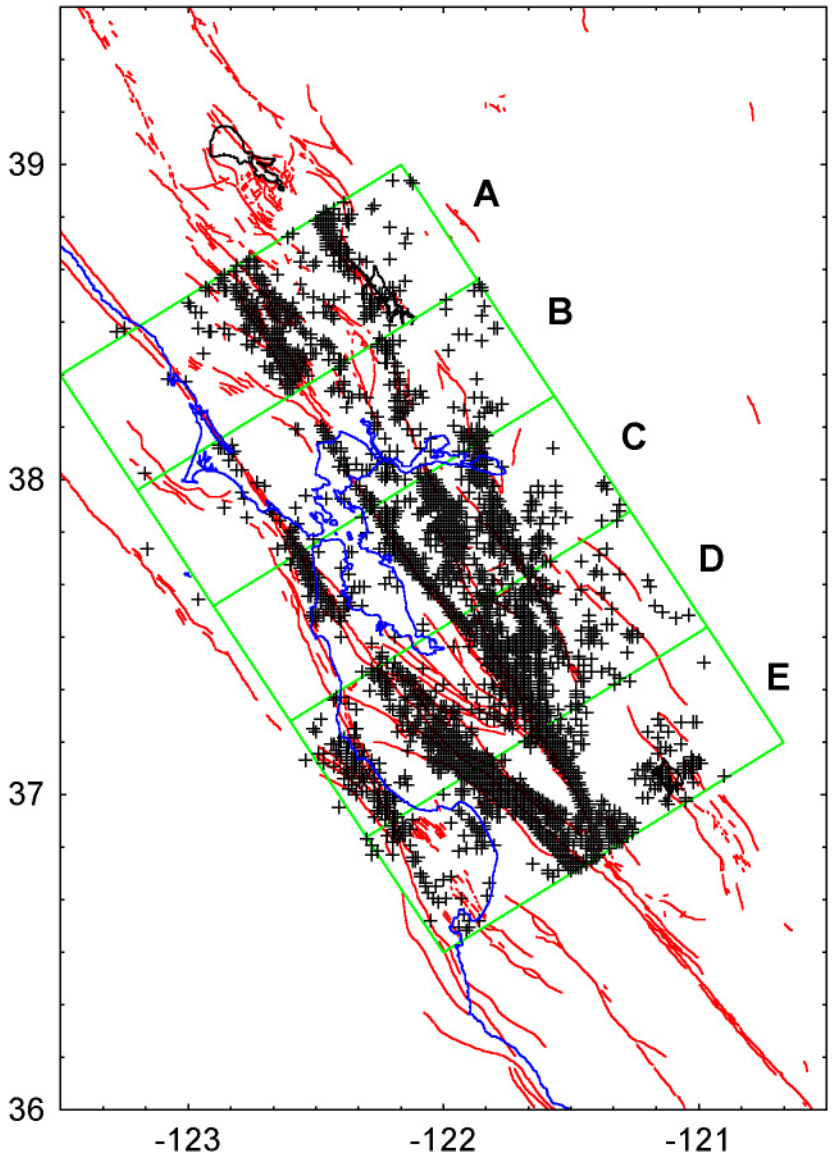

Figure 1. NCSN events of M •1.5 with an rms <0.15 seconds and at least 6 stations recording each event in the years from 1980 to the end of 1998. Lettered boxes define subregions depicted in following figures.

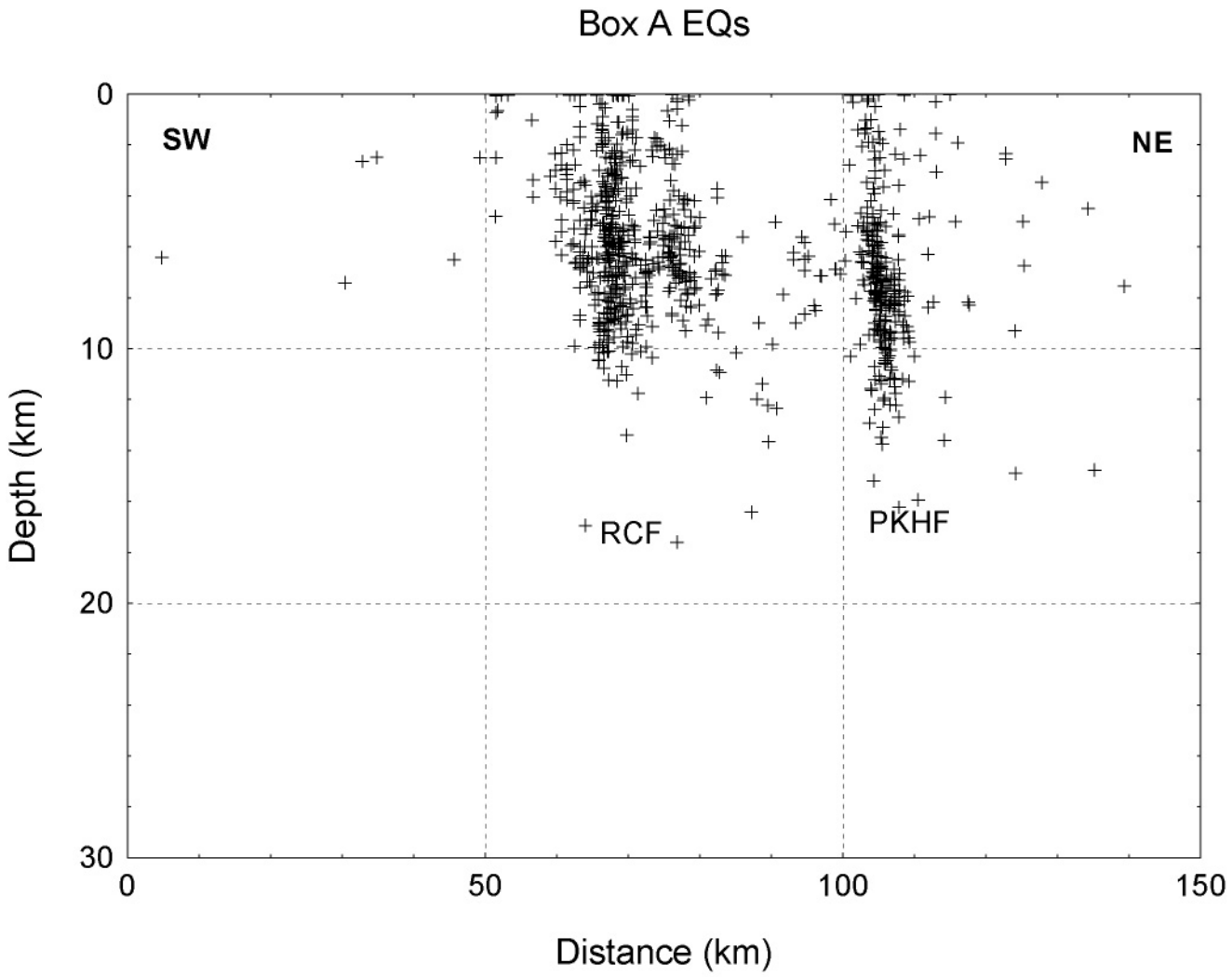

Figure 2. Cross-section of seismicity from Box A of Figure 1.

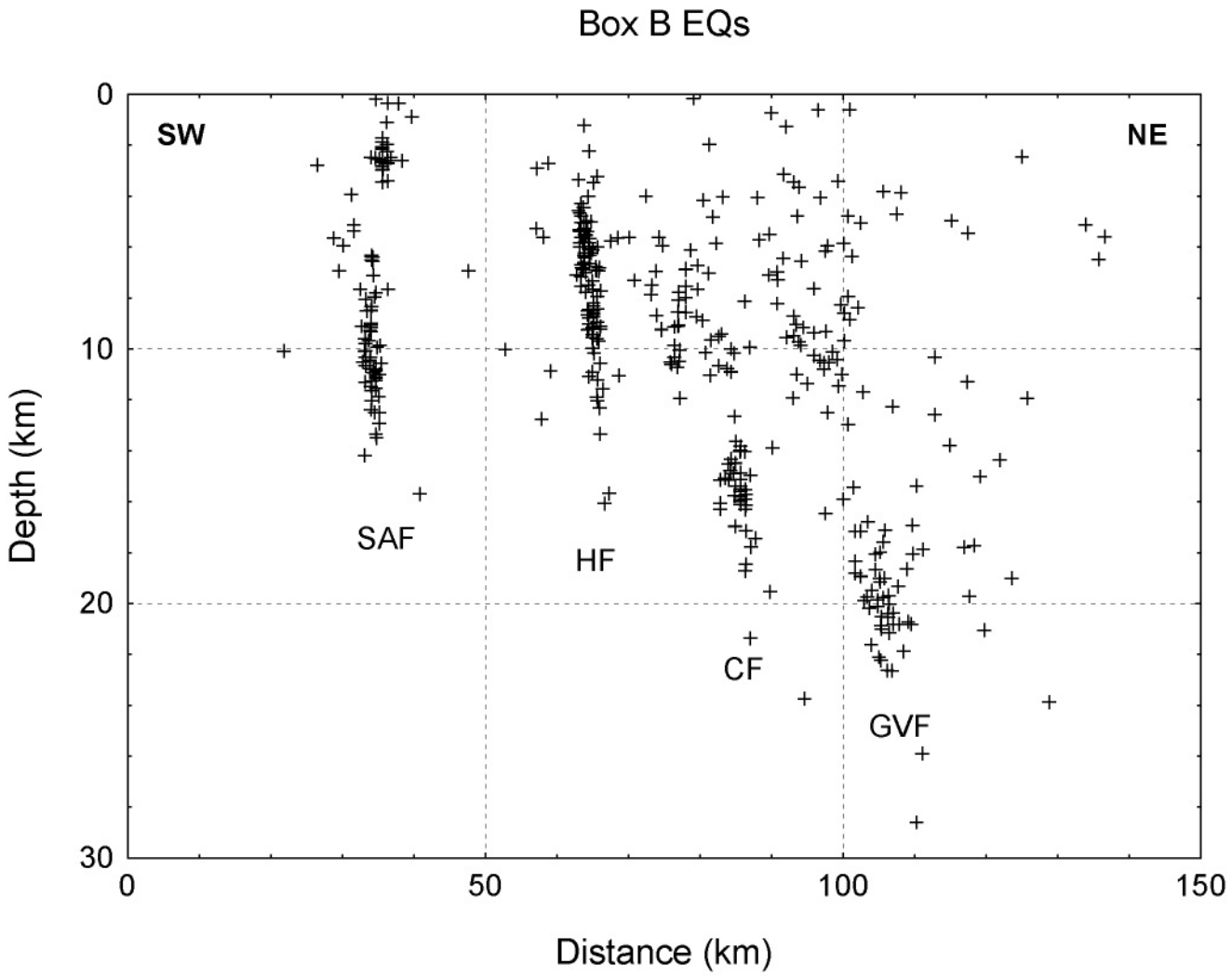

Figure 3. Cross-section of seismicity from Box B of Figure 1.

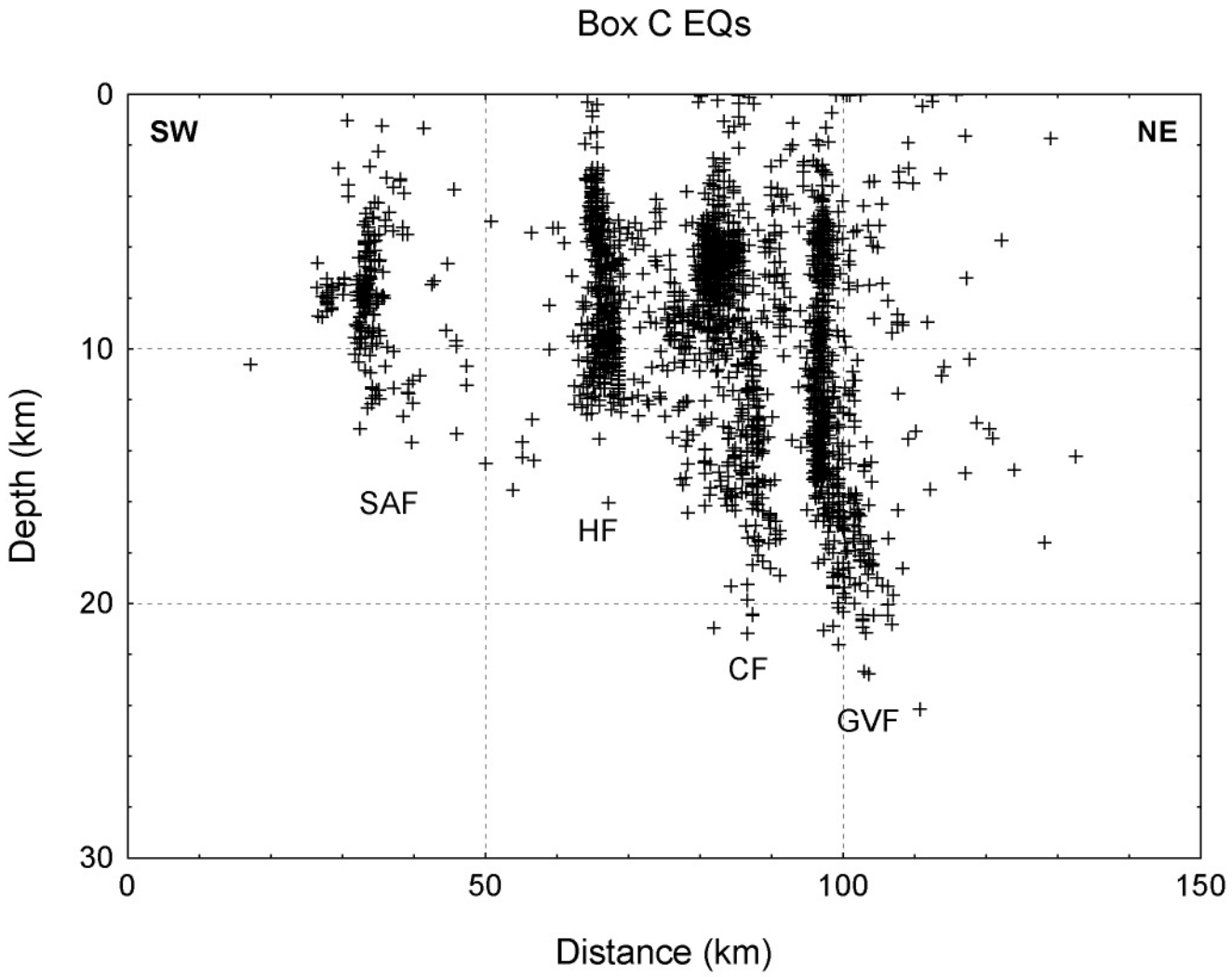

Figure 4. Cross-section of seismicity from Box C of Figure 1.

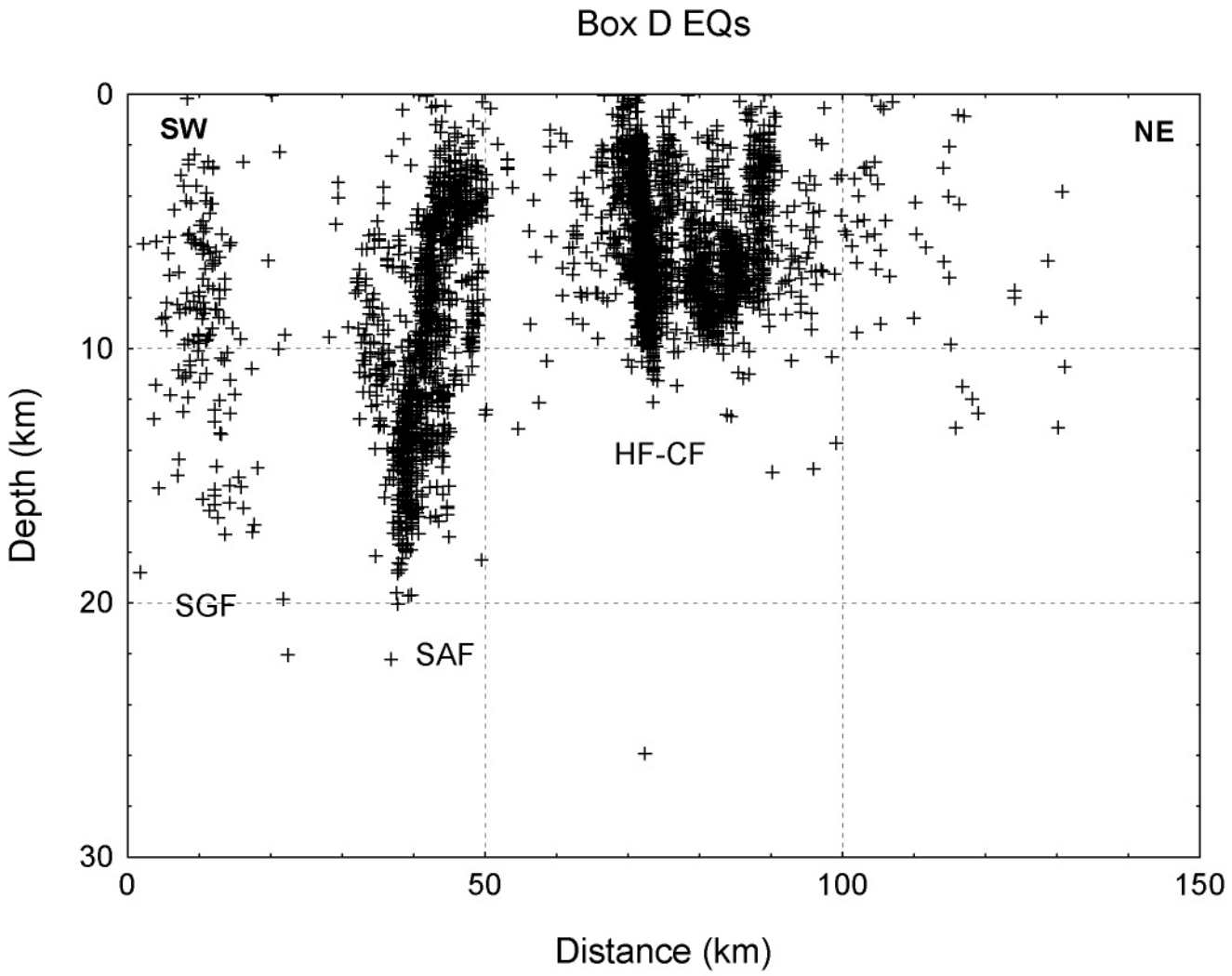

Figure 5. Cross-section of seismicity from Box D of Figure 1.

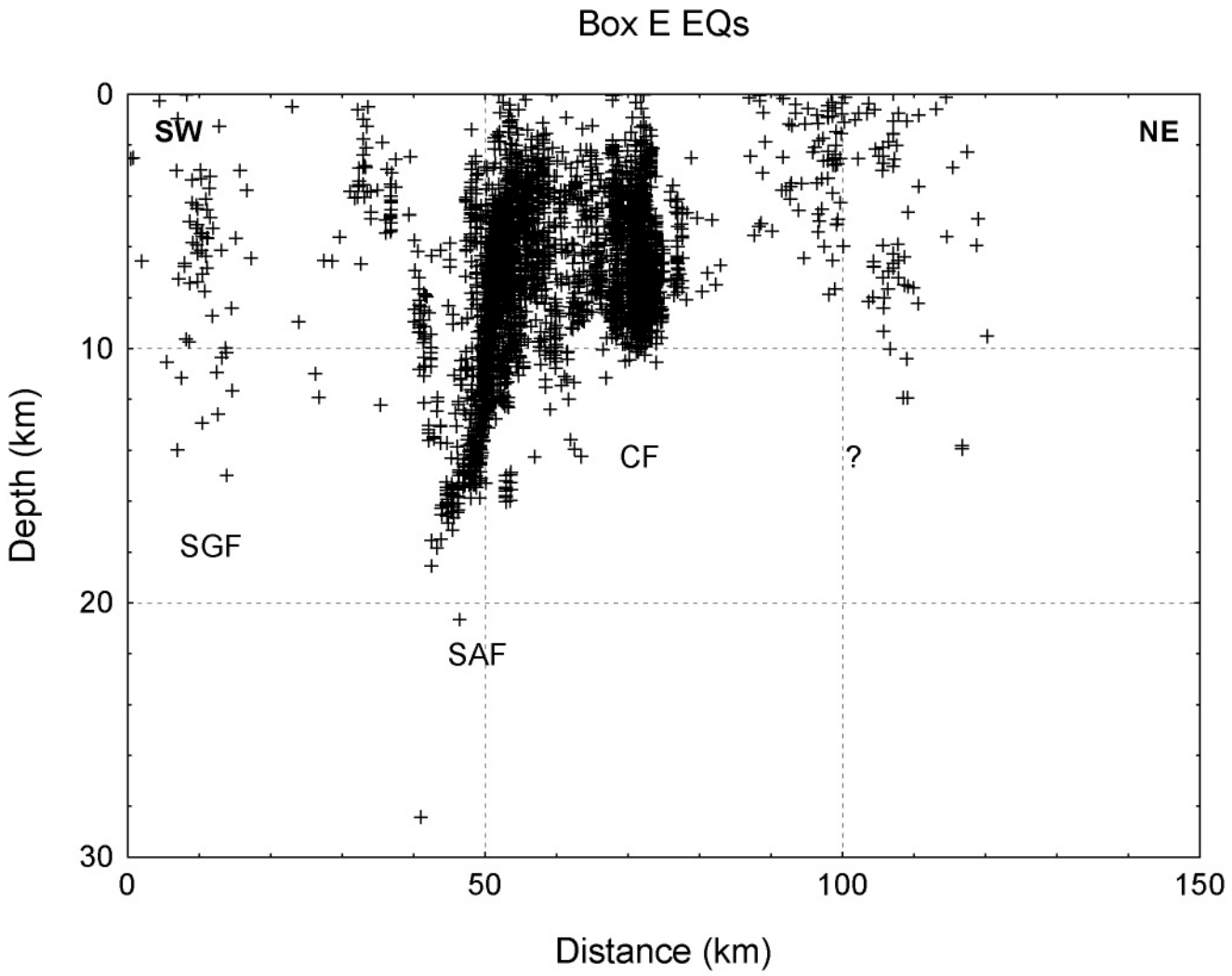

Figure 6. Cross-section of seismicity from Box E of Figure 1.

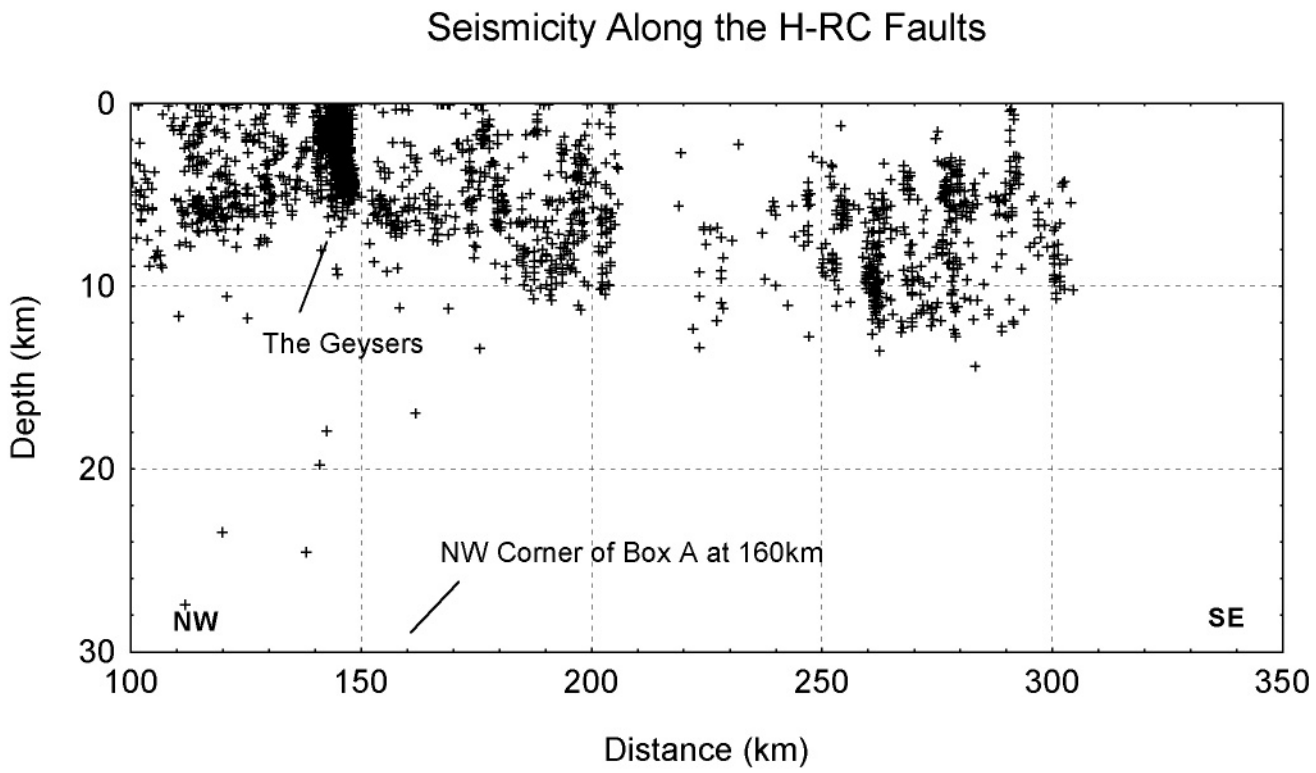

Figure 7. Seismicity cross-section along the Hayward-Rodgers Creek-Maacama fault trend.

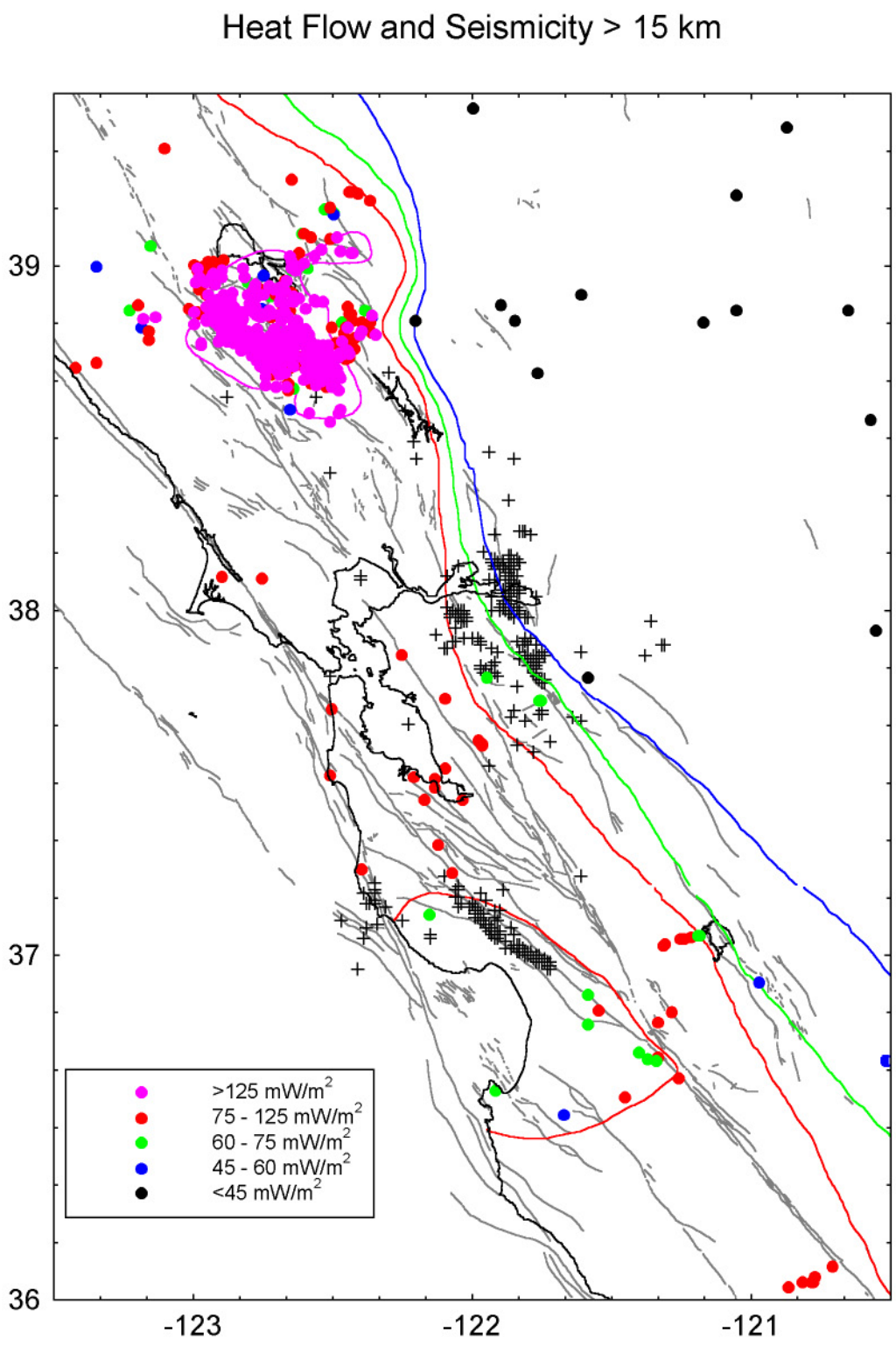

Figure 8. Locations of heat flow measurements in the San Francisco Bay Region. Colored contour lines provide an adequate grouping of the data and a depiction of the thermal regime at seismogenic depths. Black + symbols are epicenters of earthquakes from Figure 1 with depths greater than 15 km.

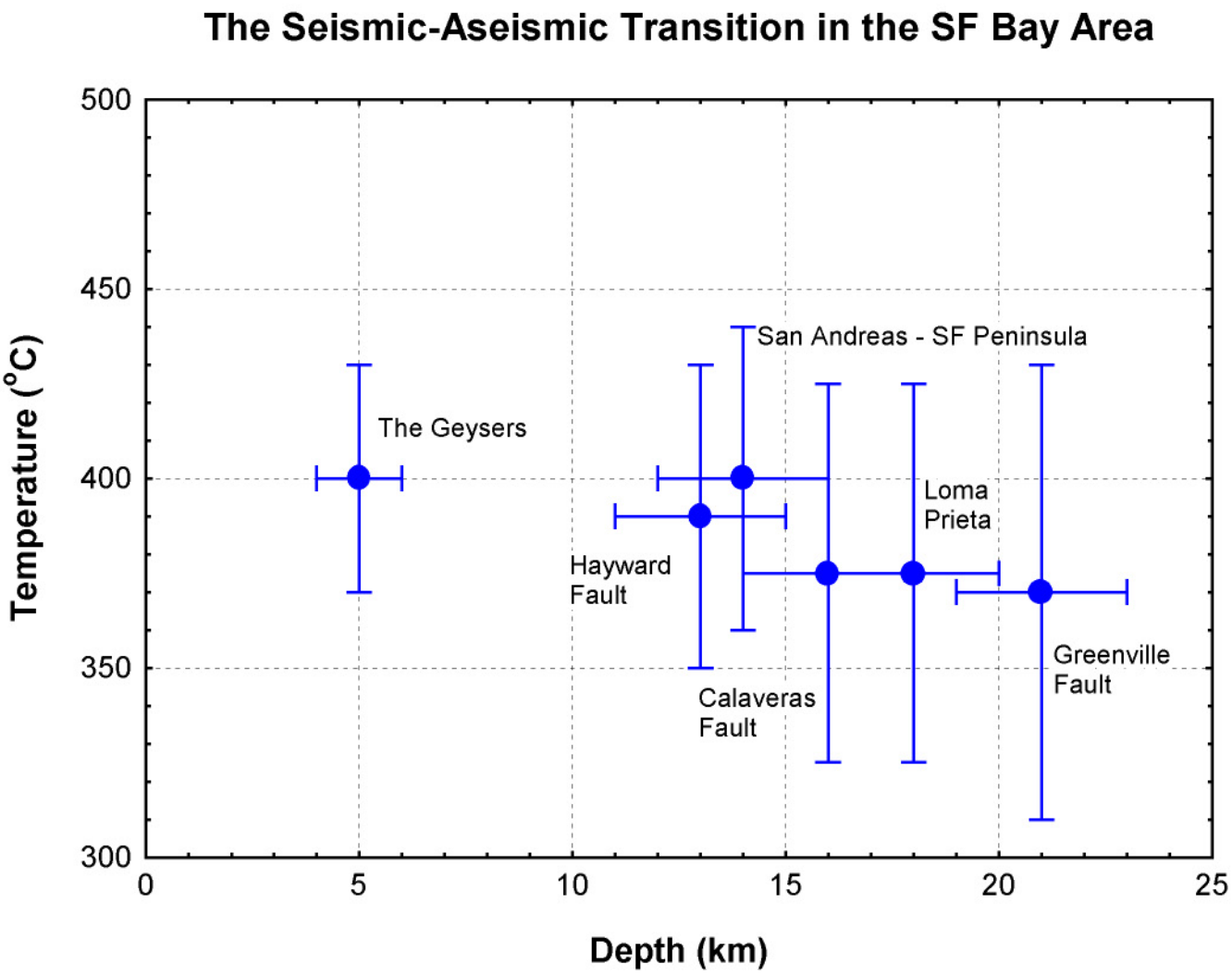

Figure 9. Estimated temperatures at the depths recorded in the table on page 3.

Appendix B

The Seismogenic Scaling Factor, R

William H. Bakun

Elastic waves are generated by slip on a fault. Far away from the causative slip, the amplitude of the elastic waves increases with the velocity of the slipping points on the fault (Aki and Richards, 1980). If slip is rapid, then detectable elastic waves are generated, and an "ordinary" earthquake occurs. If the slip is slow (a *slow earthquake*), then the energy propagated to distant points is small, and damage is minimal. If the slip is very slow (*a silent earthquake*), then no detectable seismic waves are generated (*aseismic slip*) and damage is limited to deformation of structures built across the trace of the slipping fault.

Louderback (1942) notes that geologists have long speculated on the possibility of the slow yielding of crustal rocks such that elastic strain that might result in earthquakes was not accumulated. Such aseismic slip, or *fault creep*, was first recognized in 1956 (Steinbrugge, 1957) on the trace of the San Andreas fault south of Hollister near the south end of the WG99 study area. Fault creep events at the earth's surface are a near-surface soil failure phenomena driven by deeper fault slip (Johnston and Linde, 2001). Fault creep at the surface has since been documented on the Hayward, Calaveras, San Andreas, and Concord faults in the San Francisco Bay region, on the Garlock, Banning, San Andreas, Coyote Creek, Superstition Hills, and Imperial faults in southern California (Louie and others, 1985), and on the Anatolian fault in Turkey (Ambraseys, 1970; Aytun, 1980).

Too important to ignore

Slow earthquakes have been detected in many tectonic settings. Kanamori and Hauksson (1992) described a shallow M_L = 3.5 earthquake associated with oil-field operations near Santa Maria in southern California in which the radiated energy was 1-2 orders of magnitude smaller than that of an ordinary earthquake. Slow earthquakes associated with spreading centers along mid-ocean ridges have been discussed by Beroza and Jordan (1990), and a deep slow earthquake was recently detected on the Cascadia subduction zone (Dragert and others, 2001). Closer to home, slow earthquakes have been detected on borehole strainmeters and associated with slip at depth on the Hayward fault and on the San Andreas fault in the SFBR (Linde and others, 1996; Johnston and Linde, 2001). The slow earthquake in December 1992 on the San Andreas fault near San Juan Bautista was associated with small earthquakes (aftershocks?) that outlined a crescent shape on the fault extending from a few kilometers depth to about 8 kilometers (Johnston and Linde, 2001). The aseismic moment inferred for this slow earthquake was equivalent to an **M** 5.1 ordinary earthquake, but the seismic moment was more than 100 times smaller (Johnston and Linde, 2001). That is, there is convincing evidence that aseismic slip extends to seismogenic depths for faults in the SFBR that are characterized by WG99. Aseismic slip at depth occurs *in lieu* of slip during ordinary earthquakes so that a proper accounting of the extent and amount of aseismic slip at depth is essential for accurate estimates of the probability of future damaging earthquakes.

We don't know what causes a fault to creep. Field evidence suggests that the distribution of weak materials such as serpentinite and the presence of carbon dioxide-rich fluids may be important (Irwin and Barnes, 1975, 1980). Laboratory experiments (e.g., Byerlee and Summers, 1976; Reinen and others, 1994) indicate that the presence of serpentinite, high temperatures, high pore pressures, and a thick zone of fault gouge tend to promote fault creep. In any case, we cannot map these fault attributes at depth, but must estimate the regions of aseismic slip from remote observations. Our primary indicator of the presence of aseismic slip at depth is the observation of surficial fault creep (e.g., Galehouse, 1995). If surficial fault creep is not observed, there is little reason to suspect that it is a significant fault attribute at seismogenic depths. If surficial fault creep is observed, aseismic slip may extend to seismogenic depths beneath that section of that fault and can account for a significant portion of the plate-motion slip rate available for earthquake generation.

How much aseismic slip?

What part of the plate-motion slip rate is accounted for by aseismic slip? It appears that most, if not all, of the plate motion is accommodated by fault creep along the relatively simple section of the San Andreas fault in central California just south of the SFBR (Savage and Burford, 1973). In contrast, 3-10 mm/year of fault creep has been measured since the 1970s along the trace of the south Hayward fault segment, precisely where the Hayward fault slipped in the **M** 6.8 earthquake of October 21, 1868. Clearly this amount of fault creep on the southern Hayward fault cannot extend through the seismogenic depth range. In fact, the inferred depth extent of creep varies along strike from 4 km to the bottom of the seismogenic zone (Simpson and others, 2001). Their models require locked patches under the central Hayward fault, consistent with the earthquake in 1868, but the geometry and extent of locking under the north and south ends of the Hayward fault depend critically on assumptions of fault geometry. Bürgmann and others (2000) suggested from InSAR data and the presence of repeating micro-earthquakes that a 20-km-long section of the northern Hayward fault may be creeping at all depths, precluding the initiation of any large earthquake under that section of fault. Simpson and others' (2001) models contain 1.4-1.7 times more stored moment along this stretch of the Hayward fault than does the model of Bürgmann and others (2000). That is, there is considerable uncertainty regarding the relative importance of aseismic slip on the Hayward fault, and on the other faults characterized by WG99.

WG99's method of accounting for aseismic slip

WG99 accounts for aseismic slip through a seismogenic scaling factor *R* which varies from R = 0, where all of plate-motion slip rate is accounted for by aseismic slip, to R = 1, where all of plate-motion slip rate is accounted for by earthquakes. The values of R used in USGS Open-file Report # 99-517 (see Table) were based on the consensus opinion of an expert group of geologists and geophysicists. The expert group subsequently decided that regional tectonic models based on geodetic observations collected in the SFBR in the last few decades should be the primary basis for the R values used in the final WG99 calculations. The revised R values (see Table above) that are used in this report are based on results of modeling the geodetic data (see Geodetic Modeling Section below), modified in cases by additional information. The rationale for each of the recommended R values is given below.

Fault Segment	USGS OFR 99-517		Revised (23 August 2001)	
	R	Weights	R	Weights
SAS	1	-	0.8/ 0.9 /1.0	.2/.6/.2
SAP	1	-	0.9/ 1.0 /1.0	.2/.6/.2
SAN	1	-	0.9/ 1.0 /1.0	.2/.6/.2
SAO	1	-	0.9/ 1.0 /1.0	.2/.6/.2
HS	0.6/ 0.8 /1.0	.1/.8/.1	0.4/ 0.6 / 0.8	.2/.6/.2
HN	0.3/ 0.6 /0.9	.2/.4/.4	0.4/ 0.6 / 0.8	.2/.6/.2
RC	1	-	0.9/ 1.0 /1.0	.2/.6/.2
CS	0.1/0.4/0.7	.1/.8/.1	0.0/ 0.2 /0.4	.2/.6/.2
CC	0.1/0.4/0.7	.1/.8/.1	0.1/ 0.3 /0.5	.4/.5/.1
CN	0.8/0.9/1.0	.2/.6/.2	0.7/ 0.8 /0.9	.2/.6/.2
CON	0.0/.5/1.0	thirds	0.2/ 0.5 /0.8	thirds
GVS	0.0/.5/1.0	thirds	0.2/ 0.5 /0.8	thirds
GVN	0.0/.5/1.0	thirds	0.2/ 0.5 /0.8	thirds
SGS	1	-	0.8/ 0.9 /1.0	.2/.6/.2
SGN	1	-	0.8/ 0.9 /1.0	.2/.6/.2
GS	1	-	0.8/ 0.9 /1.0	.2/.6/.2
GN	1	-	0.8/ 0.9 /1.0	.2/.6/.2

WG99's method of accounting for aseismic slip using the revised R values can be explained by consideration of Oppenheimer and others' (1990) model for earthquake occurrence on the central and south segments of the Calaveras fault. Oppenheimer and others (1990) model the Calaveras fault as a collection of stuck and creeping patches. All of the slip on the Calaveras fault occurs as fault creep at depths less than 4 kilometers and greater than about 10 kilometers. Ambient microseismicity and aftershocks extend from 4 kilometers depth to about 10 km and defines zones where 1) the slip occurs as small earthquakes and fault creep, or 2) usually aseismic zones. Hypocenters of the $5 < \mathbf{M} < 6\ ^{1}/_{4}$ main shocks occur at depths of 8-9 kilometers near the base of the zone of ambient microearthquakes within the usually aseismic zones. The usually aseismic zones are stuck patches that slip infrequently only during main shocks. Oppenheimer and others' (1990) partition of the 4-10 km seismogenic depth range into a shallow zone where aseismic slip prevails and a 2-km-thick deeper zone where seismic slip prevails might be represented by a value of R of about 1/4 to about 1/3.

WG99 uses R to reduce the width W (depth extent) of the seismogenic zone to that fraction that fails only in "characteristic" or "floating" earthquakes. Since the area of slip =W * length L, R has the effect of scaling the area. Since **M** is calculated from the area, R scales **M**. Less frequent events with larger M are necessary to satisfy the geologic slip rate, so the average recurrence time T decreases with decreasing R. That is, a decrease in R on a fault segment decreases the mean magnitude and the mean recurrence time for segment-rupturing earthquakes.

A different model and method of accounting: R scaling the geologic slip rate

Other models can be devised to account for aseismic slip. Rather than the Oppenheimer and others (1990) model described above, consider a fault that creeps everywhere, but the aseismic slip rate is less than the long-term geologic slip rate. In this model, the difference between the geologic and aseismic slip rates would be accounted for by slip in infrequent segment-rupturing earthquakes. Given this model, R might be used to scale the long-term geologic slip rate, and while the mean magnitude would not change, the mean recurrence time would increase with decreasing R.

For comparison purposes, we calculated a SFBR earthquake model and 30-year conditional probabilities accounting for aseismic slip by scaling the slip rate rather than W. Scaling the slip rate results in larger magnitude earthquakes (more W and more area) and greater recurrence times, both because there is more slip per event for larger events and because there is less slip available to produce earthquakes. The conditional 30-yr probabilities are significantly greater with slip rate scaling. For the Poisson model, the conditional 30-yr probability of at least one M≥6.7 earthquake in the SFBR is 69.9% rather than the 60.6% that is calculated in this report.

Rationale for the R values for fault segments

San Andreas North Coast (SAN). The SAN is the simplest segment of the SAF for which dense relevant geodetic observations are available. There are no significant nearby tectonic structures to complicate the interpretation of the model results for SAN, and there is no known seismic activity or surface creep on SAN since 1906. The recommended R values reflect the model results that imply a fully locked SAN segment. Note that the 0.2 weight for R = 0.9 allows for the possibility of both precursory aseismic slip and creep following a segment-rupturing earthquake (*afterslip*).

San Andreas Offshore (SAO). Like the SAN segment, there is no known seismic activity or surface creep since 1906 on SAO. Since there is no reason to differentiate the SAN and SAO segments, we assume that SAO is a continuation of SAN with the same R.

San Andreas Peninsula (SAP). Creep is not observed on the Peninsula segment (SAP) and small to moderate earthquakes are located within a few kilometers of the fault trace, but appear to be associated with tectonic processes off the SAF trace (Zoback and others, 1999). Unlike the SAN segment, the interpretation of the geodetic observations are complicated by the nearby San Gregorio fault. Also, the calculated R tradeoff with the loading rates assumed for the SAP segment (see Geodetic Modeling section below). Since there is no convincing basis for differentiating the SAP and SAN segments, we assume that SAP is a continuation of SAN with the same R.

San Andreas Santa Cruz Mtns (SAS). The SAS is different from the SAF segments to the northwest. Surface creep is clearly observed near San Juan Bautista along the southeast 10% of the SAS segment. Also, there are repeating clusters of microearthquakes on the SAS segment near San Juan Bautista (Rubin and others, 1999), and repeating clusters of microearthquakes have been suggested as a diagnostic of creep on a fault at depth (Nadeau et al, 1995). The

interpretation of the models of the geodetic data is complicated by creep on the nearby Sargent fault. Also, the depth to the base of the seismogenic zone is significantly greater in the northwest part of the SAS than in the southeast, and the model results are likely to underestimate R since they assume a constant intermediate depth. The recommended R reflects a locked SAS, but with creep in the southeast most 10% of the segment.

Hayward South (HS). The 52-km-long HS segment has been creeping at the surface at average long-term rates of 3-10 mm/yr for as long as careful observations have been made, with a 5-6 year slowdown at the south end following the 1989 Loma Prieta earthquake (Lienkaemper and others, 2001). The geodetic models (see Geodetic Modeling Section below) suggest R = 0.50 ± 0.2. Savage and Lisowski (1993) presented a two-dimensional model of the Hayward fault with a 5-km tall creeping zone over a 5-km tall locked zone. The creeping zone was driven by 10-km deep horizontal screw dislocations representing deep slip under the Hayward, Calaveras, and San Andreas faults. In their model, 50% of the area is strictly locked, but retarded creep in the creeping zone accounts for an additional 20-30% of the moment budget, for a total stored moment of 70-80%. Three-dimensional models (Bürgmann and others, 2000; Simpson and others, 2001) of a creeping zone over locked regions yield similar results. Approximately 40% of the area in these models is strictly locked, but 70-80% of the total moment budget is stored in locked areas or areas of retarded creep. The key unknown is how much of the moment stored as retarded creep is released coseismically as opposed to postseismically as afterslip. If all the stored moment were released as afterslip, R = 0.8, whereas if only the strictly locked regions contribute, R=0.4. Since the truth is probably somewhere in between, the panel chose R=0.6 as the central value.

Hayward North (HN). The 35-km long HN segment was assigned R values identical to HS. Geodetic models (see report below) suggest R = 0.66 ± 0.2. Bürgmann and others (2000) have proposed that a 20-km long part of the HN has no locked regions, but creeps from top to bottom. There are locked regions in their model to north and south of this part, however, and the locked-area percentages for HS models are slightly smaller than for HN models, but not significantly so, rounding to identical values as for HN. Given the uncertainties, the panel decided to use R values for HN identical to HS.

Rodgers Creek (RC). Although microearthquakes are located along the RC fault, there is no evidence of surface creep on the fault. There is geologic evidence for surface-rupturing earthquakes on the RC fault and the southern end of the segment is a likely location for the 31 March 1898 **M**6.3 “Mare Island” earthquake (Bakun, 1999). The models of the geodetic data for the RC fault imply a loading rate significantly greater than the long-term geologic rate used in the WG99 calculation sequence. The recommended R reflects a locked Rodgers Creek fault.

Calaveras South (CS). The19-kilometer-long CS segment is characterized by surface creep (14 mm/yr) and frequent small- and moderate-size earthquakes. There have been no significant historical earthquakes and there is no evidence for or against paleoearthquakes on the CS segment. Several studies have concluded that observed strain in the crust near the CS segment is consistent with rigid block motion with steady slip on the CS segment at the plate-motion rate. Although microearthquakes occur along the nearby Quien Sabe fault, this fault is not characterized by WG99 so that the interpretation of the models of the geodetic data for the CS

segment is complicated by un-modeled slip on the nearby Quien Sabe fault. The recommended R for the CS segment is appropriate for a creeping fault with a possibility of infrequent segment-rupturing earthquakes.

Calaveras Central (CC). Observed surface creep decreases northward along the Calaveras fault from 14 mm/yr in the CS segment and southern CC segment to a few mm/yr near the northern end of the CC segment. Several **M** < 6.5 historical earthquakes (**M**6.3 on 20 June 1897, **M**6.2 on 1 July 1911, **M**5.9 on 6 August 1979, and **M**6.2 on 24 April 1984) have occurred on the CC segment (Bakun, 1999). There is some geologic evidence for **M**7 earthquakes on the CC segment. The recommended R for the CC segment is appropriate for a fault with both creeping and locked patches at seismogenic depth as suggested by Oppenheimer and others (1990) that fails infrequently in **M**7 events associated with rupture of CN.

Calaveras North (CN). There is no evidence for any fault creep on the CN segment, except near Calaveras Reservoir at the southern end of the CN segment. There is clear geologic evidence for paleoearthquakes on the CN segment and several moderate-size nineteenth-century earthquakes may have occurred on the CN segment. The models of the geodetic data for the CN segment are not appropriate because the geodetic data imply a loading rate significantly greater than the long-term geologic rate used in the WG99 calculation sequence. The recommended R for the CN segment is appropriate for a locked fault with some creep at the southern end of the segment.

Concord (CON). Although the M_L5.4 earthquake on 24 October 1955 apparently occurred on the Concord fault (Bolt and Miller, 1975), there is no evidence for or against surface-rupturing earthquakes on the Concord fault. Surface creep is observed on the Concord fault. The recommended R for the Concord fault is appropriate for a fault with both creeping and locked patches at seismogenic depth.

Green Valley South and North (GVS and GVN). There is evidence for both surface creep and for surface-rupturing earthquakes on the Green Valley fault. Since there is no basis for differentiating the Green Valley South segment (GVS) and the Green Valley North segment (GVN) segments, the recommended R for the GVS and GVN segments is appropriate for a fault with both creeping and locked patches at seismogenic depth.

San Gregorio South and North (SGS and SGN). There is no evidence of creep on either the San Gregorio South segment (SGS) or the San Gregorio North segment (SGN). While there are some small- and moderate-size earthquakes located near the SGS segment (e.g., two M_S 6.1 earthquakes in 1926), few earthquakes are located near the SGN segment except at its northern end where it merges into the SAF near the Golden Gate. There is some evidence for paleoearthquakes on the SGN segment. Since the San Gregorio fault is located almost entirely offshore, there is little geodetic control on the slip at depth so the geodetic models are not useful. Since there is no basis for differentiating the SGN and SGS segments, the recommended R for the SGS and SGN segments is appropriate for a primarily locked fault.

Greenville South and North (GS and GN). The **M**5.8 and **M**5.4 Livermore earthquakes in 1980 (Bolt and others, 1981) occurred on the Greenville North segment (GN), and there is evidence for surface-rupturing earthquakes on the Greenville South segment (GS) in the last 1000 years.

Afterslip (surface fault creep following an earthquake) was observed following the 1980 Livermore earthquakes. There is no other evidence of creep on the Greenville fault. The recommended R for the GN and GS segments is appropriate for a primarily locked fault.

Mount Diablo Thrust (MTD). There is no evidence for either earthquakes or fault creep on the blind MTD. The R =1 is an assertion that our characterization of the MTD is a valid source model for the generation of earthquakes.

References Cited

Aki, K., and Richards, P.G., 1980, Quantitative seismology: Theory and methods: San Francisco, W.H. Freeman.

Ambraseys, N.N., 1970, Some characteristic features of the Anatolian fault zone: Tectonophysics, v. 9, p. 143-165.

Aytun, A., 1980, Creep measurements in the Ismetpasa region of the North Anatolian fault zone, in Isakara, A.M., and Vogel, A., eds., Multidisciplinary approach to earthquake prediction 2: Braunschweig/Wiesbaden, Friedrich Vieweg & Sohn, p. 279-292.

Bakun, W. H., 1999, Seismic activity of the San Francisco Bay region: Seismological Society of America Bulletin, v. 89, p. 764-784.

Beroza, G., and Jordan, T., 1990, Evidence for slow earthquake rupture from 10 years of continuously-monitored normal-mode activity: Seismological Research Letters, v. 61, p. 27.

Bolt, B.A., and Miller, R., 1975, Catalogue of earthquakes in northern California, Jan 1. 1910 - Dec. 31, 1972: Seismographic Stations, Univ. of California, Berkeley, 567 p.

Bolt, B.A., McEvilly, T.V., and Uhrhammer, R.A., 1981, The Livermore Valley, California, sequence of January 1980: Seismological Society of America Bulletin, v. 71, p. 451-463.

Bürgmann, R.D., Schmidt, R.M., Nadeau, M., d'Alessio, Fielding E., Manaker D., McEvilly T.V., and Murray, M.H., 2000, Earthquake potential along the northern Hayward fault: Science v. 289, p. 1178-1182.

Byerlee, J.D., and Summers, R., 1976, A note on the effect of fault gouge thickness on fault stability: Intl. J. Rock Mech. Min. Sci., v. 13, p. 35-36.

Dragert, H., Wang, K., and James, T.S., 2001, A silent slip event on the deeper Cascadia subduction interface: Science, v. 292, p. 1525-1528.

Galehouse, J.S., 1995, Theodolite measurements of creep rates on San Francisco Bay region faults: U.S. Geological Survey Open-file Report 95-210.

Irwin, W.P., and Barnes, I., 1975, Effect of geologic structure and metamorphic fluids on seismic behavior of the San Andreas fault system in central and northern California: Geology, v. 3 , p. 713-716.

Irwin, W.P., and Barnes, I., 1980, Tectonic relations of carbon dioxide discharges and earthquakes: Journal of Geophysical Research, v. 85, p. 3115-3121.

Johnston, M.J.S., and Linde, A.T., 2001, Implications of crustal strain during conventional, slow and silent earthquakes: Intl. Handbook of Earthquake and Engineering Geology, Academic Press, in press.

Kanamori, H., and Hauksson, E., 1992, A slow earthquake in the Santa-Maria Basin, California: Seismological Society of America Bulletin, v. 82, p. 2087-2096.

Lienkaemper, J.J., Galehouse, J.S., and Simpson, R.W., 2001, Long-term monitoring of creep rate along the Hayward fault and evidence for a lasting creep response to 1989 Loma Prieta earthquake: Geophysical Research Letters, v. 28, p. ???.

Linde A.T., Gladwin, M.T., Johnston, M.J.S., Gwyther, R.L., and Bilham, R., 1996, A slow earthquake sequence on the San Andreas fault: Nature, v. 383, p. 65-68.

Louderback, G.D., 1942, Faults and earthquakes: Seismological Society of America Bulletin, v. 32, p. 305-330.

Louie, J.N., Allen, C.R., Johnson, D.C., Haase, P.C., and Cohn, S.N., 1985, Fault slip in southern California: Seismological Society of America Bulletin: v. 75, p. 811-833.

Nadeau, R.M., Foxall, W., and McEvilly, T.V., 1995, Clustering and periodic recurrence of microearthquakes on the San Andreas fault at Parkfield, California: Science, v. 267, p. 503-507.

Oppenheimer, D.H., Bakun, W.H., and Lindh, A.G., 1990, Slip partitioning of the Calaveras fault, California, and prospects for future earthquakes: J. Geophys. Res., v. 95, p. 8483-8498.

Reinen, L.A., Weeks, J.D., and Tullis, T.E., 1994, The frictional behavior of lizardite and antigorite serpentinites: experiments, constitutive models, and implications for natural faults: Pageoph, v. 143, p. 317-358.

Rubin, A.M., Gillard, D., and Got, J.-L., 1999, Streaks of microearthquakes along creeping faults: Nature, v. 400, p. 635-641.

Savage, J.C., and Burford, R.O., 1973, Geodetic determinaton of relative plate motion in central California: Journal of Geophysical Research, v. 78, p. 832-845.

Savage, J.C., and Lisowski, M., 1993, Inferred depth of creep on the Hayward fault, Central California: Journal of Geophysical Research, v. 98, p. 787-794.

Simpson, R.W., Lienkaemper, J.J., and Galehouse, J.S., 2001, Variations in creep rate along the Hayward fault, California, interpreted as changes in depth of creep: Geophysical Research Letters, v. 28, p. 2269-2272.

Steinbrugge, K.V., 1957, Building damage on the San Andreas fault: report dated February 18, 1957, published by the Pacific Fire Rating Bureau for private circulation.

Zoback, M.L., Jachens, R.C., and Olson, J.A., 1999, Abrupt along-strike change in tectonic style: San Andreas fault zone, San Francisco Peninsula: Journal of Geophysical Research, v. 104, p. 10,719-10,742.

Appendix C: R-factors Inferred from Geodetic Modeling

W. Prescott, D. Manaker, R. Simpson, and W. Ellsworth
17 July 2000

Summary

In assigning final R-factors to the faults, the working group combined geologic and geodetic estimates of fault slip and other information about the behavior of the segments. In this section we summarize the geodetic results.

Using geodetic data, we have estimated values for the R-factors on San Francisco Bay area faults. The geodetically estimated R-factors are summarized and compared to the Working Group 99 Report (USGS Open-File 99-517, 1999) in Table 1.

Table 1. Geodetically inferred R-Factor estimates.

Name	*Code*	*WG99 Open-File 99-517*			*Suggested by this study*	
		R	*2-sigma*	*Wgts*	*R*	*2-sigma*
SAF - Santa Cruz Mtns	SAS	1.0	-	-	0.9	0.2
SAF - Peninsula	SAP	1.0	-	-	0.8	0.2
SAF - North Coast	SAN	1.0	-	-	1.0	0.1
SAF - Offshore	SAO	1.0	-	-	1.0	0.1
Hayward South	HS	0.8	0.2	.1/.8/.1	0.5	0.8
Hayward North	HN	0.6	0.3	.2/.4/.4	0.7	0.6
Rodgers Creek	RC	1.0	-	-	0.9	0.4
Calaveras South	CS	0.4	0.3	.1/.8/.1	0.1	0.5
Calaveras Central	CC	0.4	0.3	.1/.8/.1	0.6	0.3
Calaveras North	CN	0.9	0.1	.2/.6/.2	0.9	0.4
Concord	CON	0.5	0.5	thirds	1.0	0.3
Green Valley South	GVS	0.5	0.5	thirds	1.0	0.2
Green Valley North	GVN	0.5	0.5	thirds	1.0	0.2
San Gregorio South	SGS	1.0	-	-	0.7	0.8
San Gregorio North	SGN	1.0	-	-	0.7	0.8
Greenville South	GS	1.0	-	-	0.7	1.0
Greenville North	GN	1.0	-	-	0.7	0.9
Mount Diablo Thrust	MTD	1.0	-	-	-	-

Notes: The central R-factors are taken from Table 3 below, with the R-factors rounded to 0.1 unit. The 2-sigma uncertainties shown here are twice those shown in Table 3.

For the San Andreas, Calaveras, Rodgers Creek faults, the geodetically estimated R-factors are consistent with the WG99 Open-File. For the remaining faults, the values and/or the uncertainties suggested by this study are somewhat different than the WG99 Open-File. These differences are discussed in more detail below, but part of the explanation is that the geodetic observations require higher-than-geologic slip rates on the deep portions of some of the faults.

Introduction

Using geologic data (dated offset features), Working Group 1999 (WG99) arrived at a consensus geologic rate for 18 fault segments in the San Francisco Bay Area. In addition WG99 estimated the fraction of the geologic slip that occurs through seismic processes and, by implication, what fraction is released by other mechanisms (creep, inelastic deformation). WG99 refers to this ratio as the R-factor and tabulates an estimate of R-factors and their distribution for the WG99 faults. An R-factor of 1.0 implies that a fault is completely locked between seismic events and that all of the geologic slip occurs during seismic events.

We have used a set of geodetic observations from the San Francisco Bay area to provide an independent estimate of these R-factors. The relation is simple in principle:

$R = 1 - b_s/b_l$
b_s= slip rate at seismogenic depths ("s" for seismogenic slip),
b_l = slip rate at greater depths ("l" for lower slip).

Our original strategy was to estimate b_s from the geodetic data and use the WG99 geologic rates for b_l. However, the geodetic data and the geologic data appear inconsistent for some faults, and these definitions led to unlikely values for some R-factors. Thus, instead we estimated both b_s and b_l from the geodetic data. Both sets of values are given below, the geodetic/geologic set in Table 2 and the geodetic/geodetic set in Table 3. The values in the summary table come from the geodetic/geodetic set.

Input data

All of the input data files are listed in the appendix and accessible on the web. The data consisted of:

- Trilateration data collected between, roughly, 1971 and 1991;
- GPS data collected between, roughly, 1992 and 1999;
- Creep rates (Lienkaemper, pers comm.):
  HN & HS 4.5 mm/yr
  CS & CC 15.0 mm/yr
  CN 1.5 mm/yr
  CON 3.5 mm/yr
  Other faults 0.0 mm/yr
- 18 fault segments as given by WG99 with three locations for each end of each segment;
- 3 depth ranges for each fault segment, 0-3 km, 3-W km, W-5000 km,
  where width, W, is variable and sampled from WG99 distribution;
- 15 additional faults extending outside the primary area of WG99 interest;

- 10,000 samples of segment endpoints, and widths drawn from the WG99 distribution (only the first 100 have been used);
- 10,000 samples of geologic slip rates for each of the segments drawn from the WG99 distribution (only the first 100 have been used).

In addition, the following assumptions were imposed on the solution:

- Slip in the shallowest layer for all segments was constrained to the estimated creep rate;
- Slip on the north and south pieces of many segments were constrained to be the same;
- Conservation of the Burgers vector was weakly imposed at fault triple junctions (e.g., where the San Gregorio fault merges with the San Andreas fault);
- In one of the two models discussed below, slip in the deepest layer is constrained to geologic rates; in the other slip is free in both the seismogenic and deep layer.

Results

The results are most easily summarized with tables:

Table 2. Slip rate estimates and R-factors when deep slip is constrained to geologic rates.

Name	*Code*	*La1Slp*	*La1Std*	*La2Slp*	*La2Std*	*R*	*Rstd*
		mm/yr	mm/yr	mm/yr	mm/yr		
SAF - Santa Cruz Mtns	SAS	4.62	1.68	17.12	0.20	0.73	0.10
SAF - Peninsula	SAP	3.58	1.54	17.12	0.20	0.79	0.09
SAF - North Coast	SAN	0.54	0.62	24.09	0.20	0.98	0.03
SAF - Offshore	SAO	0.54	0.71	24.09	0.20	0.98	0.03
Hayward South	HS	7.18	2.10	8.82	0.20	0.19	0.24
Hayward North	HN	8.22	2.21	8.82	0.20	0.07	0.25
Rodgers Creek	RC	11.10	2.60	8.92	0.20	-0.24	0.29
Calaveras South	CS	20.92	2.99	14.67	0.20	-0.43	0.20
Calaveras Central	CC	14.54	2.08	14.67	0.20	0.01	0.14
Calaveras North	CN	6.81	2.57	5.78	0.20	-0.18	0.45
Concord	CON	10.83	3.38	4.06	0.20	-1.67	0.84
Green Valley South	GVS	14.05	2.59	5.14	0.20	-1.73	0.51
Green Valley North	GVN	14.06	2.59	5.19	0.20	-1.71	0.51
San Gregorio South	SGS	1.19	1.60	4.24	0.20	0.72	0.38
San Gregorio North	SGN	1.20	1.61	5.52	0.20	0.78	0.29
Greenville South	GS	6.11	3.02	1.85	0.20	-2.30	1.67
Greenville North	GN	6.11	3.02	1.85	0.20	-2.30	1.67
Mount Diablo Thrust	MTD	0.00	0.13	0.00	0.04		

Notes: Estimated Slip in seismogenic layer (La1) from 3 km depth to about 12 km depth (exact depth to the bottom varies with segment and sample). The entries are the average over 100 samples. Also shown is the average geologic slip rate (La2). In this solution, La2 was strongly constrained. All standard deviations are one sigma.

Table 3. Slip rate estimates and R-factors when deep slip is estimated from geodetic data.

Name	*Code*	*La1Slp*	*La1Std*	*La2Slp*	*La2Std*	*R*	*Rstd*
		mm/yr	mm/yr	mm/yr	mm/yr		
SAF - Santa Cruz Mtns	SAS	2.34	1.69	23.24	4.50	0.90	0.08
SAF - Peninsula	SAP	2.56	1.68	15.38	3.23	0.83	0.11
SAF - North Coast	SAN	0.24	0.85	21.65	2.17	0.99	0.04
SAF - Offshore	SAO	0.24	0.98	21.65	2.18	0.99	0.05
Hayward South	HS	3.39	2.20	7.27	3.89	0.53	0.39
Hayward North	HN	2.38	2.48	8.79	3.23	0.73	0.30
Rodgers Creek	RC	1.66	2.84	14.89	2.85	0.89	0.19
Calaveras South	CS	16.70	2.84	19.60	4.08	0.15	0.23
Calaveras Central	CC	8.40	2.47	19.23	3.14	0.56	0.15
Calaveras North	CN	1.77	2.15	12.32	5.05	0.86	0.18
Concord	CON	0.00	2.50*	16.64	3.18	1.00	0.15
Green Valley South	GVS	0.00	2.50*	20.18	2.23	1.00	0.12
Green Valley North	GVN	0.00	2.50*	20.20	2.23	1.00	0.12
San Gregorio South	SGS	1.84	2.18	5.91	2.54	0.69	0.39
San Gregorio North	SGN	1.86	2.18	5.91	2.54	0.69	0.39
Greenville South	GS	1.59	2.31	5.32	3.47	0.70	0.48
Greenville North	GN	1.60	2.30	5.32	3.47	0.70	0.47
Mount Diablo Thrust	MTD	0.00	0.16	0.00	0.08		

Notes: Estimated Slip in seismogenic layer (La1) from 3 km depth to about 12 km depth (exact depth to the bottom varies with segment and sample). The entries are the average over 100 samples. Also shown is the estimated slip in the deeper layer from about 12 km to infinity essentially. Entries with 0 slip and standard deviation were forced to 0 to avoid negative slip values. All standard deviations are one sigma. (*) indicates assumed values; since slip was constrained to zero, no uncertainty is calculated.

Discussion

Tables 2, 3, and 4 contain three estimates of the R-factors and their uncertainties. In Table 2, the R-factor displayed for each fault is calculated from the mean value of 100 calculations for geodetic fault slip in the seismogenic layer with the deep slip constrained to the geologic rate. The standard deviation in Table 2 is mean of the standard deviation calculated for each of the 100 cases. These standard deviations reflect the uncertainties in the observations (trilateration and GPS) and the ability of the model to resolve fault slip. The R-factors and standard deviations in Table 3 are similar, except that in this case both the seismogenic and deep slip are estimated from the geodetic data. In Table 4, the R-factors are calculated slightly differently. Rather than calculate a mean slip over 100 cases and then turn that into a single R-factor, we calculate the R-factor for each case for each fault. Table 4 contains the median values for these R-factors and a standard deviation computed from the 100-sample distribution.

Fig.1 is a histogram of these R values over 100 cases, and Fig. 2 illustrates the variation of the R-factors with slip rate in the lower layer. From Fig.2 it is apparent that for some faults the R-factor correlates strongly with the slip rate in the deep layer and for some faults it does not. Along the San Andreas and San Gregorio fault segments, there is little or no correlation (Fig. 2) between R and deep slip; while, for the other faults, there is usually a strong correlation. Another way of

Table 4. Median R-factor and standard deviations estimated from variation with model geometry and rate.

Name	*Code*	*R*	*Rstd*
SAF - Santa Cruz Mtns	SAS	0.91	0.03
SAF - Peninsula	SAP	0.87	0.04
SAF - North Coast	SAN	1.0	0.02
SAF - Offshore	SAO	1.0	0.02
Hayward South	HS	0.5	0.12
Hayward North	HN	0.66	0.09
Rodgers Creek	RC	0.89	0.03
Calaveras South	CS	0.18	0.08
Calaveras Central	CC	0.46	0.07
Calaveras North	CN	0.84	0.07
Concord	CON	0.96	0.01
Green Valley South	GVS	0.95	0.01
Green Valley North	GVN	0.95	0.01
San Gregorio South	SGS	0.77	0.12
San Gregorio North	SGN	0.76	0.13
Greenville South	GS	0.76	0.05
Greenville North	GN	0.76	0.05
Mount Diablo Thrust	MTD		

Notes: These R-factors and their standard deviations were calculated from the variation of R over the 100 cases. See the Discussion Section for a fuller description. All standard deviations are one sigma.

saying the same thing is that to note that, for the western faults, the deep slip rate and the seismogenic slip rate are positively correlated, so that R (which is essentially a ratio between the seismogenic and deep slip) is uncorrelated with either. Whereas, for the eastern faults, the seismogenic and deep slips tend to be negatively correlated. Low deep slip rates correspond to higher seismogenic slip rates and visa-versa.

Tables 3 and 4 provide similar estimates of the R-factors. The standard deviations in Table 4 are smaller than the data- and model-driven standard deviations in Table 3. In the summary to this writeup, Table 1, we used the common R-factors from Tables 2/3 and the standard deviations from Table 3. However, in assigning final R-factors to the faults, the working group took into account the distribution of R-factors for each fault, Fig.1, and the correlation with slip rate, Fig. 2, as well as other factors (see the Aseismic Slip section).

San Andreas and San Gregorio faults (SAS, SAP, SAN, SAO, SGS, SGN)

For the west bay faults, the results of geodesy and the geology seem fairly consistent. The geodetic models give low rates of slip in the seismogenic zone (La1Slp). And the deep slip rates (La2Slp) in Table 3, where this is a free parameter, are in reasonable agreement with the corresponding values in Table 2, where La2Slp is the geologic estimate. R-factors determined

geodetically agree very well with WG99 estimates. Note that the uncertainty for the R-factor is driven by the fractional uncertainty in the slip rates. For slowly slipping faults like the San Gregorio, the uncertainty in the R-factor is large because the slip rate is low compared to its standard deviation.

Hayward fault (HS and HN)

If the geologic rates are assumed to be correct, Table 2, then the seismogenic layer of the Hayward fault is slipping at nearly the geologic rate giving an R-factor near 0, and implying an absence of strain accumulation. However, a free solution, Table 3, produces nearly the geologic rate for the deep layer, but about 1/3 of that rate for the seismogenic layer, implying R = 1/3.

Calaveras South segment (CS)

The geodetic data prefer a slightly higher than geologic rate. If the deep layer is constrained to geologic values, Table 1, the geodetic model puts the extra slip in the seismogenic layer. In the free solution, Table 3, the deep slip is slightly higher than the geologic rate with most of it occurring aseismically (R = 0.15).

Calaveras Central and North Segments (CC and CN)

The constrained model, Table 2, slip in the seismogenic layer is about equal to the geologic rates, giving R-factors near 0. In the free model, Table 3, the slip pattern is more complex. In the deep layer, the slip rate is more-than-geologic along the central Calaveras and less-than-geologic along the northern Calaveras. In this free case, seismogenic layer slip is significantly less than deep slip giving R-factors of about 2/3.

Rodgers Creek fault (RC)

Along this fault, the geodetic model is mildly unhappy with the geologic rate. If forced to follow the geologic rate in the deep layer, Table 2, the model infers that the seismogenic layer is also slipping at the geologic rate (R = 0). But the geodetic data would prefer to approximately double the geologic rate in the deep layer, Table 3, and then keep slip near zero in the seismogenic layer. Thus producing an R-factor near 1.

Concord and Green Valley faults (CON, GVS and GVN)

Along this fault, the geodetic model is really not happy with the geologic rate. If forced to follow the geologic rate in the deep layer, Table 2, the model infers that the seismogenic layer is also slipping at 3 times the geologic rate (R = -2). But the geodetic data would prefer to quadruple the geologic rate in the deep layer, Table 3, and then keep slip near zero in the seismogenic layer. Thus producing an R-factor near 1. These are the only faults where a non-negative constraint was required to produce right-lateral slip. A pure least-square solution (not shown) produces left-lateral slip at about 8 mm/yr in the seismogenic layer and right lateral slip at rates about 5 mm/yr higher than those in Table 3.

Greenville fault (GS and GN)

Along this fault, the geodetic model prefers slightly more slip than the geologic rate. If the deep slip is constrained to geologic rates, Table 2, the seismogenic slip is 3 times that rate (R = -2). However, a free solution, Table 3, is happy with about double the geologic rate for the deep layer and about the geologic rate in the seismogenic layer. Thus, R = 0.7

Mount Diablo Thrust fault (MTD)

This fault was constrained to zero slip at all depths.

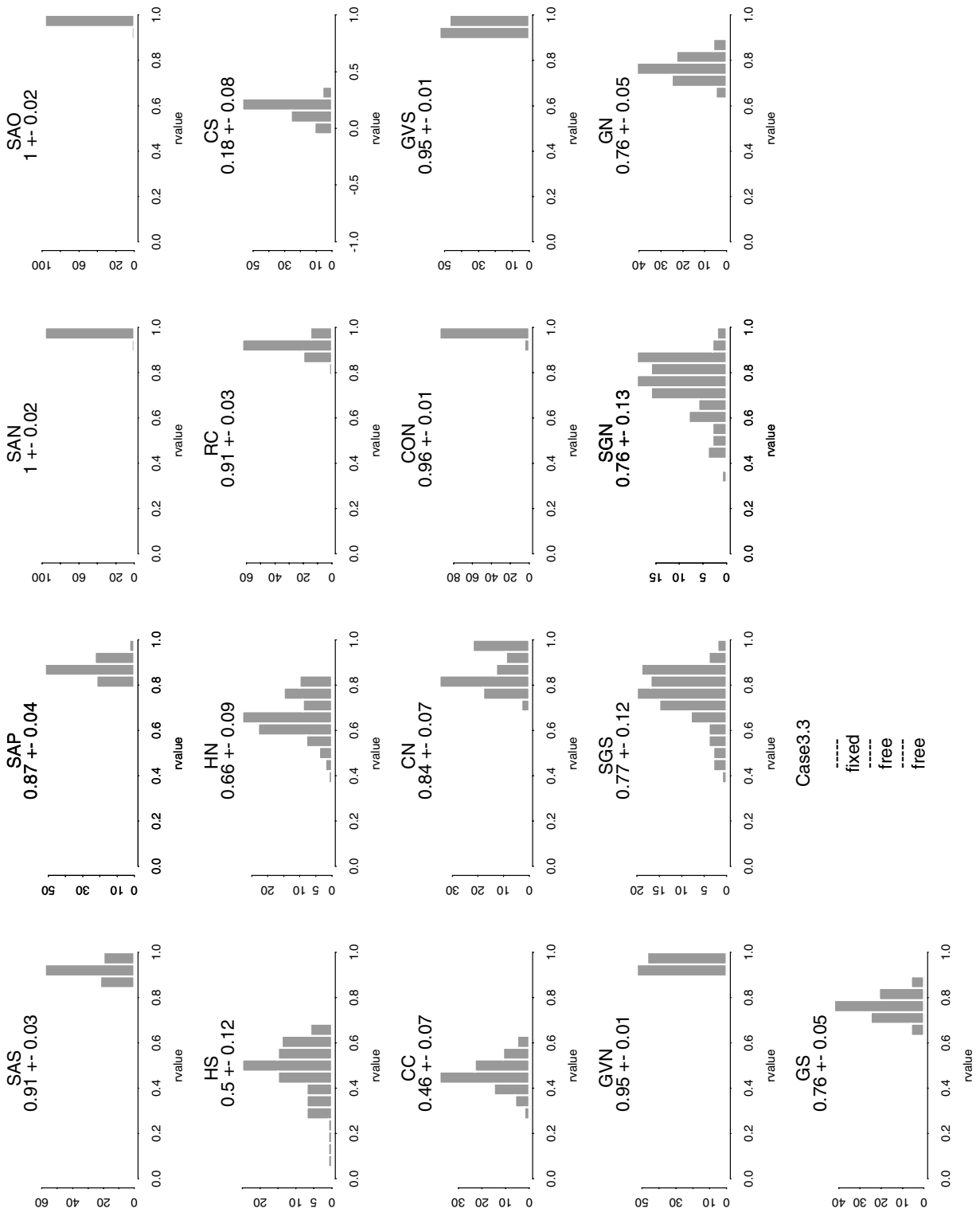

Figure 1. Histograms of R-factors for fault segments. Slip from 0 to 3 km is fixed at the surface creep rate. Slip in the seismogenic layer and in the deep layer are estimated, and R is calculated. Histograms show the values of R obtained for 100 samples of fault end points and depth-to-boundary between seismogenic and deep layer.

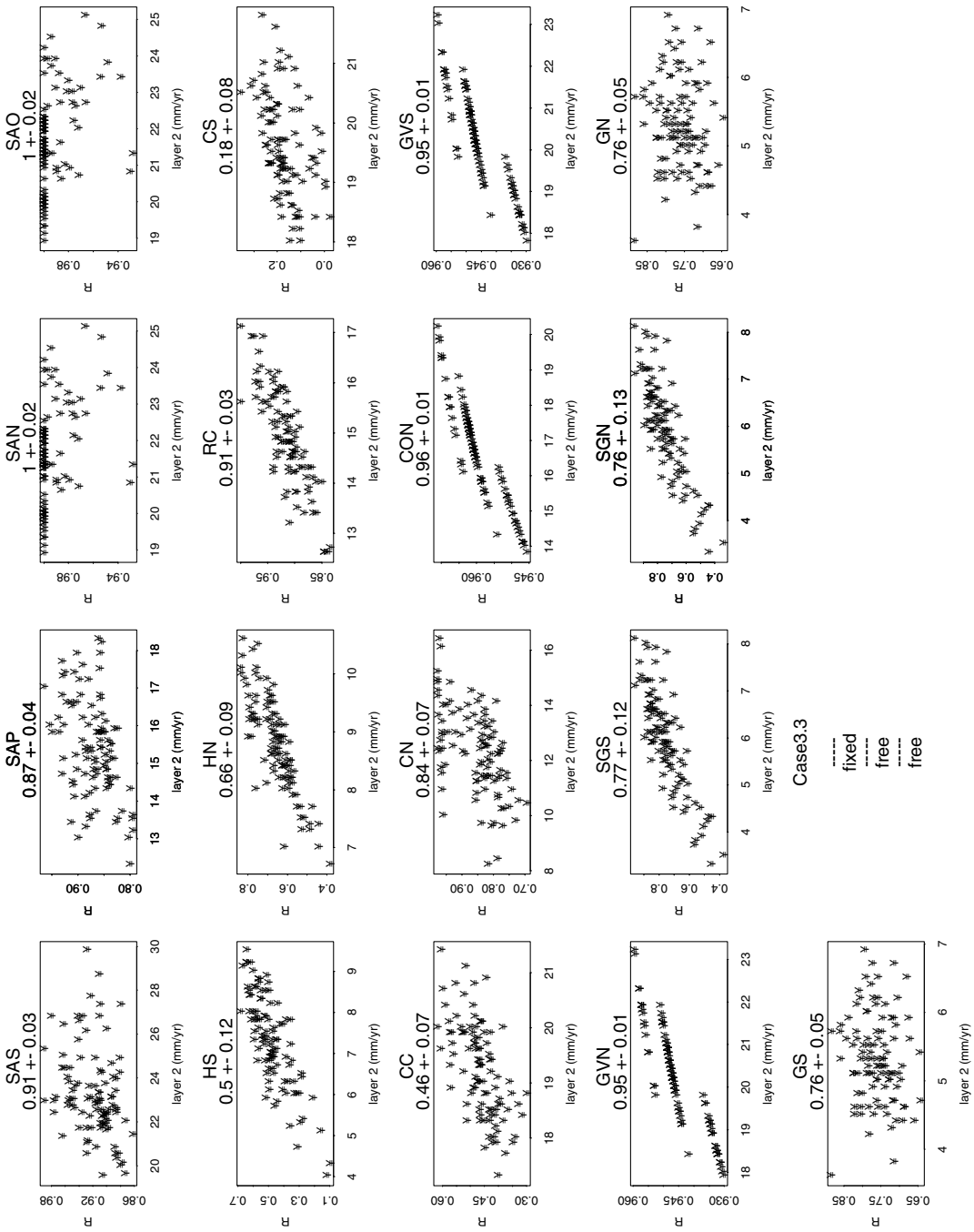

Figure 2. R-factors plotted against Layer 2 fault slip for fault segments. Slip from 0 to 3 km is fixed at the surface creep rate. Slip in the seismogenic layer and in the deep layer are estimated, and R is calculated. Plots show the values of R and slip obtained for 100 samples of fault end points and depth-to-boundary between seismogenic and deep layer.

Appendix D

Magnitude and Area Data for Strike Slip Earthquakes

William L. Ellsworth
U.S. Geological Survey
Menlo Park, CA

This appendix contains a compilation of data sets on the magnitudes and dimensions of large-magnitude strike slip earthquakes. The data sets consists of:

Table D.1. Fifty two earthquakes from Wells and Coppersmith (1994). These events range in **M** from 5.55 to 7.9. They include only those events from Table 1 of Wells and Coppersmith (1994) that those authors considered reliable enough to include in their regression analysis.

Table D.2. Seven California earthquakes for which surface ruptures and/or geodetic models are available in the literature. These events range in **M** from 6.95 to 7.88, and include multiple estimates of **M** and rupture dimensions for 4 of the events.

Table D.3. Eight earthquakes with slip models determined from inversion of seismograms, as interpreted by Sommerville, et al. (1999). In their interpretation of the published slip models, the authors trimmed some area from the slip models. These events range in **M** from 5.66 to 7.22.

Table D.4. Nineteen events compiled from new (and a few unpublished) sources. These events range in **M** from 6.5 to 8.1. The source parameters are determined from available geologic, geodetic and seismological data. Five of the events have more than one estimate of their parameters. Many of the added events are 20th century earthquakes that are listed in Table 1 of Wells and Coppersmith (1994), and that have revised or improved information based on new analyses and data.

The length (L) and width (W) of the ruptures are given in km. Seismic moments are in dyne-cm, with a shear modulus of 3_10^{11} dynes/cm2. All magnitudes are moment magnitudes (**M**). The number of measurements for earthquakes with **M**‡ 7 in the combined data set has increased to 37 from the 11 included in Wells and Coppersmith (1994).

Measurement uncertainty in M and A

Multiple estimates of L, W, A and **M** are available for 16 earthquakes in the combined data set. These redundant measurements can be used to estimate the errors associated with measuring **M** and A. If we consider the difference in magnitude between all possible pairs that measure the same earthquake, an estimated standard deviation (s.d.) of 0.08 magnitude units is obtained for **M**. Similarly, the standard deviation of the ratio of A between pairs of estimates is 1.4 (or 0.15 log-units). Thus, there is significant uncertainty in the data that goes into the correlation analysis.

Regression models of M(A)

Relations between the data in Tables D.1-D.4 are displayed in several different formats in Figures 1-3. These data show a clear dependence of moment magnitude on area (A) (Figure D.1), and of mean slip (U) on **M** (Figure D.2) and on rupture length (Figure D.3). Note in particular that mean slip increases as the fault length grows. This suggests that stress drop should also increase with increasing fault length. Stress drop can be approximately determined from these data using equation 31 of Chinnery (1969). This equation can be used to derive the stress drop at the center of a rectangular dislocation with constant slip that intersects the free surface. These data do indeed show an increase in stress drop with increasing rupture length (Figure D.4).

In principal, the data in Figure D.1 provide all of the information needed to define a **M**(A) relationship. Rather than simply apply the least-squares method, a robust regression method is used that is insensitive to data outliers (Rousseeuw and Leroy, 1987). This is preferable, because we do not have very good control on the errors in the data from the tables. The results of fitting a log-linear regression model to all of the data is

$$\mathbf{M} = 4.17 + 1.015 \log_{10}(A).$$

If we insist on d=1, the best fitting model is

$$\mathbf{M} = 4.16 + \log_{10}(A).$$

If we further restrict the fit to A>500 km^2

$$\mathbf{M} = 4.20 + \log_{10}(A).$$

This fit has an r.m.s. error of 0.19.

Similarly, the best model with d=4/3 for A>500 km^2 is

$$\mathbf{M} = 3.1 + 4/3 \log_{10}(A).$$

This fit has an r.m.s. error of 0.21. The last two equations are essentially identical to equations (2.6b) and (2.8b).

Aleatory variability of M given A

How much variability in **M** occurs when two strike slip faults with identical lengths break, or when the same earthquake happens repeatedly? In other words, how much aleatory variation in **M** is to be expected given that a rupture with area A occurs. This question is difficult to answer from data, as the measurement of both **M** and A are subject to measurement uncertainty.

To approach this question, consider the hypothetical rupture of each of the 38 WG99 rupture sources, producing an earthquake with magnitude given by $\mathbf{M} = 4.2 + \log_{10}(A)$. Further suppose

that when we observe each event that our measurements of A and **M** are uncertain by the same s.d. derived from the comparison of multiple estimates of actual earthquakes discussed above. We can then plot the estimated **M** versus A just as was done in Figure D.1. Figure D.5 shows the result. By construction, the true data that underlie the figure fall on the theoretical (solid) line. The scatter in the points is purely due to measurement error.

Figure D.5 also contains two pairs of lines that correspond to the 90% range for Gaussian variability in **M** about the true A for two different s.d.(**M**). The narrower range (dashed lines) corresponds to s.d.(**M**)=0.12, and the wider range (dotted lines) is for s.d.(**M**)=0.25. Suppose that these two ranges correspond to proposed the intrinsic (aleatory) variation in **M** given A. Clearly, the case with s.d.(**M**)=0.25 is inconsistent with the data, while the narrower range would be difficult to reject.

Now compare Figures D.1 and D.5 (they are plotted on the same axes and scale, and can be overlaid). There are two points to be taken from their obvious similarity. First, simple estimates of measurement uncertainty in A and **M** derived from multiple observations of the same earthquakes produce scatter in the otherwise exact data in Figure 4.5 that roughly mimics the behavior of the actual data in Figure D.1. Second, aleatory variability in **M**(A) of s.d.(**M**)=0.12 magnitude units lies comfortably within the scatter of the data. Given the estimated errors in the measured **M** and A, aleatory variability of 0.12 in **M** is consistent with the actual data in Figure D.1. However, a larger value such as s.d.(**M**)=0.25 would be inconsistent with the data, as the 90% range exceeds the range of the observations in Figure D.1.

References

Aky z, H.S., Barka. A., Altunel, E., Hartleb, R., and Sunal, G., 2000, Field observations and slip distribution of the November 12, 1999 Duzce earthquake (M=7.1), Bolu — Turkey: The 1999 Izmit and D zce Earthquakes: preliminary results, Barka, A., Kozaci, , Aky z, and Altunel, E., eds., Instanbul Technical University, p. 63-70.

Arnadottir, T., Segall, P., and Matthews, M., 1992, Resolving the discrepancy between geodetic and seismic fault models for the 1989 Loma Prieta, California, earthquake: Bulletin of the Seismological Society of America, v. 82, p. 2248-2255.

Barka, A.A., 1996, Slip distribution along the North Anatolian Fault associated with the large earthquakes pf the period 1939 to 1967: Bulletin of the Seismological Society of America, v. 86, p. 1238-1254.

Beanland, S., and Clark, M.M., 1994, The Owens Valley Fault Zone, eastern California, and surface faulting associated with the 1872 earthquake: U.S. Geological Survey Bulletin, Report B, 1982.

Chinnery, M.A., 1969, Theoretical fault models: Dominion Observatory Ottawa Publications, v. 37, p. 211-223.

Delouis, B., Lundgren, P., Salichon, J., and Giardini, D., 2000, Joint inversion of InSAR and teleseismic data for the slip history of the 1999 Izmit (Turkey) earthquake: Geophysical Research Letters, v. 27, p. 3389-3392.

Freymuller, J., King, N.E., and Segall, P., 1994, The co-seismic slip distribution of the Landers earthquake: Bulletin of the Seismological Society of America, v. 84, p. 646-659.

Hudnut, K.W., Bock, Y., Cline, M., Fang, P., Feng, Y., Freymuller, J., Ge, X., Gross, W.K., Jackson, D., Kim, M., King, N.E., Langbein, J., Larsen, S.C., Lisowsik, M., Shen, Z.-K., Svarc, J., and Zhang, J., 1994, Co-seismic displacements of the 1992 Landers earthquake sequence: Bulletin of the Seismological Society of America, v. 84, p. 625-645.

Ji, C., Wald, D.J., and Helmberger, D.V., in press, Source description of the 1999 Hector Mine, California, earthquake: Part II: complexity of the slip history: Bulletin of the Seismological Society of America.

King, N.E., and Thatcher, W., 1998, The coseismic slip distribution of the 1940 and 1979 Imperial Valley, California, earthquakes and their implications: Journal of Geophysical Research, v. 103, p. 18,069-18,086.

Lisowski, M., Prescott, W.H, Savage, J.C., and Johnston, M.J.S., 1990, Geodetic estimate of the coseismic slip during the 1989 Loma Prieta, California, earthquake: Geophysical Research Letters, v. 17, p. 1437-1440.

Molnar. P., and Chen, W.P., 1977, Seismic moments of major earthquakes and the average rate of slip in Central Asia: Journal of Geophysical Research, v. 82, p. 2945-2969.

Peltzer, G., Crampe, F., and King, G.,1999, Evidence of nonlinear elasticity of the crust from the M_W 7.6 Manyi (Tibet) earthquake: Science, v. 286, p. 272-276.

Rousseeuw, P.J., and Leroy, A.M., 1987, Robust Regression and Outlier Detection: John Wiley and Sons, New York.

Sieh, K., 1978, Slip along the San Andreas Fault associated with the great 1857 earthquake: Bulletin of the Seismological Society of America, v. 68, p. 1421-1448.

Sommerville, P., Irikura, K., Graves, R., Sawasa, S., Wald, D., Abrahamson, N., Iwasaki, Y., Kagawa, T., Smith, N., and Kowada, A., 1999, Characterizing crustal earthquake slip models for prediction of strong ground motion: Seismological Research Letters, v. 70, p. 59-80.

Stein, R.S., Barka, A.A., and Dieterich, J.H., 1997, Progressive failure on the North Anatolian fault since 1939 by earthquake stress triggering: Geophysical Journal International, v. 128, p. 594-604.

Stein, R.S., and Hanks, T.C., 1998, M ‡ 6 earthquakes in southern California during the twentieth century: no evidence for a seismicity or moment deficit: Bulletin of the Seismological Society of America, v. 88, p. 635-652.

Thatcher, W., Marshall, G., and Lisowsik, M,1997, Resolution of fault slip along the 7\470-km-long rupture of the great 1906 earthquake and its implications: Journal of Geophysical Research, v. 102, p. 5353-5367.

Wells, D.L., and Coppersmith, K.J., 1994, New empirical relationships among magnitude, rupture length, rupture width, rupture area, and surface displacement: Bulletin of the Seismological Society of America, v. 84, p. 974-1002.

Wright, T., Parsons, B., and Fielding, E., 2001, Triggered slip, observations of 17 August 1999 Izmit (Turkey) earthquake using radar interferometry: Geophysical Research Letters, v. 28, p. 1079-1082.

Yagi, Y., 2001, http://www.eic.eri.u-tokyo.ac.jp/yuji/English.html.

Yagi, Y., and Kikuchi, M., 2000, Source rupture process of the Kocaeli, Turkey, earthquake of August 17, 1999, obtained by joint inversion of near-field and teleseismic data: Geophysical Research Letters, v. 27, p. 1969-1972.

Yu, E., and Segall, P., 1996, Slip in the 1868 Hayward earthquake from the analysis of historical triangulation data: Journal of Geophysical Research, v. 101, p. 16,101-16,118.

Table D.1. Wells and Coppersmith (1994) Strike Slip Earthquakes

Earthquake	W&C #	M	Moment	Length	Width
1906 San Francisco	7	7.9	7.90E+27	432	12
1932 Long Beach	21	6.38	4.10E+25	23	13
1940 Imperial V.	26	6.92	2.70E+26	45	11
1958 Lituya Bay	53	7.77	5.10E+27	350	12
1963 Wakasa Bay	57	6.28	3.00E+25	20	8
1963 Skopje	58	5.99	1.10E+25	17	11
1966 Parkfield	63	6.25	2.70E+25	35	10
1966 Truckee	66	5.96	9.70E+24	13	7
1968 Borrego Mtn.	71	6.63	1.00E+26	40	10
1968 Dasht-e-Bayaz	73	7.23	7.80E+26	110	20
1968 Rampart	75	6.69	1.20E+26	30	8
1969 Coyote Mtn.	77	5.69	3.80E+24	10	3
1969 Gifu	80	6.34	3.60E+25	18	10
1969 Ceres	81	6.37	4.00E+25	20	9
1972 Sitka	91	7.7	4.00E+27	180	10
1973 Luho	96	7.47	1.80E+27	110	13
1974 Izu-Oki	100	6.54	7.20E+25	18	11
1975 Haicheng	104	6.99	3.45E+26	60	15
1975 Oita	106	6.32	3.40E+25	10	10
1976 Guatamala	112	7.63	3.10E+27	257	13
1976 Tangshan	116	7.46	1.76E+27	70	24
1976 Songpan #1	117	6.71	1.30E+26	30	12
1976 Songpan #3	120	6.58	8.40E+25	22	11
1976 Mexico	122	5.61	2.90E+24	9	5
1977 Bob-Tangol	128	5.89	7.60E+24	14	12
1978 Izu-Oshima	129	6.71	1.32E+26	50	10
1979 Homesead V	138	5.55	2.41E+24	6	4
1979 Coyote L.	141	5.77	5.10E+24	14	10
1979 Imperial V.	144	6.53	7.12E+25	51	12
1980 Mammoth L. #4	151	5.99	1.09E+25	9	11
1980 Mexicali	152	6.4	4.50E+25	28	8
1980 Izu-Hanto-Toho	153	6.39	4.30E+25	14	10
1981 Daofu	158	6.64	1.01E+26	46	15
1983 Pasinier	175	6.73	1.40E+26	50	16
1983 Guinea	177	6.32	3.40E+25	27	14
1984 Morgan Hill	178	6.28	3.00E+25	26	8
1974 Naganoken-Seibu	183	6.24	2.60E+25	12	8
1984 Round V.	185	5.83	6.20E+24	7	7
1985 New Britan	187	7.19	6.93E+26	50	15
1985 Algeria	192	6	1.11E+25	21	13
1986 Mt. Lewis	198	5.64	3.20E+24	5.5	4
1986 N. Palm Sp.	201	6.13	1.73E+25	16	9
1986 Chalfant V.	203	6.31	3.20E+25	20	11
1987 Elmore Ranch	215	6.2	2.60E+25	30	12
1987 Superstition H.	216	6.61	9.20E+25	30	11
1988 Lancang-Gengma	221	7.13	5.47E+26	80	20
1989 Loma Prieta	227	6.92	2.67E+27	40	16
1990 Izu-Oshima	230	6.37	4.05E+25	19	12
1990 Luzon	233	7.74	4.60E+27	120	20
1992 Joshua Tree	239	6.27	2.90E+25	15	13
1992 Landers	240	7.34	1.14E+27	62	12
1992 Big Bear	241	6.68	1.16E+26	20	10

Table D.2. California Earthquake Ruptures with Geologic and Geodetic Data

Earthquake	M	Length	Width	Source
1857 Ft. Tejon	7.83	300	13	Sieh (1978)
1868 Hayward	6.95	52	10	Yu and Segall (1996)
1868 Hayward	7.05	52	15	Yu and Segall (1996)
1872 Owens V.	7.6	110	15	Beanland and Clark (1994)
1872 Owens V.	7.46	110	12.5	Stein and Hanks (1998)
1906 San Francisco	7.88	470	10	Thatcher et al. (1997)
1940 Imperial V.	6.97	65	9	King and Thatcher (1998)
1989 Loma Prieta	6.95	37	13	Lisowski et al. (1990)
1989 Loma Prieta	6.95	36	10	Arnadottir et al. (1992)
1992 Landers	7.31	65	10	Hudnut et al. (1994)
1992 Landers	7.27	65	10	Freymueller et al. (1994)

Table D.3. Strike Slip Earthquake Rupture Models from Sommerville, et al. (1999)

Earthquake	Length	Width	M
1979 Coyote Lake	5.5	4.57	5.66
1979 Imperial Valley	36	10	6.43
1984 Morgan Hill	26	11.5	6.18
1986 North Palm Springs	20	13.3	6.14
1987 Superstition Hills	20	8.05	6.33
1989 Loma Prieta	40	18	6.95
1992 Landers	69	15	7.22
1995 Kobe	60	20	6.9

Table D.4. Earthquakes added from literature or unpublished studies

Earthquake	M	Moment	Length	Width	Source
1905 Bunlay, Mongolia	7.97	1.00E+28	300	15	Schwartz, written comm. (2001)
1905 Bunlay, Mongolia	8.1	1.70E+28	350	20	Schwartz, written comm. (2001)
1939 Erzihcan, Turkey	7.9	5.20E+27	327	12.5	Barka (1996); Stein et al. (1997)
1942 Erbaa, Turkey	6.9	1.70E+26	40	12.5	Barka (1996); Stein et al. (1997)
1943 Kastamonu, Turkey	7.7	2.90E+27	275	12.5	Barka (1996); Stein et al. (1997)
1944 Bolu, Turkey	7.5	1.50E+27	162	12.5	Barka (1996); Stein et al. (1997)
1949 Elmalidere, Turkey	7.1	3.50E+26	63	12.5	Barka (1996); Stein et al. (1997)
1951 Turkey	6.8	1.40E+26	35	16.25	Barka (1996); Stein et al. (1997)
1957 Abant, Turkey	6.8	1.40E+26	27	12.5	Barka (1996); Stein et al. (1997)
1957 Gobi Altai, Mongolia	7.71	4.20E+27	260	15	Schwartz, written comm. (2001)
1957 Gobi Altai, Mongolia	8.04	1.30E+28	260	20	Molnar and Chen (1977)
1966 Varto, Turkey	6.6	6.00E+25	41	12.5	Barka (1996); Stein et al. (1997)
1967 Mudurna V., Turkey	7	2.70E+26	75	12.5	Barka (1996); Stein et al. (1997)
1971 Bingol, Turkey	6.8	1.20E+26	51	12.5	Barka (1996); Stein et al. (1997)
1992 Erzincan, Turkey	6.5	4.00E+25	20	12.5	Barka (1996); Stein et al. (1997)
1996 Manyi, Tibet	7.6	2.80E+27	170	8	Peltzer et al. (1999)
1999 Izmit, Turkey	7.4	2.60E+27	136	12.5	Wright et al. (2001)
1999 Izmit, Turkey	7.58	2.60E+27	150	17	Delouis et al. (2000)
1999 Izmit, Turkey	7.4	1.40E+27	70	15	Yagi and Kikuchi (2000)
1999 Hector Mine	7.1	5.00E+26	54	13	Ji, et al., (in press)
1999 Hector Mine	7.1	6.10E+26	42	18	Yagi (2001)
1999 Duzce, Turkey	7.1	4.50E+26	40	12.5	Akyuz et al. (2000)
1999 Duzce, Turkey	7.1	5.60E+26	30	20	Yagi (2001)
2000 Tottori, Japan	6.6	1.10E+26	22	12	Yagi (2001)
2000 New Ireland, P.N.G.	8	1.30E+28	210	40	Yagi (2001)

Figure Captions

Figure D.1. Rupture area (A) in km^2 versus moment magnitude (**M**).

Figure D.2 Moment magnitude versus mean slip (U) in cm. Mean slip determined from definition of seismic moment using reported **M**, A, and shear modulus of 3_10^{11} dynes/cm^2.

Figure D.3. Rupture length (L) in km versus mean slip (U) in cm.

Figure D.4. Rupture length in km versus stress drop. Stress drop defined at the center of a rectangular dislocation with constant slip that intersects the free surface.

Figure D.5. Effect of random measurement (epistemic) errors in A and **M** on a hypothetically observed rupture of each WG99 rupture source. The correct value of $\log_{10}(A)$ for each rupture source has been corrupted by the addition of Gaussian noise with a s.d. of 0.15. Similarly, the correct values of M determined using equation (2.6b) were corrupted with Gaussian noise with a s.d. of 0.08. If measurements were error free, they would all fall on the solid line. The dashed and dotted lines correspond to 90% range of a hypothetical aleatory variability of **M** equal to 0.12 and 0.25, respectively.

Figure D.1

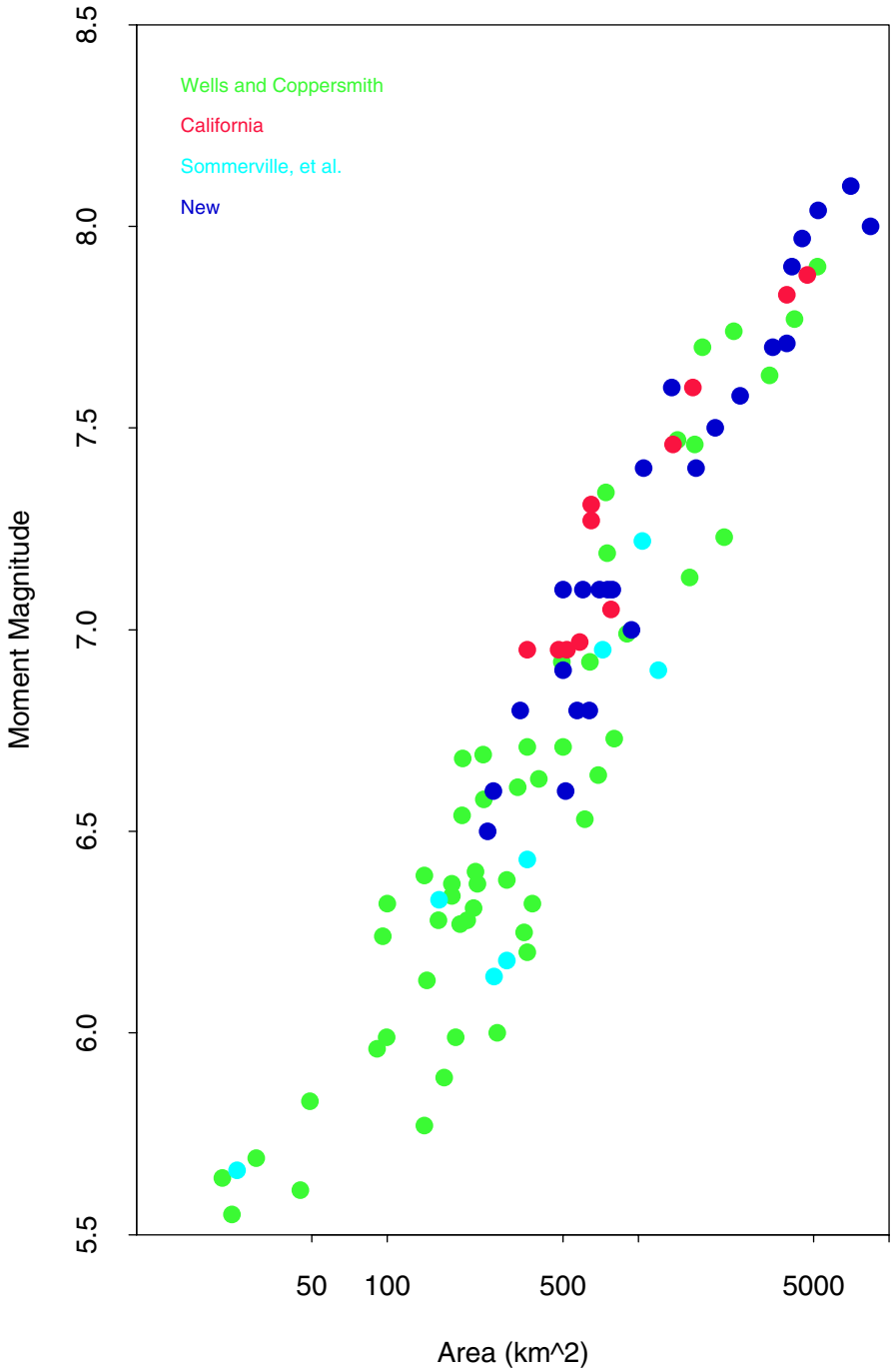

Figure D.2

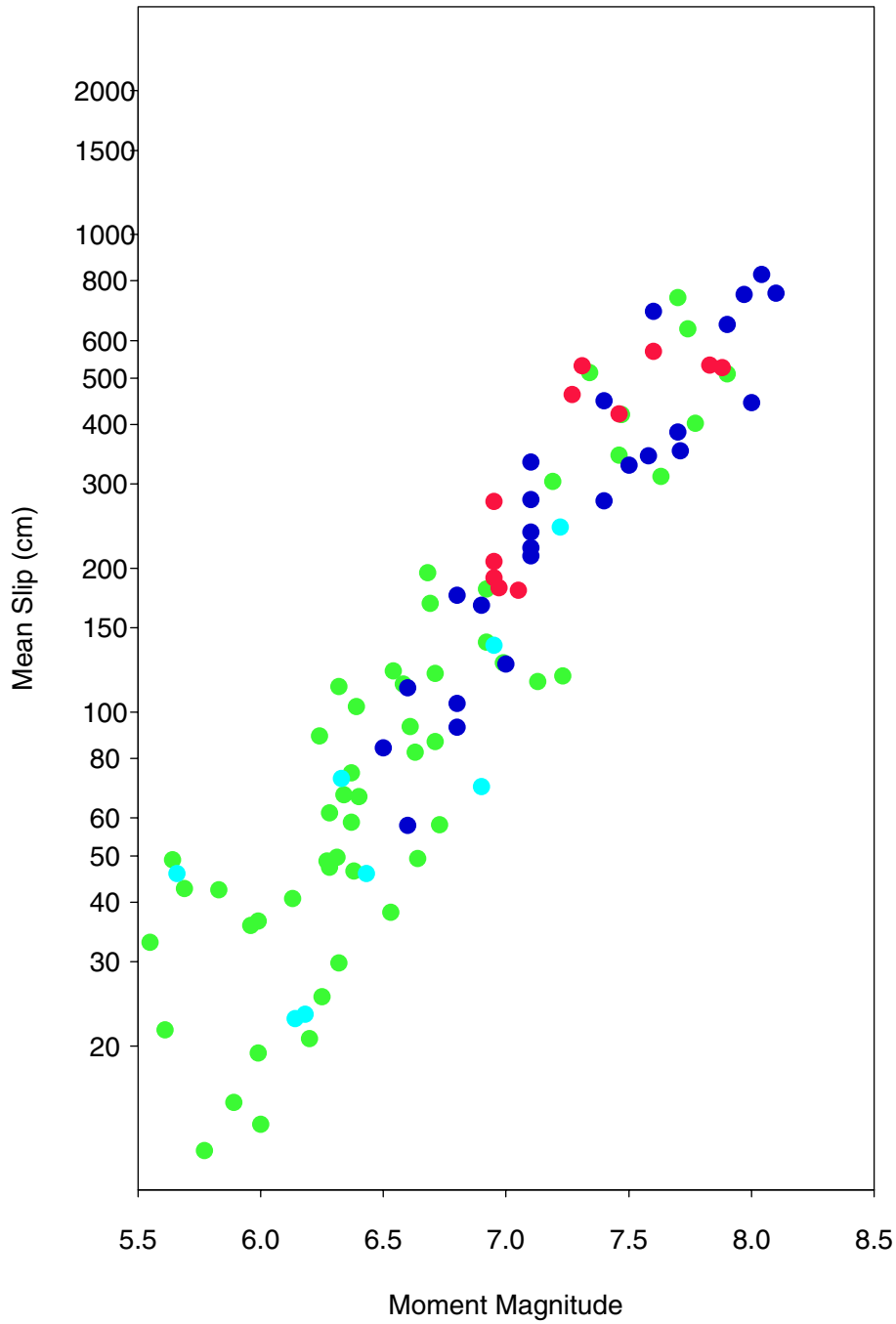

Figure D.3

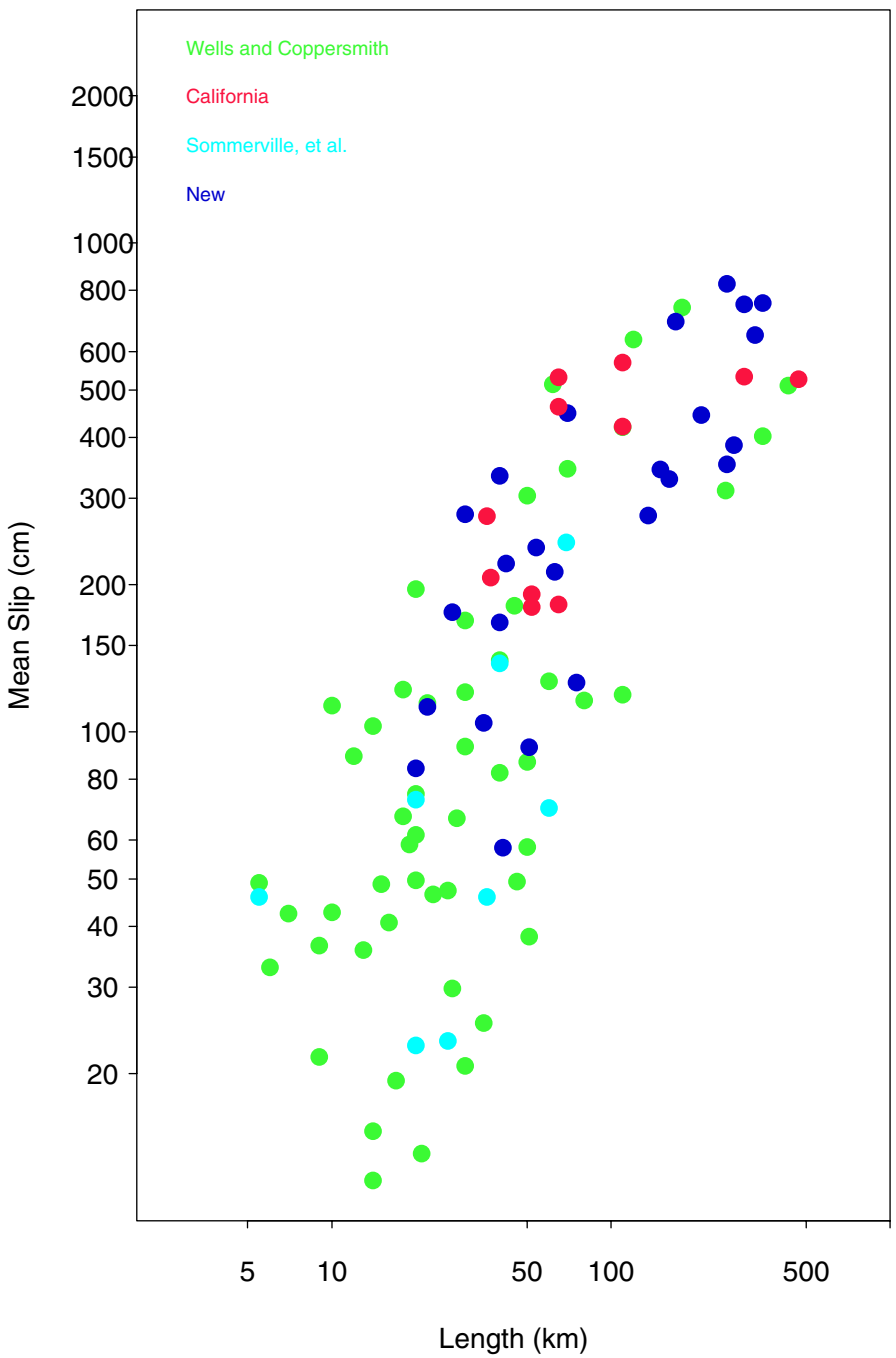

Figure D.4

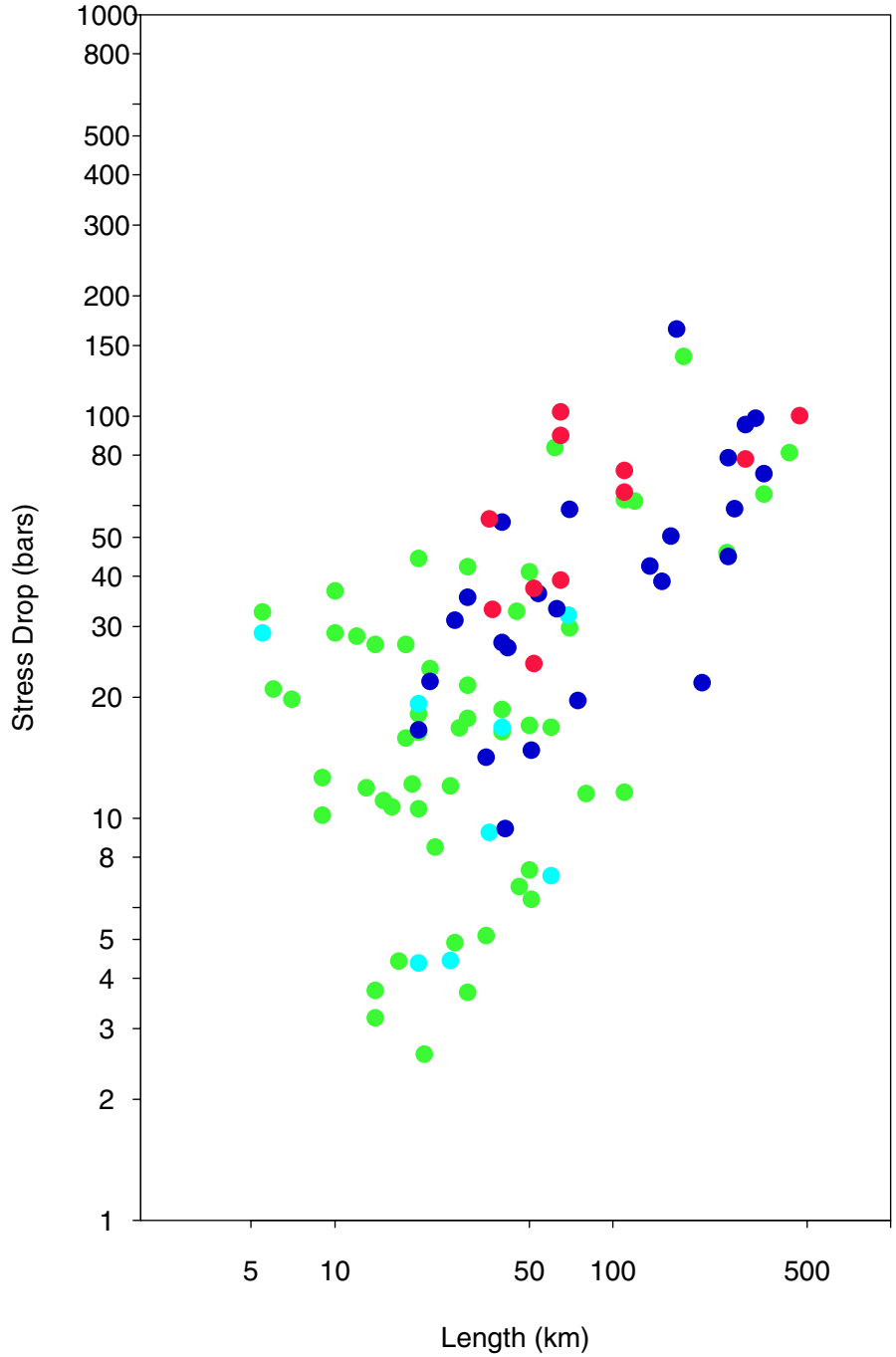

Figure D.5

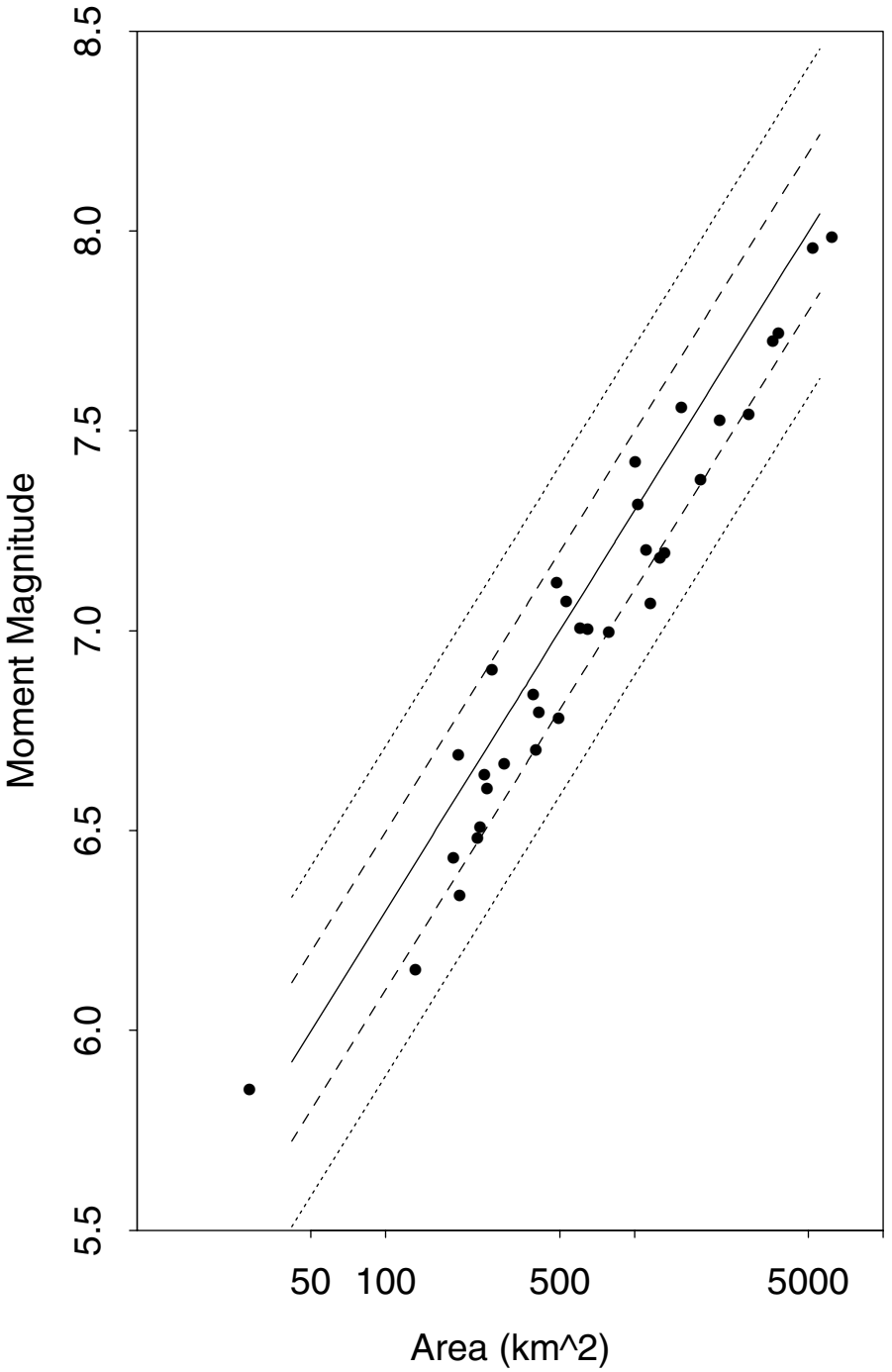

Appendix E

Moment Released by Aftershocks

Paul A. Reasenberg

Part 1: Moment released by aftershocks in the WG99 model

In constructing moment-balanced fault rupture models for the SF Bay region, WG99 needed to account for all the moment released by earthquakes in the region. These include earthquakes on characterized rupture sources, earthquakes on other rupture sources (background), and their aftershocks. Some of the aftershocks will be large, with magnitudes sometimes exceeding 6.7. WG99 assumed that an aftershock of this size would likely break the surface and have a rupture area comparable to one of the characterized fault segments, a fault segment in the background, or one of the floating earthquake sources. These aftershocks probably cannot occur on the same segments that broke in the main shock because they release too much moment. An aftershock of this size is often referred to as a *triggered earthquake*.

WG99 considered triggered earthquakes to be among the events included among the characterized rupture sources on the faults or in the background. Furthermore, it was felt that both the first earthquake and the triggered one usually would be included in any future assessment of the model s probability estimate. For example, if a M=7.5 earthquake on the Hayward fault were followed weeks, months or even a few years later, by a M=7.0 earthquake on the Rodgers Creek fault, or in the background, or on another characterized fault, WG99 would consider both earthquakes to be the output of the average regional model, despite their temporal relationship. Another example (if a WG99-like approach were applied to southern California) would be the 1992 M=7.2 Landers earthquake and the 1999 M=7.0 Hector Mine earthquake.

The smaller magnitude aftershocks tend to occur on or very near the fault segments that ruptured in the main shock. These events may fill in patches of low slip within and around the rupture, or smooth the high stress concentrations created around it by the main shock. These aftershocks help to complete the moment release on the ruptured segments. Here, we estimate the fraction of regional moment that is released in the WG99 model through M<6.7 aftershocks with the use of a generic model (Reasenberg and Jones, 1990, 1994). The model parameters are estimated using only northern California aftershock sequences. See Part 2 for a description of this model. We apply the model to each fault, using the largest WG99-characterized rupture on the fault as the model s main shock. From such models for all the faults and background, we calculate the total long-term moment rate associated with the M<6.7 aftershocks, and express this quantity as a fraction of the total regional moment rate. We find that over the long term the moment released by M<6.7 aftershocks in the region amounts to 3%–2% of the total moment released in the region. Those who go on to read Part 2 in its entirety will find that a

generic northern California sequence contains approximately 10% of its moment in aftershocks. However, applying this model to all the faults and keeping only the M<6.7 aftershocks leads to the 3% result.

Part 2: Moment released by aftershocks in a generic northern California earthquake sequence

The moment in an aftershock sequence can be expressed as a function of the magnitude of the mainshock and the a-value and b-value of the aftershock magnitude distribution. I calculate the moment sum for aftershocks in a generic aftershock sequence (as determined empirically for northern California), and express this as a fraction of the total moment for the sequence. Because the generic aftershock model is self-similar, f is independent of the main shock magnitude, M_m, and depends only on the model parameters.

Definitions:

M_m	Magnitude of main shock.
W_m	Moment of main shock
$W(M)$	Moment of an aftershock of magnitude M.
a, b	Parameters of the cumulative form of the G-R relation
a', b	Parameters of the interval form of the G-R relation
a^*	Parameter in the R&J (1989, 1994) formulation
f	Fraction of moment in earthquake sequence released in aftershocks

All logs are base 10 and R&J stands for Reasenberg and Jones (1989, 1994)

The magnitude distribution of the aftershocks follows the Gutenberg-Richter relation

$$\log N(m \geq M) = a - bM \tag{1}$$

In the incremental form of the G-R relation, the number of earthquakes $dN(M)$ within a magnitude increment ΔM centered on M is

$$\log dN(M) = \log N\left(M - \frac{\Delta M}{2} \leq m < M + \frac{\Delta M}{2} \right) = a' - bM \tag{2}$$

We will work with the incremental form, calculate the moment in each magnitude interval, and sum these to get the total moment in the aftershock sequence.

The moment, $W(M)$, of an earthquake is related to its magnitude, M, by

$$\log W(M) = 1.5M + 16.05$$

(Hanks and Kanamori, 1979). The summed moment, $dW(M)$, associated with the events in the magnitude interval centered on M is equal to the number of such events, $dN(M)$ times the mean moment in the interval, $W(M)$. Thus

$$\begin{aligned} \log dW(M) &= \log dN(M) + \log W(M) \\ &= a' + (1.5 - b)M + 16.05 \end{aligned} \tag{3}$$

The relationship between a' and a depends on ΔM and b and is obtained by starting with Andrews and Schwerer, equation (7) (Andrews and Schwerer, 2001):

$$\frac{dN}{dM} = 2.3b \exp[2.3(a - bM)]$$

Then, switching from differentials to finite intervals (Joe Andrews, personal communication),

$$\begin{aligned} \frac{\Delta N}{\Delta M} &= 2.3b \exp[2.3(a - bM)] \\ \Delta N &= 2.3b\Delta M \exp[2.3(a - bM)] \\ &= 2.3b\Delta M 10^{a - bM} \\ \log(\Delta N) &= \log(2.3b\Delta M) + a - bM \end{aligned}$$

so

$$a' = \log(2.3b\Delta M) + a. \tag{4}$$

Plugging this result into (3),

$$\log dW(M) = a + \log(2.3b\Delta M) + (1.5 - b)M + 16.05 \tag{5}$$

Next, we need to relate a to the generic aftershock sequence model. R&J (1994) express the rate of aftershocks with magnitude M or larger at time t after a main shock of magnitude M_m as

$$\lambda(t, M) = 10^{a^* + b(M_m - M)}(t + c)^{-p} \tag{6}$$

where c and p are the Omori constants, and a^* is not to be confused with a *or* a'. The corresponding cumulative number of aftershocks (up to time T) with magnitude M or larger is

$$N(m \geq M) = \int_0^T \lambda(t, M)dt$$
$$= 10^{a^* + b(M_m - M)} \int_0^T \frac{dt}{(t+c)^p} \tag{7}$$

where

$$\int_0^T \frac{dt}{(t+c)^{-p}} = \frac{(T+c)^{(1-p)} - c^{(1-p)}}{1-p} \equiv I \qquad (p > 1)$$

Equation (7) is in the form of the G-R relation, with

$$a = \log(I) + a^* + bM_m \tag{8}$$

Finally, combining the expressions for the number and moment distribution of aftershocks (equations 2 and 5) with the expressions for a' (equation 4) and the generic aftershock sequence (equations 7 and 8), we have

$$\log dN(M) = a^* + b(M_m - M) + \log(2.3b\Delta M) + \log(I)$$
$$\log dW(M) = a^* + bM_m + (1.5 - b)M + \log(2.3b\Delta M) + \log(I) + 16.05 \tag{9}$$

Model parameters for northern California

At this point, we have expressed the distribution of aftershock magnitude and moment in terms of the parameters in the R&J generic aftershock model (a^*, b, p , c) and the magnitude of the mainshock. For 62 sequences in California, R&J found median values a^*= -1.67, b=0.91, p=1.08 and c=0.05. In an unpublished continuation of their 1989 study, R&J estimated mean values of these parameters separately for southern California, northern California and eastern California. While subdividing the data resulted in smaller numbers of sequences in each set, some regional parameter estimates were significantly different from the all-California estimates. A significant difference was found in a^*, which for the 16 northern California sequences averaged a^*=—2.0. They found for Morgan Hill, a* = -3.2; for Coyote Lake, a* = -2.0; and for the Loma Prieta sequence, a^* = -1.7. We adopt the value of a^* estimated by R&J for northern California (a^* = -2.0). For the other parameters, we use the generic California values, since no significant regional differences for these were found by R&J. The curves in Figure 1 depict Equation (9) for these parameters.

Example for a M=7 main shock

Figure 1a shows the cumulative and interval forms of the magnitude (frequency) distribution for aftershocks following a $M_m = 7$ main shock. The numbers and moment are cumulative for the first 1000 days of the sequence. The main shock is represented by the black dot. The a-value is 5.3, $a' = 4.6$. Approximately 1 aftershock of magnitude 5.8

or larger is expected. Figure 1b shows the corresponding cumulative and interval distributions of moment. The moment in the M=7 main shock is $3.55 \bullet 10^{26}$ dyne-cm. The summed moment of aftershocks (in this example, in the magnitude range 3.0 † M † 6.9), expressed as a fraction, *f,* of the total moment (aftershocks + main shock) is $f = 0.10$. In the ranges 3.0†M†3.9, 4.0†M†4.9, 5.0†M†5.9, and 6.0†M†6.9, f equals 0.001, 0.005, 0.019 and 0.074, respectively.

References

Andrews, D.J. and E. Schwerer, Probability of rupture of multiple fault segments, Bull. Seismo. Soc. Am., 90, 1498-1506, (2000)

Hanks, T.C. and H. Kanamori, A moment magnitude scale, J. Geophys. Res. 84, 2348-2350 (1979).

Reasenberg, P.A. and L.M. Jones, Earthquake hazard after a mainshock in California, Science, 243, 1173-1176 (1989).

Reasenberg, P.A. and L.M. Jones, Earthquake aftershocks: update, Science, 265, 1251-1252 (1994).

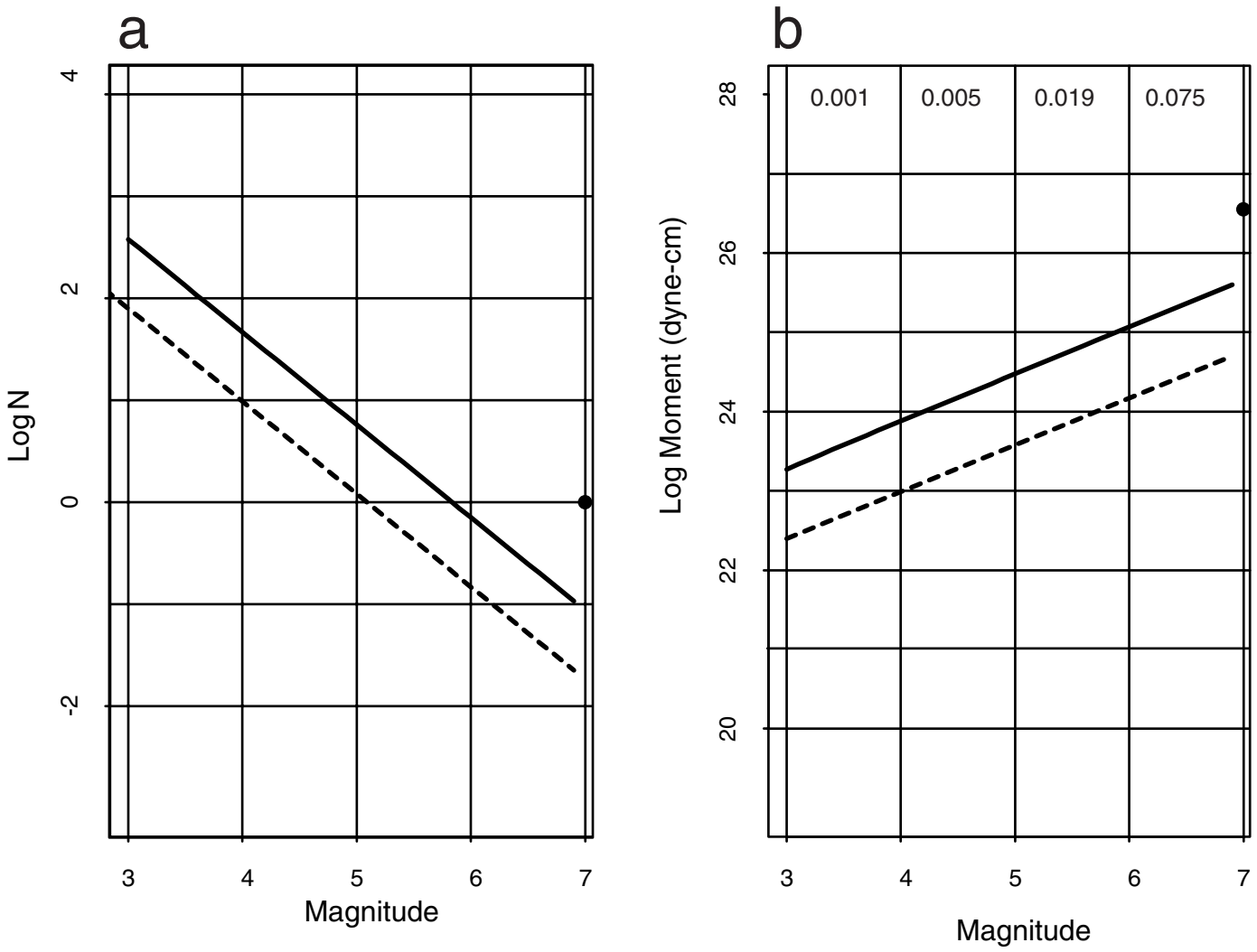

Plots of Equation (9) for an aftershock sequence following a M=7 main shock, using model parameters (a*=-2.0, p=1.08, b=0.91, c=0.05). These parameters are representative of aftershock sequences observed in northern California. (a) Magnitude distribution of aftershocks. Solid dot represents the main shock (N=1). Solid line is the cumulative distribution; dashed line is the interval distribution, for magnitude interval width 0.1. (b) Distribution of moment. Solid dot is the moment of the main shock. Cumulative distribution of aftershock moment (solid line) is obtained by summing the interval distribution (dashed line). 10% of the total moment in this model sequence (main shock plus aftershocks) is released in 3.0≤M≤6.9 aftershocks. Numbers at top are the fraction, f, of moment in the magnitude ranges 3.0≤M≤3.9, 4.0≤M≤4.9, 5.0≤M≤5.9, and 6.0≤M≤6.9.

Appendix E - Figure 1

Appendix F

Estimated Changes in State on San Francisco Bay Region Faults Resulting from the 1906 and 1989 Earthquakes

Robert W. Simpson

Introduction

In the 70 years prior to the great 1906 San Francisco earthquake, seventeen **M**≥6 earthquakes shook the San Francisco Bay region; in the 94 years following there have been only five (Bakun, 1999). A plausible explanation is that after great earthquakes the crust in an entire region is relaxed, creating a "stress shadow" within which other large earthquakes are suppressed until plate tectonic stresses gradually reload the faults (Ellsworth and others, 1981; Harris and Simpson, 1998). Calculations indicate that every major fault system in the Bay region was relaxed to some degree by the 1906 event (Figure 1).

In this report, calculated changes in stress are *static* changes, which are the changes that persist after the passage of the seismic waves with their attendant *dynamic* stress changes. Dynamic stress changes are often considerably larger than static changes, although dynamic changes may have the greatest effect on faults that were already close to failure, whereas static changes would have a greater long-term role in advancing or delaying future earthquakes on faults not yet near the end of their loading cycle (e.g., Kilb and others, 2000).

Calculations of stress changes were made by assuming elastic halfspace behavior and using rectangular dislocations to represent slipping fault segments (Okada, 1992). Although the elastic assumption probably does a fair job of estimating coseismic stress changes immediately after an earthquake, it cannot adequately describe post-seismic relaxation caused by viscous flow in the lower crust and mantle (e.g., Pollitz and others, 1998; Kenner and Segall, 1999) and it offers a limited number of ways to simulate tectonic loading on faults, which may result in estimated loading rates that are too large (Parsons, 2001). At the time WG99 began, it seemed safest to use the simple elastic halfspace approach in spite of its shortcomings, because more complex models did not seem fully mature and required additional assumptions about rheology and geometry.

The conceptual approach to failure used in this report is based on the Coulomb failure criterion: a stress relaxation shadow delays future earthquakes on a fault at least until the state of stress on the fault recovers to its pre-1906 level (Figure 2), at which time the possibility of an earthquake occurring once again exists. Laboratory derived rate-and-state failure laws suggest that changes in the timing of failure are not this simple—especially if the fault was close to failure just before it was relaxed (e.g., Dieterich, 1994; Stein and others, 1998; Gomberg and others, 1998; Harris and Simpson, 1998; Toda and others, 1998). Rate-and-state approaches to the estimation of earthquake-induced probability changes are being actively researched and tested (e.g., Dieterich and others, 2000; Gomberg and others, 2000; Parsons and others, 2000; Toda and Stein, 2001), but for the purposes of this report, the simple Coulomb failure approach was deemed most appropriate, pending further validation of the newer methods.

The Coulomb failure approach used here assumes a fixed failure threshold to estimate a *clock change* in years (Figure 2). Calculation of a clock change requires information about (1) the

coseismic Coulomb stress change on the fault and (2) the long-term loading rate of the fault caused by plate tectonic displacements. The clock change equals the coseismic stress change (in bars) divided by the loading rate (in bars/yr), and can be either a delay in the case of relaxation or an advance if Coulomb failure stress has been increased. This clock change can then be used to adjust probability estimates.

Two adjustment approaches were tried in conjunction with the Brownian Passage Time (BPT) probability distribution: Originally the estimated clock change was used to shift the reset time of the last event on a segment forward or backward by that number of years depending on whether the change was relaxing or more stressing. But the BPT distribution is based on a physical concept of a state evolving in time toward a failure threshhold, and this affords a natural way to perturb the system by stepping the state closer to or farther from the failure threshhold. Although the original approach of shifting reset times was easy to implement, it offers a good approximation to the BPT state-step result only if the time elapsed since the last event is small compared with the recurrence interval for the segment. Unfortunately, this condition was not met by many segments. We ultimately implemented the BPT state-step approach in order to overcome this limitation. Step size was estimated from the clock change and the recurrence interval. (See other appendices describing the BPT distribution for details.)

The question of immediate concern is whether the period of post-1906 quiescence can be expected to continue in the Bay region, or whether it has ended for at least some faults. Simple models described here indicate that most faults in the Bay region, with perhaps the exception of the northern San Gregorio fault, have recovered from the relaxation and passed the level of stressing that obtained for them just before the 1906 event. In spite of the uncertainties in these models and the difficulties in confirming and calibrating their results, it would seem prudent to act on the assumption that the extraordinary period of seismic quiet experienced in the Bay area after 1906 is ended or close to ending.

Coulomb Stress Change

The Coulomb stress change at a point on a fault surface is calculated using the Coulomb failure criterion (Jaeger and Cook, 1979; Scholz, 1990), which says that a fault will fail when the shear and normal stresses on the surface satisfy:

$$\sigma_C \equiv \tau - \mu(\sigma_n - p) \geq C \qquad (1)$$

where τ is the magnitude of the shear stress acting on the fault plane, μ is the coefficient of friction, σ_n is the normal stress acting on the fault plane (positive in compression), p is the pore fluid pressure, and C is the cohesion. The quantity on the left of the inequality is called the Coulomb stress σ_C (also referred to as the Coulomb failure function or CFF). Assuming that the cohesion C does not change, then a stress change induced by a nearby earthquake or other source can move the fault closer to or farther from failure depending on whether the sign of the change in Coulomb stress is positive or negative:

$$\Delta\sigma_C = \Delta\tau_r - \mu(\Delta\sigma_n - \Delta p) \qquad (2)$$

where $\Delta\tau_r$ indicates the shear stress change in the rake (slip) direction of the fault, which implies that the important shear stresses are those that act in the usual slip direction of the fault.

Changes in pore fluid pressure in response to changes in the local stress tensor depend on the poroelastic behavior of the fault zone and surrounding materials. If there are permeable pathways for the fluid to migrate Δp will also evolve with time as the fluid re-equilibrates to the new stress regime (Jaumé and Sykes, 1992). Two fluid behavior models that are commonly used assume either (1) that the instantaneous changes in pore pressure follow isotropic homogeneous poroelastic behavior or (2) respond in linear fashion to the normal stress changes (Roeloffs, 1996; Beeler and others, 2000). Little is know about the evolution in time of pore fluid pressures, although it has been suggested that it might be a combination of such behaviors (Rice and Cocco, 2000). It seems fair to say that existing models of pore fluid behavior, based as they are on very limited observations, probably fall far short of describing the real complexity that exists in the earth.

Estimating 1906 Coseismic Coulomb Stress Changes

Coseismic static stress changes on Bay region faults were estimated for the great 1906 San Francisco earthquake and for the 1989 Loma Prieta earthquake. Many examples of such calculations, designed to investigate stress triggering of earthquakes and the locations of aftershocks after a large mainshock, have been reviewed by Harris (1998). For the models described here, the stress changes were obtained using the elastic-halfspace dislocation equations of Okada (1992). These equations apply to rectangular dislocation patches, which can be arranged end-to-end to represent an earthquake rupture.

Because little is presently known about the appropriate values for coefficient of friction and other parameters, and because of uncertainties in the endpoints and heights of the WG99 segments, a Monte Carlo approach was adopted to explore a range of weighted possibilities. Estimation of the change in Coulomb failure stress on a fault requires a value for the coefficient of friction, which determines the relative contribution of fault-normal stress changes to failure, and an assumption as to how pore fluid behavior modulates the stress changes. Choices and weights used here for these parameters are given in the first 3 rows of Table 1.

The 1906 rupture model of Thatcher and others (1997) used an array of 10-km tall by 10-km long rectangular patches to represent the 480-km long earthquake fault plane (Figure 1). Their model was based on an analysis of geodetic observations before and after the event and offers uncertainties that define the range of probable slip values consistent with the observations. These uncertainties were used to define "minimum" and "maximum" slip distributions for the 1906 event ("Slip Distribution" parameter in Table 1). The depth of rupture was poorly resolved by inversion of the geodetic data, so depths of 10 km and 15 km were used ("Rupture depth" parameter in Table 1). The 15 km depth also allows, in an approximate way, for the possibility of aseismic afterslip on and under the 1906 rupture patches, which took place in the months and years after 1906 (Kenner and Segall, 2000; Parsons, 2001) and might have helped to further relax nearby faults.

Coseismic stress changes were calculated at the centers of WG99 segments. This approach worked for the 1906 earthquake, because almost all WG99 segments, with the exception of the San Gregorio North (SGN) and the Calaveras South (CS), are far enough removed from the 1906 rupture that there is not a great variation in coseismic stress change from one end of a segment to

the other. Calculations in which the WG99 segments were divided into ~10-km sub-segments offered greater resolution along segments, but the added model complexity did not seem warranted given the many uncertainties in parameter values and in the validity of the elastic-halfspace approach itself. Moreover, the resulting clock-change estimates, reported in WG99 (1999), were not notably different from those obtained using the segment-center approach described here.

The Monte Carlo approach was implemented in two steps. Norm Abrahamson generated 10,000 instances of Bay region fault-segment geometries, slip rates, and R-factors using the values, weights, and constraints assigned by WG99. For each instance, a rupture geometry, a rupture slip distribution, a coefficient of friction, a pore model, and other parameters were selected using the weights shown in Table 1. The coseismic stress change, loading-rate (as described in the next section), and finally a clock change were calculated for each instance using these choices, resulting in a distribution of 10,000 clock changes (Table 2).

Estimating Tectonic Loading Rates

In order to estimate the impact of these coseismically-induced stress changes on Bay region faults, we need to know the long-term loading rate on these faults caused by plate tectonic motion of the Pacific plate relative to the Sierra Nevada plate. There are two traditional ways to arrive at a loading rate in elastic halfspace models, both requiring knowledge of the long-term slip rates of the faults in question.

The first "deep slip" approach assumes that below its seismogenic locked part a fault segment continues to extend downward to great depth. This extension is assumed to be slipping continuously and aseismically at some long-term rate, because the temperatures and rheologies at these depths favor continuous deformation over brittle failure. As the deep section slips it loads additional stress onto the locked patch above and other nearby locked patches. Implementing this approach with dislocations requires that the deep extensions to the faults continue well beyond the study area, because the effect of these deep dislocations is felt at considerable distances. Problems arise at locations where two or more segments join but a discontinuity in long-term slip rates exists at the join, because such discontinuities create large stress and strain anomalies. (In the real world, such discontinuities produce local deformation including folds and ancillary faults.)

The second "virtual dislocation" approach (e.g., Jaumé and Sykes, 1996; Deng and Sykes, 1997; Ward, 2000) can be shown to be equivalent to the deep slip approach in two-dimensional geometries. In the virtual dislocation approach, loading is estimated by forcing the locked patches to slip backwards (that is, in a left-lateral sense for the Bay region) at the observed long-term slip rate. There is no long-term buildup of stress anywhere in the model, as can happen in the “deep slip” approach, because earthquakes occurring on the segments will, in the long-term exactly balance the reverse loading displacement. Virtual dislocation loading is less prone to end effects and join problems because the dislocations are smaller, and was adopted for the present calculations because both these problems exist in the WG99 segmentation model for the Bay region.

For each of the 10,000 instances, the same values for coefficient of friction and pore model parameters were used to calculate loading rates as in the coseismic stress change calculation described in the previous section. It seems likely that different pore models would apply over the long term and short term, corresponding to drained and undrained states (e.g., Rice and Cocco,

2000), but such a modification will probably not change the results greatly given the choice and weights of pore models used here.

Alternate models for loading of Bay region faults based on finite-element computations using more realistic rheologies are discussed briefly in a later section. At least one of these models gives systematically lower loading rates than those calculated here (Parsons, 2001). These alternate loading scenarios are not used here, but should be considered by future working groups.

Seismogenic Scaling Factors (R-Factors)

Some faults in the Bay region are creeping more or less continuously at the surface, and others may have regions of aseismic creep at depth. Because the moment released by such aseismic slip is not available for release in earthquakes, WG99 has assigned to each Bay region fault segment a seismogenic scaling factor or *R-factor* value:

> To account for observed aseismic slip (creep) on some faults in the SFBR, a seismic slip factor, also known as the seismic coupling factor, was introduced in the model. A segment with a seismic slip factor of R=1 accumulates seismic moment at the full geologic rate, while a segment with a factor of R=0 releases all of its geologic moment through creep. The seismic slip factor was used to define the area of the fault that stores seismic moment, thereby affecting both the amount of seismic moment released in a rupture and the mean rate of ruptures on a segment, but not the long-term fault slip rate. (WG99, 1999)

Although this definition seems straightforward enough as applied to the long-term, there are a number of complications that are not immediately obvious. In order to estimate an R-factor for a fault segment, it is usually necessary to recast the definition in terms of what we know from geodesy and geology about the present (interseismic) creep rate and long-term slip rate on a fault segment. If $r \equiv (G-S)/G$ where G is the long-term geologic slip rate and S is the current interseismic slip rate inferred from geodesy, then in general $R \neq r$ because S changes through the seismic cycle. (G may change over time too, but is assumed to be constant in this discussion.) For example, one can imagine creeping faults, driven additionally by slip at depth under adjacent faults during interseismic parts of the cycle so that $S>G$, yielding negative r values (e.g., Savage and Lisowski, 1993; Simpson and others, 2001).

One of the more perplexing problems in applying R-factors to the calculation of clock changes is that the geometry of slipping regions and locked patches makes a considerable difference in estimated loading rates. If the locked patches are concentrated on the deeper parts of a fault segment, loading rates are quite different than if the lock patches are concentrated toward one end of the segment. The creeping parts of a fault segment (for $R<1$) will presumably also respond to a coseismic stress change over time, in general further relaxing locked patches that were relaxed and further loading patches that were loaded, so that the clock change for a given segment will vary with time. Another oddity lies in the fact that even though, for example, half of a fault segment may be free to slip area-wise, the adjacent locked patches occupying the other half of the segment and locked patches on neighboring segments will retard creep on the freely slipping half. When any of these locked patches fail in an earthquake, is it safe to assume that the moment stored in the retarded creep on creeping half will not be released, at least in part, coseismically? Examples offered in Appendix R illustrate some of these behaviors.

Because of these problems and uncertainties as to the real behavior of creeping faults, it was decided once again that the best course was the simplest. For that reason, WG99 R-factors were

applied directly to calculated clock changes by multiplication to yield final clock changes described in the next section (Appendix R, Figure R2). Test runs in which R-factors were applied to loading rates, or in which a range of three different weighted R-factors were applied yielded results that were not different enough to justify the added complexity.

Estimating 1906 Clock Changes and Uncertainties

Assuming a steady loading rate in units of bars/yr and a known coseismic stress relaxation in units of bars, the duration of relaxation in the Coulomb approach is the coseismic step divided by the loading rate. (This assumes that the earthquake-induced stress change and associated shaking have not affected the failure process, the Coulomb failure threshold, the fault strength, the pore fluids, or the loading process in some complicated way.)

For each of the 10,000 instances, a clock change was calculated by carrying out this division. One problem that emerges is that sometimes for a given combination of variables the estimated loading rate is very small (positive or negative), leading to a clock change that is very large (positive or negative). It is unlikely that the simple elastic approach presented here could remain correct over periods of hundreds or thousands of years, so such results are not considered meaningful. Although such values represent less than 10% of the total instances, they do bias the calculation of average values and standard deviations. For that reason, median (rather than average) values are reported in Table 2, and values at the 5- and 95-percentiles are used as 90% confidence bounds.

Comparison with Earlier Results and with Other R-factor Assumptions.

Differences between the clock changes values listed in Table 2 and previous published values (Table 6, WG99, 1999) result from the earlier estimates (1) using 10-km sub-segments, (2) ignoring R-factors values, (3) neglecting height and width uncertainties for WG99 segments, and (4) using maximum and minimum values as uncertainty bounds, rather than the 90% confidence bounds in Table 2. These differences and the R-factors used are shown in Table 3. In general, applying the R-factor directly to the uncorrected clock change produces results comparable to those found by applying the adjustment to loading rate.

Estimating 1989 Clock Changes

For the 1989 Loma Prieta earthquake, calculating coseismic stress changes at the centers of WG99 segments worked adequately for most segments, but failed to yield meaningful results for the Santa Cruz (SAS) and Peninsula (SAP) segments of the San Andreas fault immediately adjacent to the Loma Prieta earthquake rupture. Although segments at intermediate distances (HS, CC, CS, SGS, SGN) showed some variation in coseismic stress changes along their lengths, the stress change values were in general small enough on these segments that the variation could be safely ignored. The two segments adjacent to the rupture (SAS and SAP) experienced extremely large variations in coseismic stress change along their lengths and also in the vertical dimension, so that the values at the WG99 centers were essentially meaningless (Figure LP1). These very large variations in calculated stresses over the surfaces of SAS and SAP depend critically on the distance from the rupture and also on the details of the rupture model used. In order to better sample the range of coseismic stress change values on SAS and SAP, we

constructed a more detailed model of these fault segments with 2-km rectangular patches. The special ad hoc treatment applied to these two segments is described in detail in Appendix LP.

Three published rupture models for the Loma Prieta event were used in the calculation applied to WG99 centers as well as in the special calculation for SAS and SAP. The weights given to these three models are shown in the last row of Table 1. The results of the initial calculation using the centers of WG99 segments are listed in Table 4. The combined results with special values added for SAS and SAP are shown in Table 5. It appears that for most segments, the clock change values are small. Previous estimates of the clock change on the southernmost part of the southern Hayward fault yielded an estimate of ~6 years (Lienkaemper and others, 1997), suggesting that the HS segment might also have profited from special treatment. The preferred value for SAP in Table 5 is close to zero, but the large confidence bounds reflect the variations over the surface of this segment, as is also true of SAS (see Appendix LP for details). Although both these segments have parts that were highly stressed, it is uncertain what the ultimate impact of this stressing might be, since we have no information as to where the hypocenter of the next large event on these segments might lie. It is possible that in the absence of the Loma Prieta event, the next earthquake on one of these segments might have nucleated at one of the spots that were strongly relaxed. It that case, the next event could have been delayed by 1989. The large uncertainty bounds placed on the 1989 clock changes for these segments reflect some of these problems.

Applying 1906 and 1989 Clock Changes as BPT state steps

A summary of preferred clock changes and confidence bounds for the 1906 San Francisco and 1989 Loma Prieta earthquakes is given in Table 6. For 30-year periods beginning after 1906 but before 1989, only the 1906 clock changes should be used as input to Norm Abrahamson's program. For 30-year intervals beginning after 1989, perturbations from both earthquakes should be included. For our original approach using the clock change to shift the reset time of the last event, the timing of the perturbations was not a factor and the two clock changes were added and the reset time of the last event on a segment was shifted by the clock change to a later date if the segment was relaxed and to an earlier date if more stressed. However, as mentioned earlier, this approach was abandoned when it proved to be a poor approximation to the more natural approach in the context of the BPT distribution of stepping BPT state closer or farther from the failure threshhold.

For the "BPT state shift" approach which we ultimately used, the fractional shift in state needs to be calculated separately for each event from its estimated clock change and segment recurrence interval and applied to the BPT state at the appropriate time. Unfortunately, limitations in the program permitted only one state shift per segment in a given run. We worked around this limitation by applying the 1906 state shift to non-San Andreas segments (where 1906 typically had a much larger effect) and the 1989 state shift to two San Andreas segments—the Santa Cruz (SAS) and Peninsula (SAP) segments—where 1989 had a large impact. (San Gregorio South and Mt. Diablo segments had somewhat comparable shifts in both events, but this is not likely to change the overall results greatly.)

A potential inconsistency arises from using the clock change results as input to the Norm Abrahamson program. Ideally, a clock change would be estimated within his program for each instance as it arose using the parameters selected for that instance (although this would add a considerable computational burden to an already complicated program). Otherwise, applying the same tabulated clock changes and confidence bounds to every instance, as was done, could result in a bias caused by potentially strong correlation of the clock changes with certain parameter

values. For example, if the clock changes on a segment were strongly correlated with R-factor values, then it would be inappropriate to select the upper-confidence clock-change value for an instance with a low R-factor. In future efforts, such correlations should also be tabulated, or a cleaner integration of the clock change results into the master program should be considered. One approach would be to tabulate the clock changes by instance and read them into the master program as input, assuming that the relevant instance parameters were specified in advance.

Discussion, Alternate Approaches, and Problems

The confidence bounds given in the various tables reflect the range of possible values that derive from different assumed model parameters. Thus they are measures of uncertainty *relative* to the elastic-halfspace dislocation model used here to calculate these clock changes. The model itself is open to criticism. To name just a few of its shortcomings: (1) It assumes that the earth behaves like an elastic halfspace over periods of decades to centuries, (2) it uses a simple but unlikely mechanism for long-term tectonic loading of the faults, and (3) it averages stress changes over broad segment-surfaces which hides the stress concentrations around individual asperities and locked patches where earthquakes likely nucleate. Ideally, future working group efforts should include estimates from more than one interaction model using different approaches and exploring different physical behaviors and rheologies.

Elastic dislocation models of the stress changes on San Francisco Bay region faults induced by the 1906 event suggest that the relaxation would typically last for decades, depending on the location and distance of the fault from the 1906 rupture (Simpson and Reasenberg, 1994; Jaumé and Sykes, 1996). It seems unlikely that the Earth is going to behave as an elastic medium over a time span of decades, but the current uncertainties in assigning geometries and parameters to more complex models argue in favor of simplicity. Afterslip, aseismic slip on horizontal detachment faults, viscous relaxation in the lower crust, and a host of other possible effects may increase or decrease the clock changes estimated here. In fact the observed seismic quiescence in the Bay region for 70 or more years after 1906 is longer than most estimates based on elastic halfspace models by a factor of 2 or more, suggesting that elastic models based on 1906 coseismic stress changes are not capturing all of the physical processes at play.

Simpson and Reasenberg (1994) attempted to estimate the magnitude of stress changes that would be produced by viscous relaxation on a horizontal detachment at depth after the 1989 Loma Prieta earthquake. Their model suggested that the 1989 coseismic stress changes on some of the Bay region faults might be amplified by a factor of two as the limit of viscous relaxation was reached. Linker and Rice (1997, Fig.5) found that the biggest amplification occurs at the south end of the SAP segment, just north of the rupture, with factors of approximately 4-7 depending on the model used. Kenner and Segall (1999) investigated post-seismic deformation and its effects on stress relaxation after a 1906-size earthquake using 2-dimensional viscoelastic models of the crust and mantle. They concluded that viscoelastic relaxation could over time amplify the effect of the relaxation on the Hayward fault by a factor six for a detachment geometry, increasing the duration of the stress shadow in the vicinity of the Hayward fault by a factor of ~3. Parsons (2001) used a 3-dimensional finite element model to study the loading and interaction of Bay region faults and found stress shadow durations typically 1-2 times longer than those predicted by the elastic model, with Calaveras Central and South segments showing shadows 4-5 times longer.

Although the traditional method used to calculate long-term loading rates in this study has been used in many previous studies, its validity has been questioned. It seems likely that the faults in

the San Francisco Bay region do not extend vertically to great depths, but that the seismogenic layer might be more like an elastic plate lying over a viscous substrate. The faults could be loaded either by displacements in this substrate, which might change in a smooth gradual fashion over the width of the region, or by stresses applied at the edges of the elastic plate. Bourne and others (1998) have suggested that the slip rates on individual faults across a fault zone can give insight as to the distribution of slip at depth, and Savage and others (1999) explored the implications of this idea for the San Francisco Bay region, although Savage (2000) subsequently suggested that in a linear system, it may not be possible to infer information about driving stresses from interseismic surface deformation. Alternatively, if the substrate had a low enough viscosity, the faults might be driven from the sides (J. Dieterich, oral communication, 2000), and each of the subparallel faults might be expected to have about the same long-term loading rate; which fault failed might then depend on stress interactions between the faults, which would tend to relax each other in large events, and relative strengths of the faults. Parsons (2001) has implemented a viscoelastic 3D finite element model driven from the sides and finds loading rates that are typically two-thirds to three-quarters of the values from elastic halfspace models used here.

Another uncertainty is whether the high level of seismicity prior to 1906 represents a normal rate for the region or a decades long pre-cursory increase in rate signaling imminent failure in a great event. This latter possibility is the subject of ongoing research (e.g., Sykes and Jaumé, 1990; Bufe and Varnes, 1993; Bowman and others, 1998). If the seismicity in the 1800's represents the "normal" rate for the Bay region, then the wearing away of the 1906 stress shadow is more ominous than if the high rates of seismicity in the 1800's were building up to the 1906 event.

Appendix R – R-factor Examples

This appendix describes several examples intended to illustrate some of the problems inherent in calculating clock changes for segments with R<1. These examples are very simple and by calculating stress changes and loading rates at the centers of locked patches they offer averaged results that don't reflect the variation in stress changes over the surface of the locked patch. Nonetheless, it is hoped that the results give some idea of the difficulties inherent in using R-factors.

In Figure R1a, a 50-km long by 10-km tall fault segment is assumed to be completely locked (R=1). Deep slip under this segment is simulated by a large vertical dislocation moving in a right-lateral sense at a long-term rate of 9-mm/yr. This configuration approximates the geometry of the Hayward South (HS) segment. A 1906-type earthquake on a parallel fault 30 km to the west induces a 3.525 bar Coulomb stress relaxation, which given the long-term loading rate at the center of the locked segment yields a 37.1 year clock delay in the time to failure of this segment.

Figure R1b shows a geometry in which the fault segment is divided into two side-by-side patches, one (L) that is locked and the second (S) that is free to slip aseismically (Table R1). It is assumed that there is no friction and no pore fluid effects acting on S. The interseismic slip on S increases the loading rate on locked patch L. Note, however, that although the long-term slip rate on the fault is assumed to be 9 mm/yr, the adjacent locked patches retard the interseismic slip on the creeping segment. For example if S is equal in area to L, the interseismic slip rate on S is 6.4 mm/yr.

When the 1906-type earthquake occurs, the loading rate on L (which is higher than the loading rate on the R=1 segment because slip on S also loads L) produces a clock delay of 32.9 years

(Table R1). Given time, however, the creeping segment S may also respond to the relaxation by slowing its rate until stresses on it again reach a steady state. The net effect of this slowdown is to enhance the relaxation on the locked patch, and for the geometry shown, the end result when a steady interseismic state is finally attained is to increase the clock delay to 37.0 years. Depending on the time to re-equilibration and the time to failure, the clock delay could presumably fall somewhere between the lower and higher value.

If all of the retarded slip in creeping segment S is ultimately released aseismically, R=0.5. But, if as seems likely, some of this catch-up slip occurs coseismically when an adjacent locked patch breaks, then R will be larger. If all of the interseismic retardation were recovered coseismically, R=0.67 in this case. Thus an important issue in deciding what R-value applies is knowing how much of the moment stored in creeping but retarded regions of the fault surface gets released coseismically rather than as postseismic afterslip.

Figure R1c shows a geometry in which the fault segment is divided into two stacked patches with the creeping patch S overlying a locked patch L. Results for this geometry are also listed in Table R1. The clock change effects for low R-values are magnified by the geometry, because in this case the center of the locked patch get closer to the deep source of the loading stress as the patch shrinks in height. Once again there is an ambiguity in R-value, depending on how much of the moment stored as retarded slip in the creeping patch gets released coseismically. There is also a time-dependent increase in the magnitude of the clock change caused by postseismic response of the creeping segment to the remote earthquake: As before, the slip rate on the creeping patch is lowered for a time by the earthquake-induced relaxation, which enhances the relaxation on the locked patch and increases the magnitude of the clock delay.

The time constant for such a response on a creeping region of a fault plane is not known. A perfectly frictionless fault would respond immediately, but even creeping faults are not "perfectly" frictionless. One way to estimate this time required for the slipping part of the fault to return to normal is to assume that the slipping part simply stops creeping in response to the relaxation and does not begin again until the equivalent slip deficit that would have been produced if that part were perfectly frictionless is made up. Table R2 lists this estimated recovery time for the various cases. These times range from 37 to 53 years, which is a relative small part of the seismic cycle (but a relatively long time to expect our elastic models to yield realistic results). Part of the southern Hayward fault stopped creeping after the 1989 Loma Prieta earthquake and resumed creep within the expected recovery time of ~ 6 years (Lienkaemper and others, 1997).

In Figure R2, the clock changes from Table R1 are shown in graphical form. The vertical arrows show the time evolution of clock changes as the creeping patch responds to the relaxing stress change. The width of the gray boxes show the range of possible R values for the given geometry depending on how much of the retarded slip gets released coseismically. The dark dashed line through the origin shows the preferred adjustment that has been applied to clock changes based on the R-factor value for a given segment. The two lighter dashed lines together with the dark dashed line are the adjustment (with weights of 0.25/0.5/0.25 respectively from top to bottom) referred to previously. The adjustment using the single dark dashed line was preferred for its simplicity, and because the stacked examples seemed more likely to simulate real fault behavior, with large earthquakes nucleating at greater rather than shallower depth. The results were not very different regardless of adjustment method chosen.

The bottom line is that when it comes to calculating clock changes, the assumed geometry of locked and slipping regions can make a big difference even for identical R-factors. There could

also be a time evolution to the clock change, as patches free to slip respond to coseismic stress changes. Finally, the amount of moment tied up in retarded slip on creeping parts of the fault can represent a substantial fraction of the total stored moment (Table R3), and the amount of this moment that gets released coseismically affects not only the R-factor, but the magnitude of earthquakes on that fault segment, and hence the hazard.

Appendix LP – 1989 Loma Prieta Earthquake and Segments SAS and SAP

Because WG99's Santa Cruz Mountains (SAS) and Peninsula (SAP) segments of the San Andreas fault system lie so close to the Loma Prieta rupture surface, the approach used to estimate clock changes after 1906 could not be used. Regardless of rupture model used, the variations in Coulomb stress change over the surface of these segments was so great that using the center of the segment as the sampling point failed to capture the range of values (Figure 1).

An alternate approach, suggested by Bill Ellsworth, subdivided the SAS and SAP segments into 2-km by 2-km patches under the trace of the San Andreas fault. The median value and the range of values of Coulomb stress change were then calculated for depths between 6-km and 20-km on two subregions of these segments most likely to have been affected by the 1989 earthquake and/or deemed most likely to nucleate future earthquakes. For SAS, this segment consisted of the northernmost 40 km and for SAP the southernmost 20 km.

The three 1989 rupture models used were those of Arnadottir and Segall (1994) based on inversions of geodetic information, Beroza (1995) based on inversion of strong motion data, and Wald and Heaton (1995) based on teleseismic and strong motion records. As can be seen from Figure LP1, there are considerable variations in detail in the calculated shear stress changes produced by these model ruptures on the San Andreas fault surface, although in general, the upper 6 km along the length of the rupture in the adjacent SAS segment tends to be more stressed while the region below 6 km tends to be relaxed. It seems unlikely that the upper 6 km could host a future earthquake of M>6.7, although the region below might well be capable. The remaining ~12 km at the south end of the SAS segment is adjacent to the creeping section of the San Andreas fault lying south of San Juan Bautista, and also seemed less likely to nucleate a M>6.7 earthquake.

For the southern end of the SAP segment, all models indicate increased stress above about 10 km and patches of decreased stress below. If we knew where the next large earthquake on the SAP segment was likely to nucleate, we would have a better idea of the likely impact of 1989 on the SAP segment, but in the absence of such knowledge, the best we can do is assign a large uncertainty to the clock change values—in this case both positive and negative bounds.

As in the 1906 calculation, weighted values of friction and pore parameters shown in Table 1 were used in a Monte Carlo process to estimate the average coseismic Coulomb stress changes shown in Table LP1. The three rupture models were given equal weight, so these values were averaged, as were the 90% confidence bounds, and the resulting average of averages were divided by the median loading rates for these segments to yield estimates of clock changes.

The results shown in Table LP1 with very large confidence bounds of both positive and negative signs are consistent with our lack of knowledge about the processes at work on these segments and about the critical regions for earthquake nucleation.

References Cited

Arnadottir, T., and Segall, P., 1994, The 1989 Loma Prieta earthquake imaged from inversion of geodetic data: Journal of Geophysical Research, v. 99, p. 21,835-21,855.

Bakun, W.H., 1999, Seismic activity of the San Francisco Bay region: Seismological Society of America Bulletin, v. 89, p. 764-784.

Beeler, N.M., Simpson, R.W., Hickman, S.H., and Lockner, D.A., 2000, Pore fluid pressure, apparent friction, and Coulomb failure: Journal of Geophysical Research, v. 105, p. 25,533-25,542.

Beroza, G.C., 1995, Rupture history of the earthquake from high-frequency strong-motion data, in, Spudich, P., ed., The Loma Prieta earthquake of October 17, 1989—Mainshock characteristics: U.S. Geological Survey Professional Paper 1550-A, p. A9-A32.

Bourne, S.J., England, P.C., and Parsons, B., 1998, The motion of crustal blocks driven by flow of the lower lithosphere: Implications for slip rates of faults in the South Island of New Zealand and southern California: Nature, v. 391, p. 655-659.

Bowman, D.D., 1998, An observational test of the critical earthquake concept: Journal of Geophysical Research, v. 103, p. 24,359-24,372.

Bufe, C.G., and Varnes, D.J., 1993, Predictive modeling of the seismic cycle of the greater San Francisco Bay region: Journal of Geophysical Research, v. 98, p. 9871-9883.

Dieterich, J., 1994, A constitutive law for rate of earthquake production and its application to earthquake clustering: Journal of Geophysical Research, v. 99, p. 2601-2618.

Dieterich, J., Cayol, V., and Okubo, P., 2000, The use of earthquake rate changes as a stress meter at Kilauea volcano: Nature, v. 408, p. 457-460.

Deng, J., and Sykes, L.R., 1997, Evolution of the stress field in southern California and triggering of moderate-size earthquakes: A 200-year perspective: Journal of Geophysical Research, v. 102, p. 9859-9886.

Ellsworth, W.L., Lindh, A.G., Prescott, W.H., and Herd, D.G., 1981, The 1906 San Francisco earthquake and the seismic cycle, *in* Simpson, D.W., and Richards, P.G., eds., Earthquake prediction; an international review (Maurice Ewing series 4): Washington, D.C., American Geophysical Union, p. 126-140.

Geist, E.L., and Andrews, D.J., 2000, Slip rates on San Francisco Bay area faults from anelastic deformation of the continental lithosphere: Journal of Geophysical Research, v. 105, p. 25,543-25,552.

Gomberg, J., Beeler, N.M., Blanpied, M.L., and Bodin, P., 1998, Earthquake triggering by transient and static deformations: Journal of Geophysical Research, v. 103, p. 24,411-24,426.

Gomberg, J., Beeler, N., and Blanpied, M., 2000, On rate-state and Coulomb failure models: Journal of Geophysical Research, v. 105, p. 7857-7871.

Harris, R.A., 1998, Introduction to special section: Stress triggers, stress shadows, and implications for seismic hazard: Journal of Geophysical Research, v. 103, p. 24,347-24,358.

Harris, R.A., and Simpson, R.W., 1998, Suppression of large earthquakes by stress shadows: A comparison of Coulomb and rate-and-state failure: Journal of Geophysical Research, v. 103, p. 24,439-24,451.

Jaeger, J.C., and Cook, N.G.W., 1979, Fundamentals of rock mechanics (3rd ed.): London, Chapman and Hall, 593 p.

Jaumé, S.C., and Sykes, L.R., 1992, Changes in state of stress on the southern San Andreas fault resulting from the California earthquake sequence of April to June, 1992: Science, v. 258, p. 1325-1328.

Jaumé, S.C., and Sykes, L.R., 1996, Evolution of moderate seismicity in the San Francisco Bay region, 1850 to 1993: Seismicity changes related to the occurrence of large and great earthquakes: Journal of Geophysical Research, v. 101, p. 765-789.

Kenner, Shelley, and Segall, Paul, 1999, Time dependence of the stress-shadowing effect and its relation to the structure of the lower crust: Geology, v. 27, n. 2, p. 119-122.

Kenner, Shelley, and Segall, Paul, 2000, Postseismic deformation following the 1906 San Francisco earthquake: Journal of Geophysical Research, v. 105, p. 13,195-13,209.

Kilb, D., Gomberg, J., Bodin, P., 2000, Triggering of earthquake aftershocks by dynamic stresses: Nature, v. 408, p. 570-574.

Lienkaemper, J.J., Borchardt, G., and Lisowski, M., 1991, Historic creep rate and potential for seismic slip along the Hayward fault, California: Journal of Geophysical Research, v. 96, p. 18,261-18,283.

Lienkaemper, J.J., Galehouse, J.S., and Simpson, R.W., 1997, Creep response of the Hayward fault to stress changes caused by the Loma Prieta earthquake: Science, v. 276, p. 2014-2016.

Linker, M.F., and Rice, J.R., 1997, Models of postseismic deformation and stress transfer associated with the Loma Prieta earthquake, in Reasenberg, P.A., ed., The Loma Prieta, California, earthquake of October 17, 1989—aftershocks and postseismic effects: U.S. Geological Survey Professional Paper 1550D, p. 253-275.

Okada, Y., 1992, Internal deformation due to shear and tensile faults in a half-space: Seismological Society of America Bulletin, v. 82, no. 2, p. 1018-1040.

Parsons, Tom, Stein, R.S., Simpson, R.W., Reasenberg, P.A., 1999, Stress sensitivity of fault seismicity; a comparison between limited-offset oblique and major strike-slip faults: Journal of Geophysical Research, v. 104, p. 20,183-20,202.

Parsons, Tom, Toda, Shinji, Stein, R.S., Barka, Aykut, Dieterich, J.H., 2000, Heightened odds of large earthquakes near Istanbul; an interaction-based probability calculation: Science, v. 288, p. 661-665.

Parsons, Tom, 2001, Post-1906 stress recovery of the San Andreas fault system calculated from 3-D finite element analysis: (submitted to JGR).

Pollitz, F.F, Burgmann, Roland, and Segall, Paul, 1998, Joint estimation of afterslip rate and postseismic relaxation following the 1989 Loma Prieta earthquake: Journal of Geophysical Research, v. 103, n. B11, p. 26975-26922.

Reasenberg, P.A., and Simpson, R.W., 1992, Response of regional seismicity to the static stress change produced by the Loma Prieta earthquake: Science, v. 255, no. 5052, p. 1687-1690.

Rice, J.R., Cocco, Massimo, 2000, Pore pressure transitions in Coulomb stress analysis of earthquake interactions: Eos, Transactions, American Geophysical Union, v. 81, p. F1086.

Roeloffs, E., 1996, Poroelastic techniques in the study of earthquake related hydrologic phenomena: Adv. Geophys., v. 37, p. 135-195.

Savage, J.C., and Lisowski, M., 1993, Inferred depth of creep on the Hayward fault, Central California: Journal of Geophysical Research, v. 98, p. 787-793.

Savage, J.C., Svarc, J.L., Prescott, W.H., 1999, Geodetic estimates of fault slip rates in the San Francisco Bay area: Journal of Geophysical Research, v. 104, p. 4995-5002.

Savage, J.C., 2000, Viscoelastic-coupling model for the earthquake cycle driven from below: Journal of Geophysical Research, v. 105, p. 25,525-25,532.

Scholz, C.H., 1990, The mechanics of earthquakes and faulting: Cambridge, U.K., Cambridge University Press, 439 p.

Simpson, R.W., and Reasenberg, P.A., 1994, Earthquake induced static stress changes on central California faults, in, Simpson, R.W., ed., The Loma Prieta earthquake of October 17, 1989—tectonic processes and models: U.S. Geological Survey Professional Paper 1550-F, p. 55-89.

Simpson, R.W., Lienkaemper, J.J., and Galehouse, J.S., 2001, Variations in creep rate along the Hayward fault, California, interpreted as changes in depth of creep: Geophysical Research Letters, v. 28, p. 2269-2272.

Stein, R.S., Barka, A.A., and Dieterich, J.H., 1997, Progressive failure on the North Anatolian fault since 1939 by earthquake stress triggering: Geophysical Journal International, v. 128, p. 594-604.

Sykes, L.R., and Jaumé, S., 1990, Seismic activity on neighboring faults as a long-term precursor to large earthquakes in the San Francisco Bay area: Nature, v. 348, p. 595-599.

Thatcher, W., Marshall, G., and Lisowski, M., 1997, Resolution of fault slip along the 470-km-long rupture of the great 1906 San Francisco earthquake and its implications: Journal of Geophysical Research, v. 102, p. 5353-5367.

Toda, Shinji, Stein, R.S., Reasenberg, P.A., and Dieterich, J.H., 1998, Stress transferred by the 1995 Mw=6.9 Kobe, Japan, shock: Effect on aftershocks and future earthquake probabilities: Journal of Geophysical Research, v. 103, p. 24,543-24,565.

Toda, Shinji, and Stein, R.S., 2001, Response of the San Andreas fault to the 1983 Coalinga-Nunez earthquakes: A test of interaction-induce probability changes at Parkfield: Journal of Geophysical Research, (submitted).

Wald, D.J., and Heaton, T.H., 1995, Strong-motion and broadband teleseismic analysis of the earthquake for rupture process and hazards assessment, in, Spudich, P., ed., The Loma Prieta earthquake of October 17, 1989—Mainshock characteristics: U.S. Geological Survey Professional Paper 1550-A, p. A235-A262.

Ward, S.N., 2000, San Francisco Bay area earthquake simulations: A step toward a standard physical earthquake model: Bulletin of the Seismological Society of America, v. 90, p. 370-386.

Zoback, M.D., Zoback, M.L., Mount, V.S., Suppe, John, Eaton, J.P., Healy, J.H., Oppenheimer, D.H., Reasenberg, P.A., Jones, L.M., Raleigh, C.B., Wong, I.G., Scotti, Oona, and Wentworth, C.M., 1987, New evidence on the state of stress of the San Andreas fault system: Science, v. 238, no. 4830, p. 1105-1111.

Figure Captions

Figure 1. Regional stress relaxation shadow produced by the 1906 earthquake. Colors represent decreased (blue) or increased (red) right-lateral shear stress caused by the 1906 event at 6.5 km depth on vertical N35W striking planes. The red line, hachured at 10 km intervals, represents the 1906 rupture model of Thatcher and others (1997) with their preferred offsets in meters printed next to each segment. The black lines, terminated by circles are WG99 fault segments. The red region to the southeast of the 1906 rupture contains the creeping section of the San Andreas fault (not shown).

Figure 2. Coulomb stress evolution diagram for a typical Bay region fault segment showing how a 1906-induced relaxation of the segment would delay its time to failure in a Coulomb failure model. The original failure time $\mathbf{t_A}$ gets delayed until $\mathbf{t_B}$ yielding the clock change shown. The upward slope of the Coulomb stress level curve between earthquakes represents the long-term loading on the fault segment by plate tectonic forces. The gray region indicates the time during which the fault lies in the 1906 stress shadow; the parallelogram rising from the top of the shadow region up to the failure threshold line indicates that the duration of the shadow is identical to the clock change.

Figure R1. Three geometric configurations used in R-factor examples. (a) A locked 50-km long segment, lying between two semi-infinite locked segments, loaded by 9 mm/yr of slip at depth. (b) The segment is subdivided into two side-by-side parts, one slipping freely (S) and the other completely locked (L). (c) The segment is divided into a slipping part (S) lying above a locked part (L). Gray shaded regions are creeping continuously. Results for different relative widths and heights are given in Table R1.

Figure R2. Clock changes estimated from the examples in Table R1 for the geometry where the slipping part of the fault is next (N) to the locked part as in Figure R1b, or over (O) the locked part as in Figure R1c. Subscripts to N and O are the fraction of segment area that is locked.

Black filled squares are clock changes before the slipping segment has had a chance to relax. White filled squares are same after slipping segment has responded fully to the relaxing stress changes. Grey rectangles represent range of clock changes and R-factors depending on how much triggered slip has occurred on the freely slipping part and how much of the retarded slip in slipping areas is released coseismically.

Figure LP1. Horizontal shear stress changes on SAS and SAP segments of the San Andreas fault calculated using three rupture models for the 1989 Loma Prieta earthquake: (a) Arnadottir and Segall (1994), (b) Beroza (1995), (c) Wald and Heaton (1995). The rectangular patches making up these segments are 2-km by 2-km in size and extend from sea level to 20-km depth. Other WG99 fault segments are indicated by red lines and terminated by red dots.

Table 1. – Weights and Choices Entering into Monte Carlo Generation of Instances

Parameter Type	Choices	Weights	Comments	References
Pore fluid effects	Yes / no	0.5 / 0.5	Importance of pore fluid effects is poorly understood.	Beeler and others (2000), Rice and Cocco (2000).
Pore fluid models	"Rice" / "isotropic - poroelastic"	0.5 / 0.5	Applicable model is not known. (B = 1 for both models.)	Beeler and others (2000), Rice and Cocco (2000).
Coefficient of friction	0.0 / 0.4 / 0.8	0.5 / 0.25 / 0.25	Some evidence indicates that the major strike-slip faults act like low-friction faults.	Zoback et al. (1987) Reasenberg and Simpson (1992), Parsons and others (1999).
1906 Rupture depth	10 km / 15 km	0.5 / 0.5	Depth is poorly controlled. Larger depth allows for afterslip also.	Thatcher and others (1997).
1906 Slip distribution	Preferred / min / max	0.6 / 0.2 / 0.2	Takes account of uncertainties in Thatcher et al. slip model.	Thatcher and others (1997).
1989 Rupture models	Arnadottir / Beroza / Wald	0.33 / 0.33 / 0.33	Models produce different results in detail on closer segments.	Arnadottir and Segall (1994), Beroza (1995), Wald and Heaton (1995).

Table 2. 1906 Clock Changes, Coseismic Coulomb Stress Changes, and Long-Term Loading Rates

Seg-ment Num-ber	**Median Clock Change (years)**	Lower 90% Con-fidence Bound (years)	Upper 90% Con-fidence Bound (years)	**Median Co-seismic Stress Change (bars)**	Lower 90% Con-fidence Bound (bars)	Upper 90% Con-fidence Bound (bars)	**Median Loading Rate (bars/yr)**	Lower 90% Con-fidence Bound (bars/yr)	Upper 90% Con-fidence Bound (bars/yr)	Segment Code and Name	
1*	-133.0	-437.5	-13.7	-24.35	-77.27	-2.71	0.171	0.138	0.197	SAS	SAF Santa Cruz
2*	-172.9	-337.4	-61.1	-32.05	-56.71	-11.82	0.187	0.151	0.223	SAP	SAF Peninsula
3*	-212.7	-639.6	75.1	-63.25	-176.16	20.41	0.283	0.226	0.345	SAN	SAF North Coast
4*	-87.9	-223.7	-16.5	-24.33	-60.44	-4.80	0.280	0.223	0.341	SAO	SAF Offshore
5	**-13.5**	-33.0	-0.1	**-3.10**	-7.34	-0.03	**0.138**	0.113	0.164	HS	Hayward South
6	**-25.4**	-44.0	-13.2	**-5.76**	-8.66	-3.27	**0.131**	0.108	0.155	HN	Hayward North
7	**-27.6**	-58.4	-5.2	**-3.36**	-7.13	-0.64	**0.121**	0.098	0.140	RC	Rodgers Creek
8	**-2.3**	-10.5	0.0	**-3.30**	-11.49	-0.91	**0.262**	0.208	0.339	CS	Calaveras South
9	**-4.0**	-14.0	-0.4	**-3.90**	-8.96	-0.39	**0.202**	0.173	0.243	CC	Calaveras Central
10	**-15.1**	-33.4	-2.8	**-2.41**	-4.80	-0.43	**0.124**	0.102	0.148	CN	Calaveras North
11	**-16.3**	-36.8	-4.9	**-2.28**	-3.56	-1.32	**0.066**	0.045	0.083	CON	Concord
12	**-9.7**	-30.1	-2.2	**-1.43**	-3.44	-0.35	**0.069**	0.037	0.086	GVS	Green Valley South
13	**-4.7**	-18.8	0.3	**-0.84**	-2.40	0.06	**0.085**	0.042	0.136	GVN	Green Valley North
14	**-6.2**	-17.8	14.3	**-0.24**	-0.48	0.37	**0.034**	0.013	0.042	SGS	San Gregorio South
15	**-55.1**	-136.6	-6.7	**-6.39**	-16.75	-0.80	**0.106**	0.077	0.129	SGN	San Gregorio North
16	**-19.0**	-38.1	-7.6	**-1.07**	-2.10	-0.39	**0.049**	0.038	0.061	GS	Greenville South
17	**-28.9**	-67.7	-11.5	**-1.27**	-2.02	-0.47	**0.037**	0.021	0.049	GN	Greenville North
18	**-1.6**	-4.4	5.5	**-0.09**	-0.16	0.32	**0.057**	0.023	0.091	MTD	Mount Diablo

Confidence bounds are relative to the models used, rather than absolute (see text).

Negative values for clock changes indicate a delay. Negative values for coseismic Coulomb stress changes indicate a relaxation; that is, the segment moves farther from failure.

Clock changes for starred (*) San Andreas fault segments are not used in the probability calculations, because probabilities for these segments are governed by the date of the last event, which is known at 1906.

Table 3. – 1906 Clock Changes: Comparison with Prior Results

Segment Number	Median 1906 Clock Change (yr) using wts with one R-factor applied to dT	[1] "Simple" 1906 Clock Change (yr) from Open-File Report 99-517	WG99 Seismogenic Scaling Factor (R-factor)	Segment Code and Name	
1	**-133.0**	-	0.8/0.9/1.0	SAS	SAF Santa Cruz
2	**-172.9**	-	0.9/1.0/1.0	SAP	SAF Peninsula
3	**-212.7**	-	0.9/1.0/1.0	SAN	SAF North Coast
4	**-87.9**	-	0.9/1.0/1.0	SAO	SAF Offshore
5	**-13.5**	-20.1	0.4/0.6/0.8	HS	Hayward South
6	**-25.4**	-31.1	0.4/0.6/0.8	HN	Hayward North
7	**-27.6**	-27.9	0.9/1.0/1.0	RC	Rodgers Creek
8	**-2.3**	-13.7	0.0/0.2/0.4	CS	Calaveras South
9	**-4.0**	-13.8	0.3/0.5/0.7	CC	Calaveras Central
10	**-15.1**	-14.6	0.7/0.8/0.9	CN	Calaveras North
11	**-16.3**	-21.2	0.2/0.5/0.8	CON	Concord
12	**-9.7**	-13.1	0.2/0.5/0.8	GVS	Green Valley South
13	**-4.7**	-8.7	0.2/0.5/0.8	GVN	Green Valley North
14	**-6.2**	-5.8	0.8/0.9/1.0	SGS	San Gregorio South
15	**-55.1**	-42.4	0.8/0.9/1.0	SGN	San Gregorio North
16	**-19.0**	-15.8	0.8/0.9/1.0	GS	Greenville South
17	**-28.9**	-23.1	0.8/0.9/1.0	GN	Greenville North
18	**-1.6**	-1.3	1.0/1.0/1.0	MTD	Mount Diablo

[1] The "simple" clock change from WG99 (1999) was the result obtained from the use of preferred parameters and geometries (zero coefficient of friction, no pore fluids, 10-km deep 1906 rupture, Thatcher and others (1997) preferred slip), rather than a weighted combination of parameters and geometries. No adjustment for R-factor was applied.

Table 4. 1989 Clock Changes, Coseismic Coulomb Stress Changes, and Long-Term Loading Rates

Seg-ment Num-ber	**Median Clock Change (years)**	Lower 90% Con-fidence Bound (years)	Upper 90% Con-fidence Bound (years)	**Median Co-seismic Stress Change (bars)**	Lower 90% Con-fidence Bound (bars)	Upper 90% Con-fidence Bound (bars)	**Median Loading Rate (bars/yr)**	Lower 90% Con-fidence Bound (bars/yr)	Upper 90% Con-fidence Bound (bars/yr)	Segment Code and Name	
1*	(-23.5)	(-970.4)	329.7	-4.38	-193.25	59.47	0.170	0.138	0.197	SAS	SAF Santa Cruz
2*	(1.3)	(0.7)	(3.0)	0.25	0.13	0.54	0.187	0.151	0.223	SAP	SAF Peninsula
3	**0.0**	0.0	0.0	**0.01**	0.00	0.01	**0.283**	0.227	0.345	SAN	SAF North Coast
4	**0.0**	0.0	0.0	**0.00**	0.00	0.00	**0.280**	0.223	0.341	SAO	SAF Offshore
5	**-1.0**	-2.3	-0.4	**-0.23**	-0.52	-0.10	**0.138**	0.113	0.164	HS	Hayward South
6	**-0.0**	-0.2	0.0	**-0.01**	-0.05	0.00	**0.131**	0.108	0.155	HN	Hayward North
7	**0.0**	-0.1	0.0	**0.00**	-0.01	0.00	**0.121**	0.098	0.140	RC	Rodgers Creek
8	**-0.3**	-1.2	0.0	**-0.52**	-1.18	-0.04	**0.262**	0.207	0.336	CS	Calaveras South
9	**-0.0**	-0.7	2.2	**-0.01**	-0.51	1.70	**0.202**	0.173	0.243	CC	Calaveras Central
10	**-1.7**	-3.4	-0.9	**-0.26**	-0.51	-0.14	**0.124**	0.102	0.148	CN	Calaveras North
11	**-0.4**	-1.0	-0.1	**-0.05**	-0.10	-0.03	**0.066**	0.046	0.083	CON	Concord
12	**0.0**	-0.2	0.1	**0.01**	-0.03	0.01	**0.069**	0.036	0.086	GVS	Green Valley South
13	**0.0**	-0.1	0.1	**0.01**	-0.02	0.01	**0.085**	0.042	0.137	GVN	Green Valley North
14	**-6.2**	-17.2	1.3	**-0.24**	-0.35	0.04	**0.034**	0.013	0.042	SGS	San Gregorio South
15	**-1.8**	-9.6	0.3	**-0.21**	-1.08	0.04	**0.106**	0.077	0.129	SGN	San Gregorio North
16	**-4.7**	-7.3	1.2	**-0.26**	-0.36	0.06	**0.049**	0.038	0.061	GS	Greenville South
17	**-4.4**	-7.8	-1.6	**-0.18**	-0.27	-0.06	**0.037**	0.021	0.049	GN	Greenville North
18	**-1.2**	-3.2	-0.5	**-0.07**	-0.13	-0.03	**0.057**	0.023	0.090	MTD	Mount Diablo

Confidence bounds are relative to the models used, rather than absolute (see text).

Negative values for clock changes indicate a delay. Negative values for coseismic Coulomb stress changes indicate a relaxation; that is, the segment moves farther from failure.

Clock changes for starred (*) San Andreas fault segments (SAS and SAP) were replaced by values from more detailed models for use in the probability calculations. (See text for details.)

Table 5. – 1989 Clock Changes: Preferred Values and Comparison with Prior Values

Segment Number	**Preferred Median Clock Change (years)**	Lower 90% Confidence Bound (years)	Upper 90% Confidence Bound (years)	**Prior 1989 Clock Change (yr) from Open-File Report 99-517**	Segment Code and Name	
1*	**-66.8**	-229.0	+127.3	-60	SAS	SAF Santa Cruz
2*	**-0.5**	-48.7	+19.2	+5	SAP	SAF Peninsula
3	**0.0**	0.0	0.0	-	SAN	SAF North Coast
4	**0.0**	0.0	0.0	-	SAO	SAF Offshore
5	**-1.0**	-2.3	-0.4	-	HS	Hayward South
6	**-0.0**	-0.2	0.0	-	HN	Hayward North
7	**0.0**	-0.1	0.0	-	RC	Rodgers Creek
8	**-0.3**	-1.2	0.0	-	CS	Calaveras South
9	**-0.0**	-0.7	2.2	-	CC	Calaveras Central
10	**-1.7**	-3.4	-0.9	-	CN	Calaveras North
11	**-0.4**	-1.0	-0.1	-	CON	Concord
12	**0.0**	-0.2	0.1	-	GVS	Green Valley South
13	**0.0**	-0.1	0.1	-	GVN	Green Valley North
14	**-6.2**	-17.2	1.3	-	SGS	San Gregorio South
15	**-1.8**	-9.6	0.3	-	SGN	San Gregorio North
16	**-4.7**	-7.3	1.2	-	GS	Greenville South
17	**-4.4**	-7.8	-1.6	-	GN	Greenville North
18	**-1.2**	-3.2	-0.5	-	MTD	Mount Diablo

The values for starred (*) segments (SAS andSAP) were obtained using more detailed models as described in the text and appendix LP.

Table 6 - Revised Clock Change Values for 1906 and 1989 Earthquakes

	1906			1989				
Seg-ment Num-ber	**Median Clock Change (years)**	Lower 90% Con-fidence Bound (years)	Upper 90% Con-fidence Bound (years)	**Median Clock Change (years)**	Lower 90% Con-fidence Bound (years)	Upper 90% Con-fidence Bound (years)	Segment Code and Name	
1	–	–	–	**-66.8**	-229.0	+127.3	SAS	SAF Santa Cruz
2	–	–	–	**-0.5**	-48.7	+19.2	SAP	SAF Peninsula
3	–	–	–	**0.0**	0.0	0.0	SAN	SAF North Coast
4	–	–	–	**0.0**	0.0	0.0	SAO	SAF Offshore
5	**-13.5**	-33.0	-0.1	**-1.0**	-2.3	-0.4	HS	Hayward South
6	**-25.4**	-44.0	-13.2	**-0.0**	-0.2	0.0	HN	Hayward North
7	**-27.6**	-58.4	-5.2	**0.0**	-0.1	0.0	RC	Rodgers Creek
8	**-2.3**	-10.5	0.0	**-0.3**	-1.2	0.0	CS	Calaveras South
9	**-4.0**	-14.0	-0.4	**-0.0**	-0.7	2.2	CC	Calaveras Central
10	**-15.1**	-33.4	-2.8	**-1.7**	-3.4	-0.9	CN	Calaveras North
11	**-16.3**	-36.8	-4.9	**-0.4**	-1.0	-0.1	CON	Concord
12	**-9.7**	-30.1	-2.2	**0.0**	-0.2	0.1	GVS	Green Valley South
13	**-4.7**	-18.8	0.3	**0.0**	-0.1	0.1	GVN	Green Valley North
14	**-6.2**	-17.8	14.3	**-6.2**	-17.2	1.3	SGS	San Gregorio South
15	**-55.1**	-136.6	-6.7	**-1.8**	-9.6	0.3	SGN	San Gregorio North
16	**-19.0**	-38.1	-7.6	**-4.7**	-7.3	1.2	GS	Greenville South
17	**-28.9**	-67.7	-11.5	**-4.4**	-7.8	-1.6	GN	Greenville North
18	**-1.6**	-4.4	5.5	**-1.2**	-3.2	-0.5	MTD	Mount Diablo

(Negative values for clock changes indicate a delay.)

Table R1 – Summary of R-factor Example Results

Geometry	Fraction of Area Locked L/(L+S)	Long-Term Loading at Center of L with slip on S (bar/yr)	Coseismic Stress Change at Center of L right after event (bar)	Coseismic Stress Change at Center of L with afterslip on S (bar)	Inter-seismic slip rate on S (mm/yr)	Clock Change right after event (years)	Clock Change with afterslip on S (years)	R-factor (assuming all moment accumulated interseismically in retarded slip on S gets released coseismically)	R-factor (assuming all moment accumulated interseismically in retarded slip on S gets released aseismically)
S next to L	1.00	0.095	-3.525	-	-	-37.1	-	1.00	1.00
"	0.75	0.098	"	-3.629	4.2	-36.0	-37.0	0.88	0.75
"	0.50	0.107	"	-3.956	6.4	-32.9	-37.0	0.67	0.50
"	0.25	0.138	"	-5.115	7.4	-25.6	-37.1	0.38	0.25
"	0.10	0.252	"	-9.367	7.8	-14.0	-37.2	0.22	0.10
S over L	1.00	0.095	-3.525	-	-	-37.1	-	1.00	1.00
"	0.75	0.098	-3.346	-3.858	1.7	-30.4	-26.3	0.95	0.75
"	0.50	0.107	-3.139	-5.212	3.5	-15.3	-25.4	0.83	0.50
"	0.25	0.138	-2.910	-9.770	5.5	-6.3	-21.2	0.54	0.25
"	0.10	0.252	-2.764	-23.777	6.9	-2.2	-18.9	0.31	0.10

S is a rectangular area of a fault segment free to slip aseismically; L is a rectangular locked area that fails only in earthquakes. The two rectangles fill a fault segment that is 50 km long and 10 km tall, either side by side with S next to L, or stacked with S over L.

Deep long-term slip rate is assumed to be at 9 mm/yr.

Coseismic event is on a 400 km long, 10 km tall parallel fault surface 30 km away, which slips by 4 m right-laterally in the event.

Table R2 – More R-factor Example Results

Geometry	Fraction of Area Locked L/(L+S)	Inter-seismic slip rate on S (mm/yr)	Fraction of total stored moment in slipping region S	Magnitude equivalent of total stored moment per century	Slip equivalent to relaxation stress applied to S (mm/yr)	Estimated recovery time = slip equivalent/ interseismic slip rate (years)	R-factor (assuming all moment accumulated interseismically in retarded slip on B gets released coseismically)	R-factor (assuming all moment accumulated interseismically in retarded slip on B gets released aseismically)
S next to L	1.00	-	0.0	6.8	-	-	1.00	1.00
"	0.75	4.2	0.15	6.7	156	37	0.88	0.75
"	0.50	6.4	0.22	6.6	237	37	0.67	0.50
"	0.25	7.4	0.35	6.5	275	37	0.38	0.25
"	0.10	7.8	0.55	6.3	288	37	0.22	0.10
S over L	1.00	-	0.0	6.8	-	-	1.00	1.00
"	0.75	1.7	0.21	6.7	090	53	0.95	0.75
"	0.50	3.5	0.38	6.7	172	50	0.83	0.50
"	0.25	5.5	0.54	6.6	241	44	0.54	0.25
"	0.10	6.9	0.68	6.4	275	40	0.31	0.10

S is a rectangular area of a fault segment free to slip aseismically; L is a rectangular locked area that fails only in earthquakes. The two rectangles fill a fault segment that is 50 km long and 10 km tall, either side by side with S next to L, or stacked with S over L.

Deep long-term slip rate is assumed to be at 9 mm/yr.

Coseismic event is on a 400 km long, 10 km tall parallel fault surface 30 km away, which slips by 4 m right-laterally in the event.

Table LP1 – Estimated Clock Changes for SAS and SAP from Three 1989 Rupture Models

	SAS – north 40 km			**SAP – south 20 km**		
	Average coseismic Coulomb stress change (bars)	Lower 90% confidence stress change (bars)	Upper 90% confidence stress change (bars)	Average coseismic Coulomb stress change (bars)	Lower 90% confidence stress change (bars)	Upper 90% confidence stress change (bars)
Arnodottir	-12.6	-70.9	+14.2	-0.6	-20.3	+7.3
Beroza	-11.0	-56.8	+26.7	0.2	-1.2	+1.0
Wald	-9.6	-43.1	+26.1	-0.1	-6.7	+2.9
Average	**-11.1**	**-40.3**	**+22.4**	**-0.1**	**-9.4**	**+3.7**
Median Loading Rate (bars/yr)	0.176 bar/yr			0.193 bar/yr		
Estimated Clock Change (yrs)	**-66.8 yr**	**-229.0 yr**	**+127.3 yr**	**-0.5 yr**	**-48.7 yr**	**+19.2 yr**

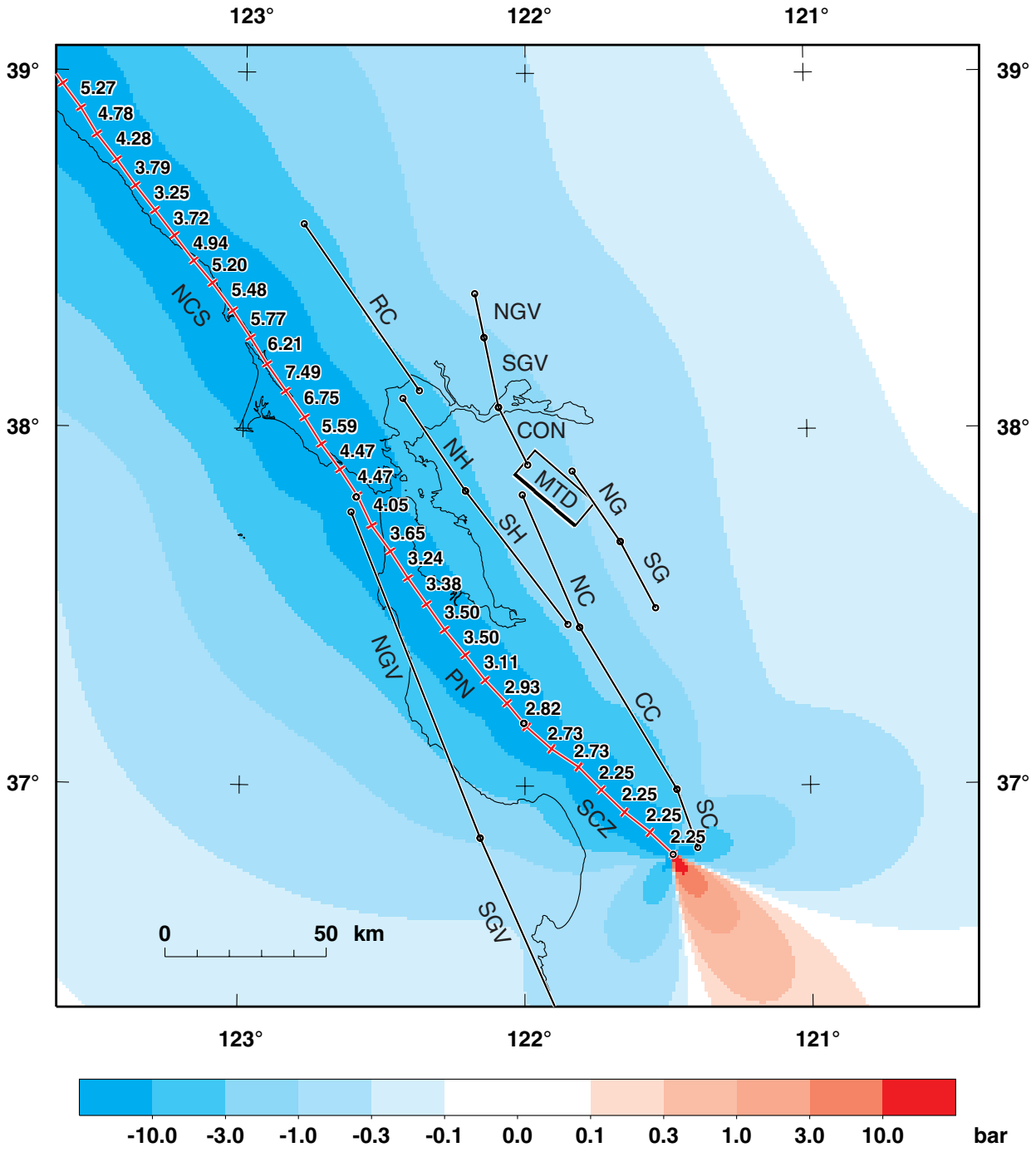
123°
122°
121°
39°
38°
37°
5.27
4.78
4.28
3.79
3.25
3.72
4.94
5.20
5.48
5.77
6.21
7.49
6.75
5.59
4.47
4.47
4.05
3.65
3.24
3.38
3.50
3.50
3.11
2.93
2.82
2.73
2.73
2.25
2.25
2.25
2.25
NCS
RC
NGV
SGV
CON
MTD
NH
SH
NG
SG
NC
CC
SC
SCZ
PN
NGV
SGV
0
50 km
-10.0
-3.0
-1.0
-0.3
-0.1
0.0
0.1
0.3
1.0
3.0
10.0
bar

Figure 1

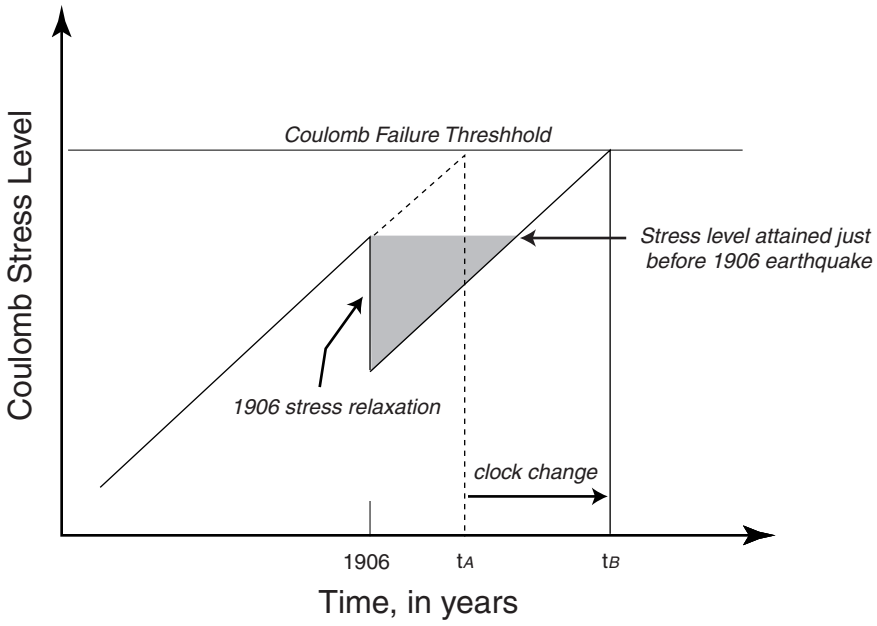
Coulomb Stress Level
Coulomb Failure Threshhold
Stress level attained just
before 1906 earthquake
1906 stress relaxation
clock change
1906
tA
tB
Time, in years

Figure 2

(a)

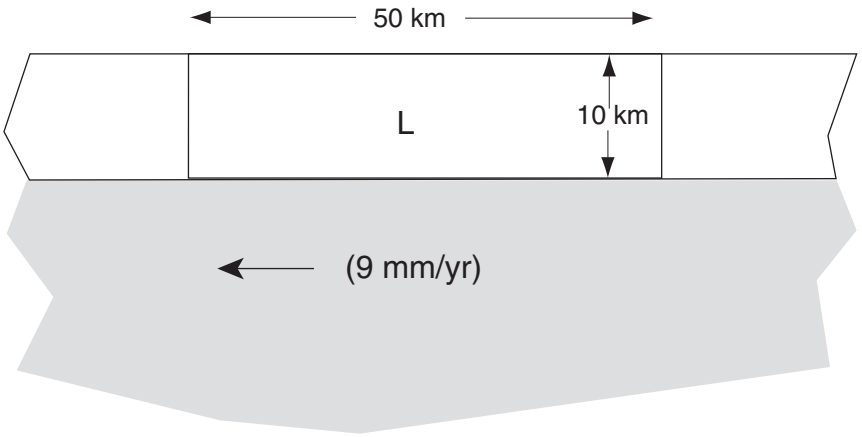

(b)

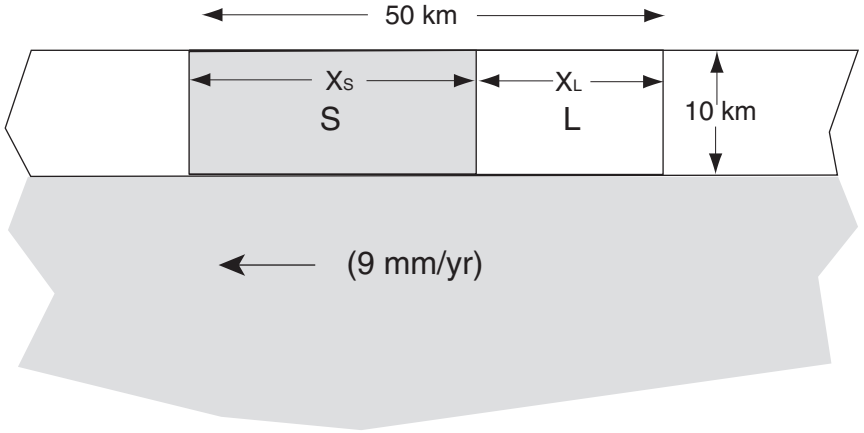

(c)

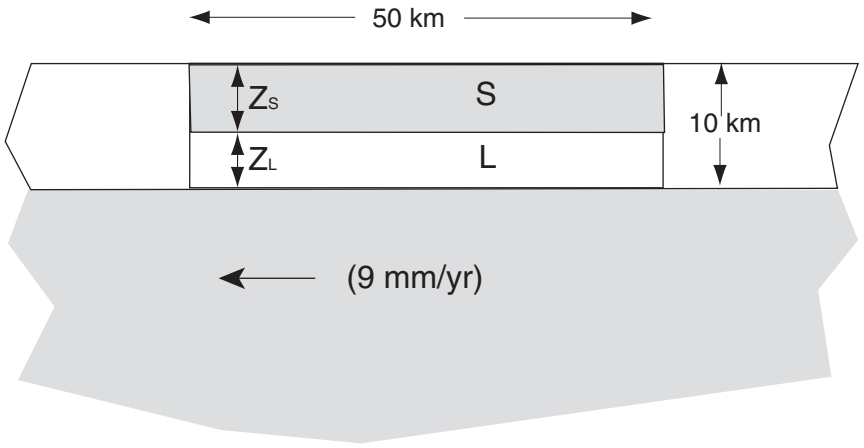

Figure R1

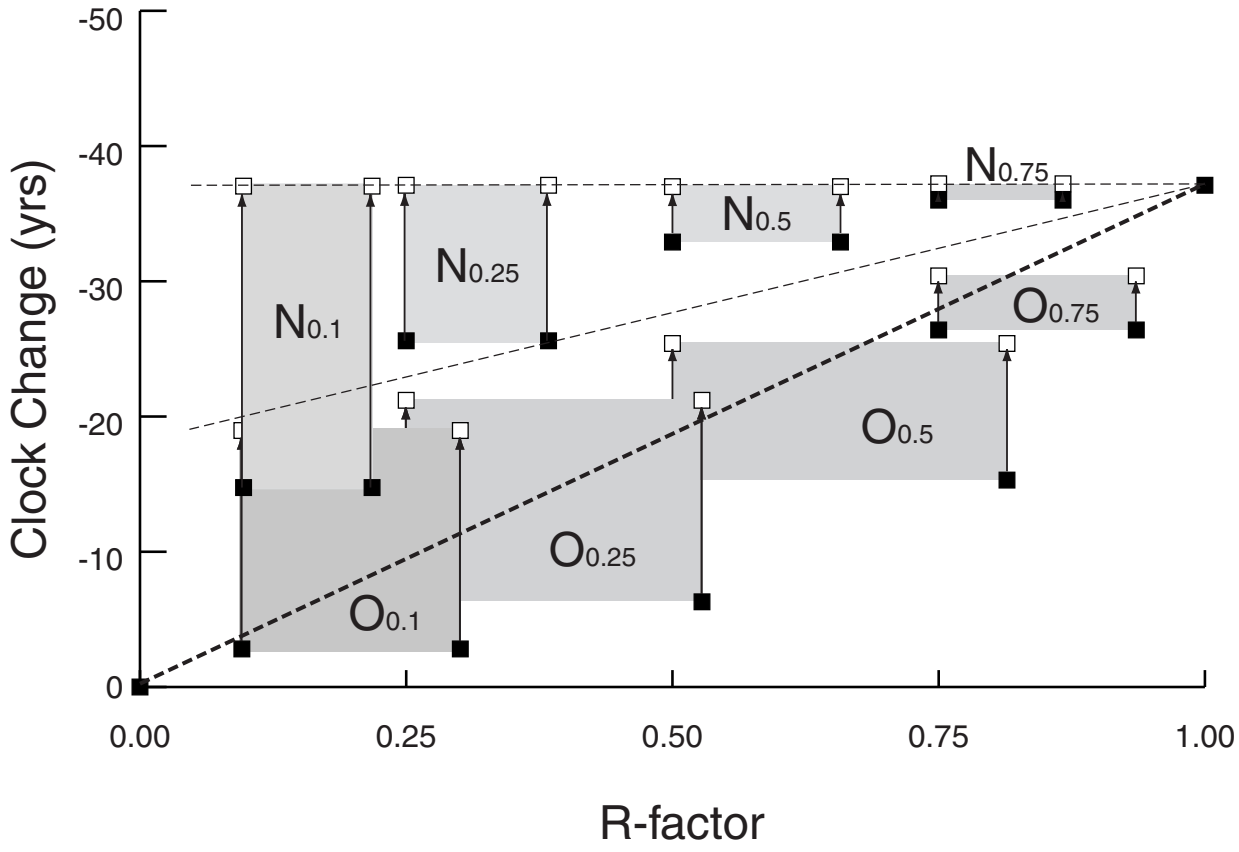
-50
-40
-30
-20
-10
0
Clock Change (yrs)
0.00
0.25
0.50
0.75
1.00
R-factor
N0.1
N0.25
N0.5
N0.75
O0.1
O0.25
O0.5
O0.75

Figure R2

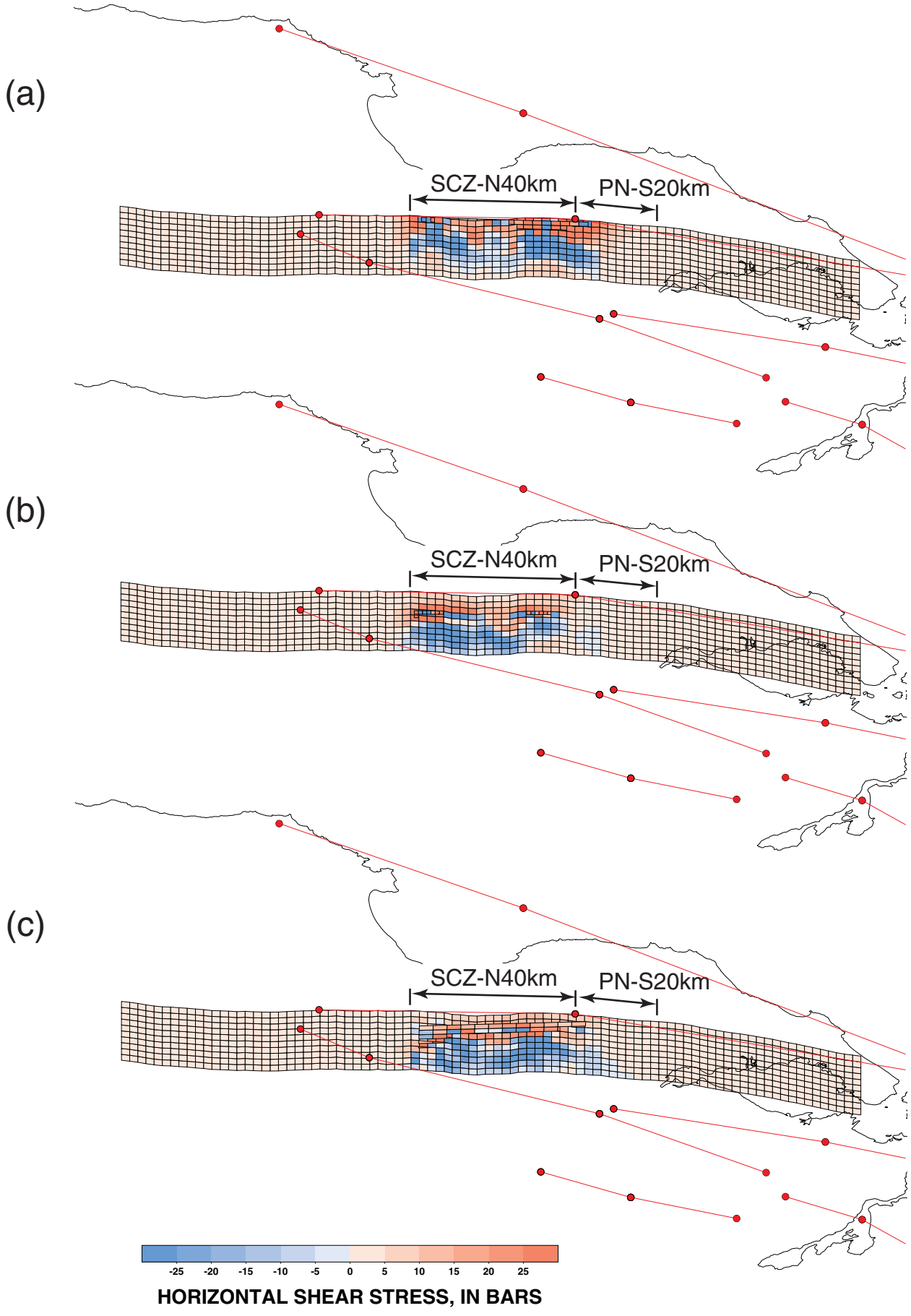
(a)
SCZ-N40km
PN-S20km
(b)
SCZ-N40km
PN-S20km
(c)
SCZ-N40km
PN-S20km
-25
-20
-15
-10
-5
0
5
10
15
20
25
HORIZONTAL SHEAR STRESS, IN BARS

Figure LP1

APPENDIX G: MOMENT-BALANCING THE FAULT RUPTURE MODELS

Norm Abrahamsen, PG&E, and Michael Blanpied, USGS

Introduction

As described in **Chapter 3**, the fault characterization sub-groups assigned preliminary relative likelihood to the various rupture sources by assembling *fault rupture models* for each system. A fault rupture model consists of combinations of *rupture scenarios* that define the complete rupture of the fault system (e.g., **Figure 3.2**). Each scenario is assigned a weight, or relative frequency, which specifies the amount that that mode of failure contributes to the long-term seismic behavior of the fault. One to five fault rupture models were developed for each fault system; where more than one, competing models were weighted collectively by expert opinion (see below). The variation in scenario frequencies between models (e.g., across a row of **Table 3.4**) reflects the degree of certainty that exists in the community about the strength and persistence of segmentation points on each fault. In each realization of the model, a single fault rupture model (a set of relative scenario rates, e.g., a column of **Table 3.4**) is selected for each of the seven fault systems.

In general, the relative scenario frequencies within a given fault rupture model will not result in a moment-rate-balanced model (i.e., will not satisfy $\dot{M}_0$ on each fault segment) because the rupture sources within each rupture scenario have different moments, and those moments vary with the choices of *L*, *W* and *R* made in a given realization of the SFBR model. The problem of moment-rate balancing the model is underdetermined because there are generally more rupture source rates than segment moment rates (or slip rates *v*) to constrain them. Therefore, we use least-squares regression to obtain a set of revised relative rates that are the best fit to the relative rates supplied by the subgroups. This approach in detail in this Appendix, along with an example case worked out in detail, a table of WG02's results, and commentary on the procedure's success.

The need to balance moment

As part of the fault characterization process, groups of experts developed fault rupture models that gave the relative rate of each rupture scenario, r_j. They were asked to consider that if the complete fault system ruptured many (say, 100) times, what would be the percentages of the different rupture scenarios that would be observed. For example, given a two-segment fault, what percentage of the time would the fault generate two-segment ruptures versus pairs of single-segment ruptures.

Since the area of different rupture sources are not all equal in any given rupture scenario, this approach does not necessarily lead to models that are moment-balanced. Again consider the example of the two-segment fault. The seismic moment of the characteristic earthquake scales exponentially with segment area, (e.g. $M_o \propto 10^{1.5A}$) and the moment–rate scales linearly with

segment area ($\dot{M}_o \propto A$). If one segment is longer than the other, the two segments will not have the magnitudes or rates of single segment rupture earthquakes.[1] But in the development of the rupture models, the rates of the two segments are assumed to be the same. Therefore, the rupture models do not lead to moment-balanced models.

Since the rupture models given by the source characterization groups (SCG's) will not produce moment-balanced models, the problem is to find a set of moment-balanced weights for each permissible rupture scenario that lead to relative rates that are as close as possible to those specified in the rupture models by the geologists. A mathematical process for finding the best set of moment-balanced weights is given below.

Moment balancing procedure

We wish to compute the mean rate of occurrence of earthquakes produced by every rupture source. Within a given fault rupture model, multiple rupture scenarios are considered, each with a relative frequency determined by a source characterization sub-group. Using these scenario frequencies, we compute relative rates for each rupture source. These relative rupture rates are not likely to balance the moment rate (long-term slip rate) of each fault segment; therefore, we first adjust the scenario frequencies such that moment rate is balanced.

The problem is to find a set of moment-balanced frequency for each permissible scenario, and additionally to make these as close as possible to those specified by the source characterization subgroups. To do this, we define *relative* rupture rates in terms of the available moment rate and the mean moments of each earthquake that occurs on the fault. In this case the relative rates satisfy the moment rate $\dot{M}_0$ of each fault segment. Then, we minimize the difference between these two sets of relative rupture rates (the one dictated by moment rates and the one provided by the source subgroups), and in so doing, solve for a set of constants that distribute each segment's moment rate onto the various ruptures that involve that segment. It is that distribution of moment rate that allows us to calculate absolute rates for each rupture source. The following paragraphs explain these steps in more detail.

First we compute relative rupture source rates R_G using the scenario weights f supplied by the sub-groups. We make the interpretation that the weights apply to all events in the rupture scenario. That is, if there are two rupture sources in a rupture scenario, then that scenario produces two times as many earthquakes as a scenario with only a single rupture source.

For example, consider a fault with two segments. The two segments can rupture separately (scenario A), or they can rupture together (scenario B). If these scenarios are given equal weight, then there are two single segment ruptures in scenario A for each multi-segment rupture in scenario B. More generally, the relative rate of the i^{th} rupture sources is found as the ratio of sums*:*

[1] Rupture source areas depend on values of length, width and seismic scaling (*R*) factor for the component fault segments. Each of these, and therefore rupture source moments, vary between realizations of the SFBR earthquake model depending on which logic tree branches are selected.

$$R_{G_i} = \frac{\sum_{j=1}^{Nscen} f_j E_{i,j}}{\sum_{j=1}^{Nscen} f_j N_j} \quad (4.9)$$

where f_j is the relative frequency of rupture scenario j, and N_j is the number of earthquakes in fault rupture scenario j. The summation in the numerator is across only those scenarios that include rupture source i (we employ the dummy variable $E(i,j)$ which has value of 1 if rupture source i is included in scenario j, and value 0 otherwise). A floating earthquake counts as one earthquake. The relative rates R_{G_i} for each fault system sum to 1.0, but do not necessarily balance segment moment rates. Values of R_{G_i} are listed in **Table G.4**.

Next, we define an analogous set of relative rates, R_{MB_i}, that *do* balance the moment, and solve for a set of constants C_j that minimize the difference $R_{G_i} - R_{MB_i}$.In a moment-balanced model, the moment is partitioned into each rupture. The relative rate of the individual ruptures sources is given by:

$$R_{MB_i} = \frac{\sum_{j=1}^{Nscen} \frac{\dot{M}_{0i}}{\overline{M}_{0i}} C_j}{\sum_{k=1}^{Nrup} \sum_{j=1}^{Nscen} \frac{\dot{M}_{0k}}{\overline{M}_{0i}} C_j} \quad (4.10)$$

The $\dot{M}_0$'s are the maximum moment rates for rupture sources (product of μ, seismogenic area, and mean slip rate, see (4.8)), the $\overline{M}_0$'s are the mean rupture source moments calculated earlier, and the C's are constants that partition the segment moment rate onto the various rupture sources. (Again, the summations in j are across those scenarios that include the rupture source of interest.) Note that the ratios of moment rates to mean moments define the maximum rate of a rupture source (its rate if it accommodates the full slip rate of all its component fault segments), and the C's temper this rate to recognize that the slip rate may be accommodated by earthquakes on other sources as well.

What remains is only to solve for the values of the partition factors C_j, which we do using least-squares regression, to minimize $R_{G_i} - R_{MB_i}$ across the suite of i rupture sources. The result is a set of partition factors that balance the fault segment slip rates while retaining the character of the fault rupture model to the extent possible.

Example of a two-segment fault

As a simple example, consider a fault with a single segmentation point and the following segment characteristics:

Segment 1:
Length = 100 km

width = 15 km
slip-rate = 10 mm/yr
mu = $3x10^{11}$ dyne/cm^2
moment-rate$_1$ = $4.50x10^{24}$ dyne-cm/yr

Segment 2:
Length = 50 km
width = 15 km
slip-rate = 10 mm/yr
mu = $3x10^{11}$ dyne/cm^2
moment-rate$_2$ = $2.25x10^{24}$ dyne-cm/yr

There are two rupture scenarios (we will not allow a floating rupture source):
Scenario 1: segments 1 and 2 rupture independently
Scenario 2: segments 1 and 2 rupture together

Assume a magnitude-area relation of M=4.0 + log*A* and use a delta function for the magnitude pdf. The resulting magnitudes and moment per earthquake (Mo/eqk) for each rupture source are listed in **Table G.1**.

Table G.1.

Rupture source	M	Mo/eqk	Rate
segment 1	7.18	6.6E+26	0.0068 C_1
segment 2	6.89	2.4E+26	0.0094 C_1
segment 1 + 2	7.35	1.2E+27	0.0056 C_2

Let C_1 and C_2 be factors that partition the moment-rate into scenarios 1 and 2, respectively. (C_1+C_2=1.0)

Then it is straight forward to develop a moment-balanced model for the rate of each rupture source. We just divide the available moment-rate by the Mo/eqk for each rupture source:

$$\text{Rate}(\text{seg}_1) = C_1 * \text{moment-rate}_1/(\text{Mo/eqk})_1$$

$$\text{Rate}(\text{seg}_2) = C_1 * \text{moment-rate}_2/(\text{Mo/eqk})_2$$

$$\text{Rate}(\text{seg}_1) = C_2\ (\text{moment-rate}_1 + \text{moment-rate}_1)/(\text{Mo/eqk})_{1+2}$$

The resulting rates are listed in the last column of **Table G.1**. This is what most people understand by the term moment-balancing.

The problem is that the weights given to the rupture scenarios are based on the relative rates of the different rupture sources, not on partitioning the moment rate. Call the weights from the SCG's w_1 and w_2 for rupture scenarios 1 and 2, respectively.

The relative rate of a rupture source is computed by dividing the weighted number of occurrences of rupture source by the total weighted number of rupture sources. The "weighted number" of rupture source j is computed by adding the P_i values for each rupture scenario that includes rupture source j.

In this example, the weighted numbers for the three rupture sources are listed in **Table G.2** and the total weighted number of ruptures is $2w_1+w_2$. The relative weights from the geologists weights are then computed (Column 3). The relative rate can also be computed from the moment-balanced rates given in Table 1. These are listed in the last column of **Table G.2**.

Table G.2.

Rutpure source	Weighted number	Relative Rate from geologists	Relative Rate (from moment-balance)
segment 1	w_1	$w_1/(2w_1+w_2)$	$\frac{0.0068C_1}{(0.0068C_1 + 0.0094C_1 + 0.0056C_2)}$
segment 2	w_1	$w_1/(2w_1+w_2)$	$\frac{0.0094C_1}{(0.0068C_1 + 0.0094C_1 + 0.0056C_2)}$
segment 1+2	w_2	$w_2/(2w_1+w_2)$	$\frac{0.0056C_2}{(0.0068C_1 + 0.0094C_1 + 0.0056C_2)}$

The moment-balancing done in the WG02 code finds the values of C_i that minimize the difference in the rates computed with the geologists weights and the moment-balanced weights. This is done using least-squares. In this example, we have 3 equations (rates for 3 ruptures sources) and 2 unknowns (C_1 and C_2).

In this example, assume that w_1=0.8 and w_2=0.2. The least-squares solution is

$C_1 = 0.72$

$C_2 = 0.28$

The resulting rates are given in **Table G.3**.

Table G.3.

rupture source	Relative Rate from geologists	Relative Rate (from moment-balance)
segment 1	0.444	0.370
segment 2	0.444	0.511
segment 1+2	0.111	0.119

WG02 results

Resulting values of R_{MB_i} are listed in **Table G.4**. Comparison of R_{MB_i} to R_{G_i} reveals that, for most fault rupture models on most fault systems, only minor adjustments of a few percent or less were required. Larger adjustments were driven by high weight on floating-earthquake scenarios and by large contrasts in moment rate (*L*, *R*, and/or *v*) between fault segments. The Calaveras Fault suffers in both regards, and substantial adjustments were required to obtain fault rupture models that satisfy the moment rates of its three segments. In all four fault rupture models for the Calaveras, the relative rate of rupture of the CN segment was reduced due to its low slip rate (6 mm/yr) relative to CC and CS (15 mm/yr). Nonetheless, the basic character of each fault rupture model (e.g., the relative frequency of single- versus combined-segment ruptures) is preserved.

Comments on the moment-balancing process

The moment-balancing process described below was developed anew by WG99 as a means of handling the problem of determining rates for multiple, overlapping rupture sources. The process turned out to be cumbersome—both to perform and to describe. For example, the meaning of scenario weights was confusing to sub-group members. Also, the process obscures the link between R_{MB_i} and the specific observations, interpretations, and opinions that underlie them. The process for developing moment-balanced models is cumbersome and was confusing to many of the SCG members. As an alternative, we could have solicited a set of moment-balanced models to start with. In fact, we tried that approach but found that some SCG's had difficulty partitioning moment into the different rupture scenarios. Many experts were more comfortable giving the relative rates for each rupture scenario, so we accepted those results and converted those relative rates to moment-balanced models.

We recommend that future working groups consider alternative approaches. One promising alternative is to describe the relative strength (rupture-stopping potential) of segmentation points, rather than relative scenario frequency. This approach was used by the Hayward/Rodgers Creek SCG in developing their estimates of the relative scenario rates. While this approach has the advantage that is seems simpler, it has its own difficulties. First, there is the issue of correlation. For example, if we have a three-segment fault, does the probability that that rupture goes through segmentation point 2 depend on if the rupture went through segmentation point 1? In addition, for the models to be moment-balanced, the strength of the segmentation point (e.g. probability of rupturing through a segmentation point) may need to be different if the rupture starts on one side or the other. In the end, some sort of method for developing moment-balanced models still needs to be applied to the input from the SCG's. This is a topic that would benefit from additional research before the next working group analysis.

Table G.4. Relative rates of SFBR rupture sources, initial and moment-balanced.

	Relative rates from sub-group weights f, R_{Gi}					Relative rates in moment-balanced model, R_{MBi}				
Fault, rupture source	Model 1	Model 2	Model 3	Model 4	Model 5	Model 1	Model 2	Model 3	Model 4	Model 5
San Andreas										
SAS	0.105	–	0.147	0.092	0.081	0.118	–	0.164	0.104	0.089
SAP	0.105	–	0.088	0.092	0.081	0.100	–	0.088	0.089	0.076
SAN	–	–	–	0.012	0.074	–	–	–	0.005	0.067
SAO	–	–	–	0.023	0.094	–	–	–	0.026	0.101
SAS+SAP	0.038	0.310	0.029	0.218	0.074	0.057	0.319	0.050	0.238	0.079
SAN+SAO	0.143	0.310	0.118	0.299	0.081	0.117	0.299	0.102	0.275	0.077
SAS+SAP+SAN	–	–	–	0.012	0.020	–	–	–	0.008	0.010
SAP+SAN+SAO	–	–	0.059	–	–	–	–	0.028	–	–
SAS+SAP+SAN+SAO	0.571	0.310	0.412	0.138	0.329	0.570	0.311	0.416	0.139	0.331
floating	0.038	0.069	0.147	0.115	0.168	0.038	0.072	0.152	0.116	0.170
Hayward/RC										
HS	0.147	0.217	0.313	0.294		0.144	0.213	0.311	0.280	
HN	0.119	0.174	0.229	0.267		0.136	0.196	0.252	0.299	
HS+HN	0.261	0.174	0.042	0.057		0.294	0.215	0.090	0.110	
RC	0.379	0.348	0.271	0.324		0.337	0.296	0.212	0.255	
HN+RC	0.028	0.044	0.083	0.027		0.027	0.042	0.076	0.036	
HS+HN+RC	0.043	0.022	0.029	0.012		0.041	0.020	0.027	0.007	
floating	0.024	0.022	0.033	0.019		0.022	0.020	0.032	0.014	
Calaveras										
CS	0.190	0.095	0.196	0.265		0.209	0.169	0.213	0.273	
CC	0.177	0.095	0.174	0.245		0.189	0.155	0.190	0.242	
CS+CC	0.111	–	0.022	0.020		0.207	–	0.120	0.112	
CN	0.376	0.429	0.370	0.327		0.116	0.108	0.110	0.099	
CC+CN	0.013	–	0.022	0.020		0.012	–	0.014	0.016	
CS+CS+CN	0.022	–	0.022	0.020		0.051	–	0.051	0.051	
Floating	0.022	0.048	0.022	0.041		0.052	0.113	0.053	0.073	
Floating CS+CC	0.089	0.333	0.174	0.061		0.164	0.455	0.249	0.134	
Concord/GV										
CON	0.222	0.083	0.083			0.214	0.081	0.080		
GVS	0.111	0.042	0.042			0.102	0.040	0.039		
CON+GVS	0.111	0.042	0.042			0.087	0.032	0.032		
GVN	0.222	0.083	0.083			0.240	0.090	0.090		
GVS+GVN	0.111	0.042	0.042			0.122	0.045	0.046		
CON+GVS+GVN	0.111	0.667	0.042			0.118	0.669	0.044		
Floating	0.111	0.042	0.667			0.118	0.044	0.669		
San Gregorio										
SGS	–	0.259	0.412			–	0.176	0.284		
SGN	–	0.259	0.412			–	0.319	0.515		
SGS+SGN	0.700	0.259	–			0.700	0.271	–		
Floating	0.300	0.222	0.177			0.300	0.234	0.202		
Greenville										
GS	0.375					0.373				
GN	0.375					0.374				
GS+GN	0.188					0.189				
Floating	0.063					0.064				
Mt Diablo										
MTD	1.000					1.000				

A dash "–" indicates that that rupture source does not exist for that fault rupture model; for example, in fault rupture model 2 for the San Andreas fault, no single-segment ruptures are permitted.